4th European Conference on Chemistry for Life Sciences

4th ECCLS
2011 - Budapest

Foreword

The **4th European Conference on Chemistry for Life Science (ECCLS)** was held 31 August 3 September 2011 in Budapest, Hungary. Previous conferences were held in Rimini (2005), Wroclaw (2007) and Frankfurt (2009). The Budapest Conference inspired an interdisciplinary audience and attracted young researchers to this nascent and highly flourishing field of chemistry and biology.There were closely **400 participants (154 students)** from **37 countries**, of **4 continents** on the event. The organizers invited leading scientists of the field, **4 plenary** (Bertini, Krebs, Lubitz, Seebach) and **11 keynote** (Alberto, Bodor, Csizmadia, Enders, Giralt, Hauser, Hindsgaul, Kozlowski, Leeson, Mansy, Nordén) speakers.

Moreover there were **89 oral presentations** delivered and **171 poster presentations** on view in **15 sessions**:

The Conference covered a wide, interdisciplinary and intersectorial field. With its numerous topics from bioorganic chemistry to bioinorganic chemistry, from chemical biology to structural biology, from glycochemistry to the nucleic acid chemistry, from the chemistry of the „omes" to bionanomaterials, etc. it brings together scientists from different disciplines to find answers to their common questions how chemistry can help to answer their questions concerning details or essence of some life process. These conferences can be very flourishing, as we experienced so far during the past events of this series.

This year a 4 parts Tutorial (towards biology) complemented the Conference for non specialist who wanted to get some medium-level knowledge and skill in molecular biology and molecular biological methods. It was fairly popular as 25 students attended the course, who, at the end received a Certification about the participation.

Undoubtedly, the Conference was a great success and evidenced by the attendance and the quality of presentations. The next meeting is awaited eagerly with great anticipation and will be held at the University of Barcelona in Spain between June 10-12, 2013.

The entire program and abstracts of the conference, list of participants and photographs of the event can be accessed at www.4eccls.mke.org.hu.

Tamás Kiss and András Perczel

Index

Synthesis of Gadolinium-complexed beta-Amyloid binding peptides as Contrast Agents for MRI diagnosis of Alzheimer's Disease

Matharu B., Spencer N., Howe F, Chang E, and Austen B.

Basic Medical Sciences, St George's University of London, London, SW17 ORE

Summary; Early detection and diagnosis of Alzheimer' Disease is crucial for an understanding of the pathogenesis of the disease, and development of treatments. The implication of aggregated forms of small peptides, known as β-amyloid in the disease process, is controversial, but their formation seems to be related to disease progression. MRI of brain is widely used as diagnostic imaging for cerebrovascular disease, but it only detects Alzheimer's at late stages. Here we describe the development of β-amyloid-binding peptide reagents as contrast agents that contain tightly bound gadolinium.

Introduction.

Alzheimer's Disease is the most common neurodegenerative disease. It currently afflicts about 10% of the population over 60, and number s are rising. There is currently no in vivo diagnostic technique apart from memory testing.. Early detection of AD is essential for intervention and successful treatment.

The main pathological feature of AD is the deposition of plaques in the brain, composed primarily of 38-42 residue peptides known collectively as β-amyloid. It would be of immense diagnostic advantage to be able to image β-amyloid deposits in the brains of Alzheimer's patients at various stages of their illness. Considerable success has been achieved with Pittsburg Compound B, a radioactive ligand of aggregated β-amyloid that is visualized by PET scanning (Klunk et al (2004)., Compared with control patients, AD patients showed considerable retention of PIB in areas of association cortex known to contain large amounts of amyloid deposits. The disadvantages of this technique are that individual plaques cannot be seen due to low resolution of PET.. The radionucleotides used have a short half life, and must be synthesized in a location close to the scanner . In contrast, MRI can resolve individual plaques non-invasively, and contrast agents used are not radioactive. These attempts have progressed in different ways. One is the imaging of plaques in AD transgenic

mice after administration of exogenous plaque-labeling contrast media (Poduslo et al., 2002). The second way is microimaging MRI of plaques without exogenous contrast media in the living AD mouse (Jack et al., 2004). The basis for intrinsic MRI contrast (i.e., without administration of an exogenous labeling agent) between individual plaques and normal background tissue is presumed to be related to the iron content of plaques, which accelerates T2 and T2* relaxation rates of tissue water protons in and adjacent to plaques .

Ideally, an MRI amyloid binding reagent would bind aggregated β-amyloid tightly with rapid on-rates, would enhance the image obtained by MRI, by enhancing or inhibiting the T1 or the T2 responses of water molecules in the vicinity of the plaques and amyloid deposits, dissociate slowly over the time taken for an MRI scan (1 hour), and would break down and be cleared rapidly after reappearance in the peripheral circulation.

Materials and Methods. Aβ40 and Aβ42 were synthesized by the optimized Fmoc procedure described previously (El-Agnaf et al 2000). The peptide (1,4,7,10-tetraaza-cyclododecane-1,4,7-tris(acetic acid-t-butyl ester)-10-acetic acid) (DOTA)-GrffvlkGrG-pentadiamine (R1), was synthesized from 4-{4-Formyl-3-methoxyphenoxy}butyric acid (FMBP) NovaGel TM resin (0.55 mequivs)(Nova Biochem),which was suspended in dichloroethane (8ml) and trimethylorthoformate (8ml) and stirred overnight under helium agitation with mono-1-butoxycarbonyl, 1,5-diminopentane (Tosyl salt) (Nova) (1g) along with sodium acetoxy borohydride (0.6g) and DMF (6ml). The resin was washed with excess DMF, followed by 10%(v/v) diisopropylethylamine in DMF, and then 100% dimethylformamide. Fmoc-Glycine (1.2g) and O-(7-Azabenzotriazol-1-yl) 1,1,3,3-tetramethyl uronium hexafluorophosphate (HATU) (1.5g) was added and stirring continued overnight. The following residues were coupled from the C-terminus to the N-terminus, using double coupling with HATU for each position as described by ((Matharu et al., 2010). Fmoc-D-Arg(Pbf), Fmoc-Gly, Fmoc D-Lys(tBoc), Fmoc-D-Leu, Fmoc-D-Val, Fmoc-D-Phe, Fmoc-D-Phe, , Fmoc-D-Arg(Pbf), Fmoc-Gly all from Nova-Biochem, and finally DOTA (1,4,7,10-tetraazacyclododecane-1,4,7-tri(acetic acid-t-butyl ester)-10-acetic acid) were coupled.in 4-molar excess using HATU. Fmoc removal was with 20% piperidine for 10 mins. The modified peptide was released and deprotected with trifluoroacetic acid, triisopropyl silane (5%) and water (5%), triturated with ether , and purified on a column of Phenomenix C4 in 0.1% TFA with an acetonitrile gradient to produce the target compound DOTA-rGffvlkGrG-pentadiamine(mass spec gave 1597 calc 1595). (lower case represents D-amino acids).

The peptides (1,4,7,10-tetraazacyclododecane-1,4,7-tris(acetic acid-t-butyl ester)-10-acetic acid) (DOTA)-Grffvlkrrrrrr-NH2 (R2) and (1,4,7,10-tetraazacyclododecane-1,4,7-tris(acetic acid-t-butyl ester)-10-acetic acid) (DOTA)-Grffvlkrrlsysrrf-NH2 (R3) were synthesized on Fmoc-PAL-PEG-PS resin (1.13g; 0.2mmoles) by the procedure of El-Agnaf et al (2000). Protected DOTA (1,4,7,10-tetraazacyclododecane-1,4,7-tri(acetic acid-t-butyl ester)-10-acetic acid) was coupled in 4-fold molar excess at the final step as above. Additional peptides with εBiotinLys residues inserted at position 8 were also synthesized (BiotinR2 and BiotinR3) to enable monitoring of the reagents.

The Gadolinium salts of R1,R2 and R3 were prepared by incubation overnight with a 3-fold molar excess of gadolinium trichloride in 9ml of water, adjusted to pH 7.0 by the addition of 20mM NaOH, then purified on a preparative column of Phenomenix C4 in 0.1% TFA with an acetonitrile gradient (GdR1;MH gave 1702

Figure 1; Maldi mass spectra of purified imaging agents with and without the addition of Gd
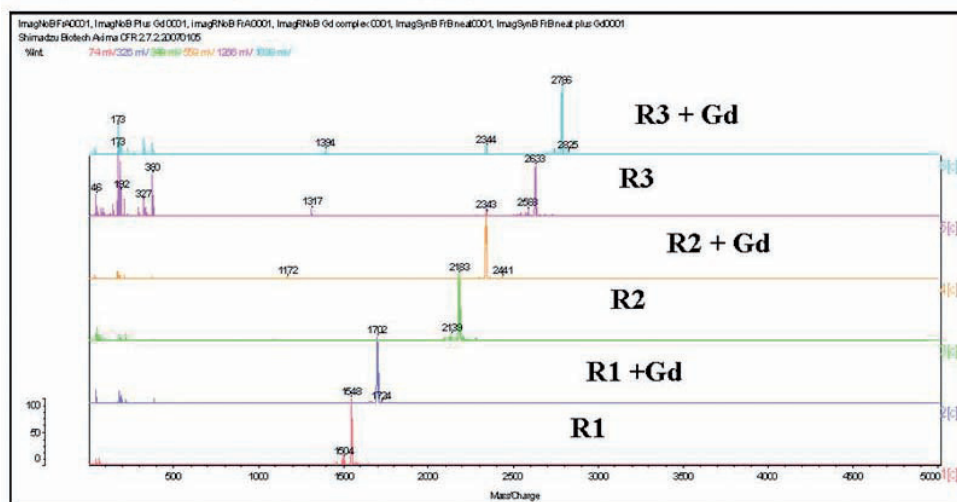
calc 1701) (yield R1 86mg; 0.049mmoles; 9%yield); GdR2; MH=2343 expected 2340);GdR3;MH=2786 expected 2782).The mass spectra of the imaging agents before were as expected from their structures and increased by 157 after the addition of gadolinium are shown in Figure 1.

Results. Solutions of Aβ40 at 1.0mg/ml were prepared in sterile 0.1M Tris (pH7.4), and Aβ42 (1mg) was dissoved in DMSO)) (0.1ml) and then diluted to 1.0 ml with sterile PBS. Solutions were incubated at 37°C for 2 days to produce aggregated forms, which were monitored by Congo red and an ELISA reported previously

β(1-40) Amyloid aggregates were diluted to a final concentration of 50 µg/ml in 10 mM acetate buffer pH 4.5 and coupled to the CM5 chip. activated groups with a 7 minute injection of NHS/EDC at a flowrate of 5 µl/min in the Biacore T100. Reactive ester groups were then blocked by a single 7 minute injection of 1M ethanolamine.HCl.

Affinies were derived from steady-state analysis, each reagent being examined for binding at a range of concentrations (0-100µM)

Imaging reagents 1 and 2 appear to bind more tightly to β(1-42) amyloid proteins than 1-40 proteins, whilst it would appear that this trend is reversed for Imaging reagent 3. Imaging reagent 3 appears to bind to both forms of β-amyloid protein with the highest affinity (Kd~15nM), 3) No specific binding of control reagent 4 to either form of β-amyloid protein was observed and 4) Although binding of Imaging Reagent 1 was observed the binding responses were very low and saturation of the chip has not been observed over the range analysed so a more accurate Kd could not be determined.

Penetration of brain by these reagents into 5xFAD transgenic mice under the influence of nanobubble-activated focused ultrasound, and their suitability in MRI diagnosis, is under investigation.

FC2-1 100uM R1-R4 binding to amyloid 1-40 fibrils
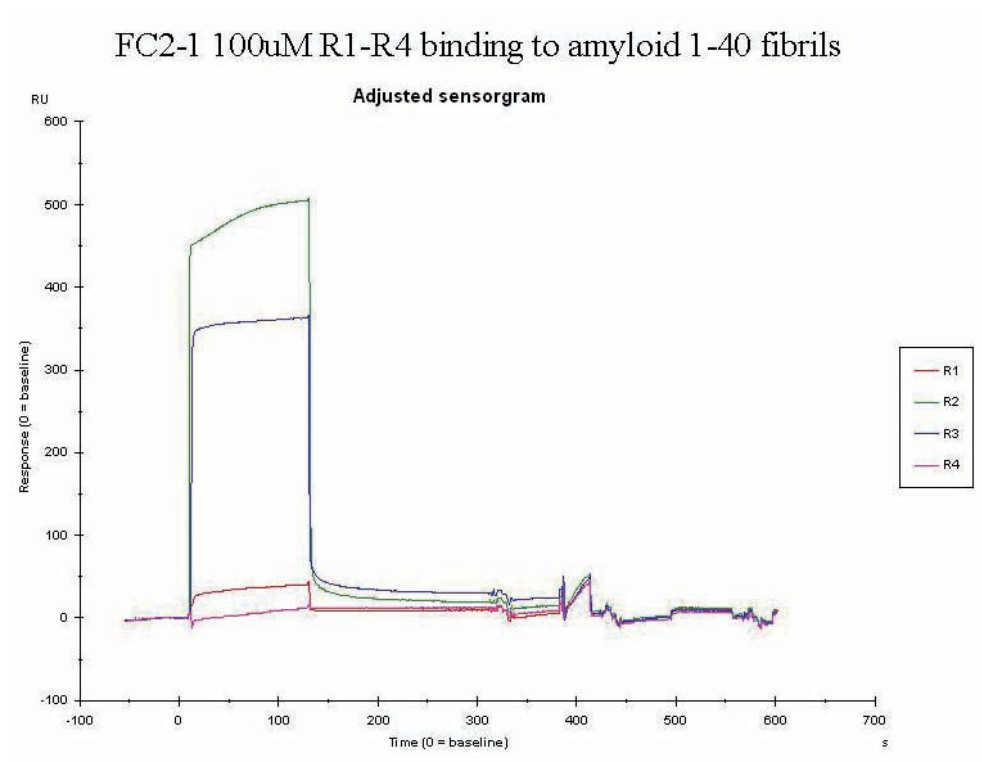
Fig. 2

	ka (1/Ms)	kd (1/s)	KD (nM)
Image R-3 over Amyloid 42	0.8×10^4	0.9×10^{-3}	32.5
Image R-3 over Amyloid 40	1.1×10^4	0.9×10^{-3}	15.2
Image R-2 over Amyloid 40	3.3×10^4	1.6×10^{-3}	49.4
Image R-2 over Amyloid 42	1.9×10^4	1.6×10^{-3}	82.9
Image R-1 over Amyloid 40	7.4×10^5	5.2×10^{-3}	70.8
Image R-1 over Amyloid 42	1.3×10^3	5.4×10^{-4}	399.3

Fig. 3

References

EL-AGNAF OM, MAHIL DS, PATEL BP, AUSTEN BM. (2000a) Oligomerization and toxicity of β-amyloid-42 implicated in Alzheimer's disease. Biochem Biophys Res Commun. ;273(3):1003-1007

EL-AGNAF O, SHERIDAN J, GOODWIN H & AUSTEN BM (2000b) Improved Solid-Phase syntheses of Amyloid Proteins associated with neurodegenerative Diseases. Peptide and Protein Letters 7; 1-8.

JACK CR JR, GARWOOD M, WENGENACK TM, BOROWSKI B, CURRAN GL, LIN J, ADRIANY G, GRÖHN OH, GRIMM R, PODUSLO JF.(2004) In vivo visualization of Alzheimer's amyloid plaques by magnetic resonance imaging in transgenic mice without a contrast agent. Magn Reson Med. 52; 1263-71

KLUNK WE, ENGLER H, NORDBERG A, WANG Y, BLOMQVIST G, HOLT DP, BERG-STRÖM M, SAVITCHEVA I, HUANG GF, ESTRADA S, AUSÉN B, DEBNATH ML, BARLETTA J, PRICE JC, SANDELL J, LOPRESTI BJ, WALL A, KOIVISTO P, ANTONI G, MATHIS CA, LÅNGSTRÖM B. (2004)., Imaging brain amyloid in Alzheimer's Disease with Pittsburg Compound B. Ann Neurol. 55; 306-319

MATHARU B., EL-AGNAF, OMA., RAZVI A., & AUSTEN BM (2010) Development of retroinverso peptides as anti-aggregation drugs for β-amyloid in Alzheimer's Disease. Biochemistry 31; 1866-1872

PODUSLO JF., WENGENECK TM., CURRAN GL., WISNIEWSKI T., SIGURDSSON EM., MACURA SIM., BOROWSKI BJ., AND JACK CR (2002) Molecular targeting of Alzheimer's Amyloid Plaques for Contrast-Enhanced MagneticResonance Imaging Neurobiol of Disease 11; 315-329

Interactions between plant and environment revealed by the concept of state-dependent correlation

Badáczy D. Z.[1], Németh K. E.[2], Kocsis R.[1], Németh Z. I.[1]

[1]*Institute for Chemistry, Faculty of Forestry, University of West Hungary, Sopron, Hungary*
[2]*College of Bioengineering BSc, Pannon University, Veszprém, Hungary*

Summary

Our work presents some correlating results of monitoring investigation of Pendunculate oak (*Quercus robur*), Norway maple (*Acer platanoides*) and maize (*Zea mays*) plants. The monitored pairs of biochemical variables were the activities of peroxidise (POD) and polyphenol oxidase (PPO), reflection intensities of the leaf spectrum and the contents of D-glucose and D-fructose. Various parameters of environmental air (solar radiation, temperature, relative humidity) have been associated to the significant discrepancies of the state-dependent correlations of the variables. Serials of state-dependent regressions have proven to be capable for revealing the latent interactions between the plant and the environment. State-dependent regressions of biochemical variables can or must be regarded as an alternative indicator of the plant adaptation.

Key words*: Quercus robur, Zea mays, Acer platanoides,*glucose, fructose, peroxidase, polyphenol oxidase, reflection spectrum, state-dependent correlation.

Introduction

The photosynthesis is executed with different velocities in the individual leaves. Influenced by environmental factors, the biochemical variables of plant metabolism (metabolite concentrations, enzyme activities) show some distributions in the foliage. In number of cases, the empirical standard deviations of the variables can make the means undistinguishable. Thus, from the standpoint of statistical comparison, the effect of an arbitrary environmental factor on the mean of a biochemical variable can remain hidden. Since the metabolism is a regulated process, the values of biochemical variables can not be independent of each other. Moreover, if the distributions of two variables in the foliage are the same in type then the values of the variables are linearly correlated to each other [1]. The linear relationship of some biochemical variables is sensitive to environmental condition. Alteration of environmental state can induce the significant modifications of regression parameters, namely, those of
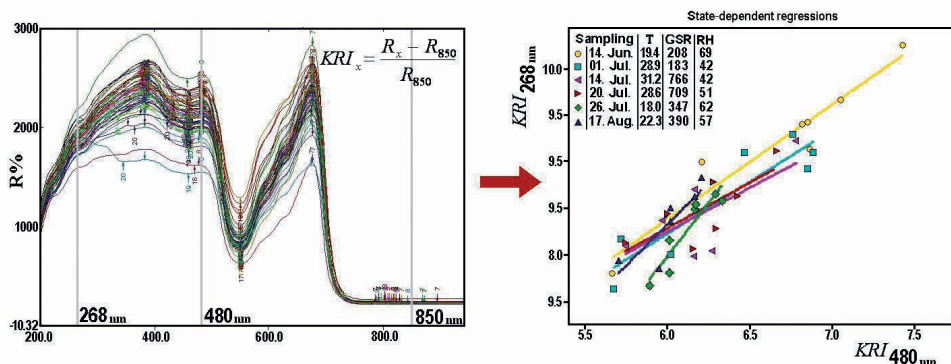
Fig. 1. (a) Reflection spectra of the Norway maple foliage and (b) state-dependent regressions of the reflection intensities (KRI268-KRI480; KRI – compensation reflection index)

the slope, the intercept and the coefficient of determination. This establishment is the main thesis of the concept of state-dependent correlation [1]. Regression straight lines of biochemical variables are state-dependent regressions. Based on the realization of distributional criterion, the theoretical relationship of state-dependent correlation can be derived from standardization formulas of correlating biochemical variables. One of importance of Equation 1 is that physical meaning can be related to linear regression of biochemical variables.

$$(1) \qquad y_2 = \frac{\sigma_2}{\sigma_1} y_1 + \frac{\sigma_1 \mu_2 - \sigma_2 \mu_1}{\sigma_1}$$

where y_1 and y_2 are the correlating biochemical variables, σ_1, σ_2, μ_1 and μ_2 are the theoretical standard deviations and the means. With their determinations in monitoring way, regulated adjustment of physiological state to the actual environmental condition can be tracked. The correlation monitoring of biochemical variables has successfully been applied to the characterization of the vegetation period of Pendunculate oak, Norway maple and maize, moreover, to tracking some abiotic plant stress syndromes [2].

Materials and Methods

Separation of carbohydrates. Sample preparation: 300 mg plant powdered, 800 μl of MeOH : H_2O, 80:20, v/v, centrifugation at 18000 min^{-1}, 10 min, 4 °C; OPLC stationary phase and eluent: HPTLC silica 60 F254 (Merck Co.), ACN : H2O (85:15, v/v); Staining: aniline - diphenyl amine - phosphoric acid, λ=540 nm; *Extraction of enzymes*. 1.2 g plant samples / 15 ml KNa-phosphate buffer (pH = 6.0), 4°C, 20 min at 6000 min^{-1}, 10 min. *Protein determination*: Bradford's method (1976). *Assay (POD)*. Reaction mixture: 1.7 ml buffer (pH=6.0), 30 μl of 0.3 % H2O2, 20 μl *o*-dianizidine, 10-20 μl extract, 480 nm, 1 Unit = 0.01 absorbance unit·min^{-1}. *Assay (PPO)*: 1 ml buffer (pH=6.0), 1 ml (0.2 M) catechol, 0.5 ml extract, 420 nm, 1 Unit = 0.001

Fig. 2. (a) State-dependent regressions of the POD and PPO activities and (b) those of the glucose and fructose levels.

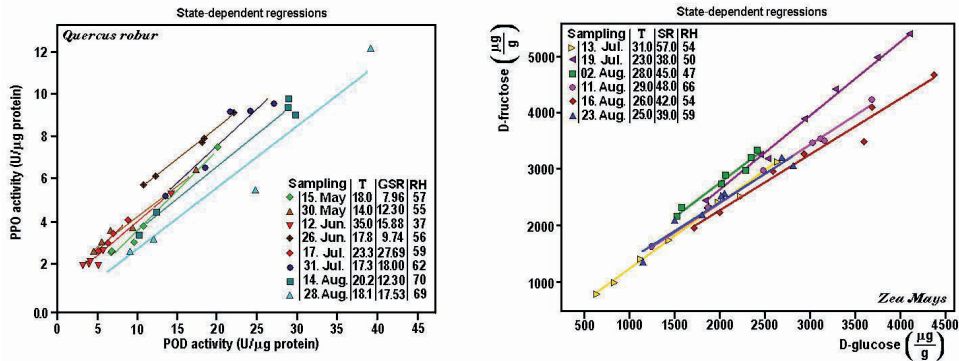|				Spearman's rho coefficient						
			M_{KRI268}	SD_{KRI268}	M_{KRI480}	SD_{KRI480}	slope	intercept	T	RH
Maple (Acer platanoides) KRI_{268}-KRI_{480}	**Pearson's R coefficient**	M_{KRI268}		**0,886**	**0,943**	**0,829**	-0,371	0,371	0,143	-0,029
		SD_{KRI268}	**0,89**		**0,943**	**0,829**	-0,486	0,486	0,371	-0,143
		M_{KRI480}	**0,97**	0,847		**0,714**	-0,429	0,429	0,257	-0,086
		SD_{KRI480}	**0,921**	**0,947**	**0,877**		-0,2	0,2	0,086	0,029
		slope	-0,377	-0,616	-0,385	-0,34		**-1**	**-0,886**	0,657
		intercept	0,384	0,619	0,4	0,345	**-0,999**		**0,886**	-0,657
		T	-0,195	0,181	-0,229	-0,116	**-0,796**	0,784		**-0,886**
		RH	0,387	-0,038	0,456	0,196	0,546	-0,53	-0,927	
			M_G	SD_G	M_F	SD_F	slope	intercept	T	RH
Maize (Zea Mays) Glucose - Fructose	**Pearson's R coefficient**	M_G		0,476	**0,952**	0,024	-0,429	0,452	-0,119	**-0,595**
		SD_G	0,343		0,405	**0,619**	-0,333	**0,762**	0,119	-0,405
		M_F	**0,942**	0,45		0,143	-0,191	0,238	-0,333	-0,476
		SD_F	-0,118	**0,726**	0,117		0,452	0,024	-0,191	-0,048
		slope	-0,537	-0,4	-0,38	0,307		**-0,786**	-0,452	**0,595**
		intercept	0,379	**0,678**	0,312	0,103	**-0,896**		0,357	-0,405
		T (ºC)	0,155	0,409	0,121	-0,085	-0,813	0,864		-0,524
		RH	**-0,598**	-0,499	-0,533	0,001	**0,795**	-0,821	-0,788	
			M_{PPO}	SD_{PPO}	M_{POD}	SD_{POD}	slope	intercept	T	RH
Pendunculate oak (Quercus robur) POD – PPO activities	**Pearson's R coefficient**	M_{PPO}		0.357	**0.881**	0.500	-0.166	-0.142	*-0.547*	**0.547**
		SD_{PPO}	0.313		**0.666**	**0.976**	-0.309	**-0.809**	*-0.119*	**0.619**
		M_{POD}	**0.916**	0.648		**0.761**	-0.214	-0.452	*-0.333*	**0.809**
		SD_{POD}	0.295	**0.987**	0.619		-0.357	-0.761	*-0.238*	**0.666**
		m	-0.284	-0.472	-0.334	-0.577		-0.214	0.428	0.095
		b	0.269	**-0.529**	-0.076	-0.434	-0.383		-0.214	-0.714
		T	*-0.468*	*-0.251*	*-0.459*	*-0.236*	0.150	-0.057		0.071
		RH	**0.562**	**0.609**	**0.737**	**0.587**	-0.060	-0.332	-0.685	

(M_{PPO} , M_{POD}, M_{KRI268}, M_{KRI480}, M_G, M_F: **the means;** *SD_{PPO} , SD_{POD}, SD_{KRI268}, SD_{KRI480}, SD_G, SD_F: empirical standard deviations; T : temperature; radiation; RH : relative humidity)*

Table I. Correlations of biochemical variables and environmental parameters

absorbance unit·min^{-1}. *Reflection spectra:* Shimadzu UV 3101 PC spectrophotometer with ISR 3100 integrating sphere, range: 200-900 nm.

Results and Discussion

In the cases of these three plants, the correlations of various biochemical variables were tracked during the vegetation period. The regressions of biochemical variables, which are influenced by some environmental factors, are depicted in Figures 1 and 2.

Significant deviations of regression parateters within each serials of the regressions can be dected by covariance analysis (ANCOVA). Between some environmental factor and statistical parameters of the variables and as well as state-dependent regressions, relevant correlations can be experienced by correlation analysis. Its results can be found in Table I. The correlation factors in bold highlight the relationships between biochemical variables, furthermore, between environmental factors and the parameters of state-dependent regressions.

Conclusions

The correlations with high values between the means and empirical standard deviations of biochemical variables are the consequences of synchronic regulation of the variable values in the metabolism. The correlations between the slope and the intercept of state-dependent regressions give a support to the existence of equation 1. The correlation analysis can reflect the relevant effects of temperature and relative humidity on the leaf metabolism.

References:

[1] Zs. I. Németh, É. Sárdi, É. Stefanovits-Bányai, *J. Chemometrics*, 23, 197 (2009).
[2] Zs. I. Németh, M. Pozsgai-Harsányi, É. Stefanovits-Bányai, É. Sárdi, *Cereal Research Communications* Suppl S, 37, 141 (2009).

Synthesis of novel polynitrogenated drugs based on phenstatins. Tubulin polymerization evaluation

Álvarez R.[1]*, Caballero E.[1], Pérez-Melero C.[1], De Sio M.[2], Aramburu L.[1], Peláez R.[1], Medarde M.[1]

[1]*Departamento de Química Farmacéutica, Facultad de Farmacia, Campus Miguel de Unamuno, 37007 Salamanca, Spain. [2] Dpto. di Scienze Farmaceutiche e Biomediche, Università di Salerno, Italy. (raquelalvarez@usal.es).*

Summary. – A new family of phenstatin analogues with polynitrogenated aromatic rings has been synthesized and evaluated as tubulin polymerization inhibitors. The synthesized compounds have a 3,4,5-trimethoxyphenyl A ring, a one carbon bridge between the rings and triazolopyridines, benzothiadiazoles, dihydrobenzoxazines or dihydropyridoxazines as B rings. The replacement of carbon atoms by nitrogen aimed at increasing the aqueous solubility results in a lower antitubulin potency.

Introduction.

Cancer is a heterogeneous group of malignancies characterized by uncontrolled cell proliferation and tissue invasiveness. Microtubules and their dynamics are involved in many essential cell functions, such as development and maintenance of shape, motility and intracellular transport, cell signaling and cell division.[1] Microtubules are cylinders formed by protofilaments composed of αβ-tubulin hetero-dimers. The structure of tubulin complex with colchicine and a stathmin-like domain has been elucidated by X-Ray crystallography. Combretastatins are natural products that are able to inhibit tubulin polymerization by binding at the colchicine site, therefore interrupting the cell division cycle and lead to programmed cell death. Combretastatin A-4 has been taken as structural reference to establish structure–activity relationships because of its high potency and its soluble derivatives CA-4 phosphate sodium salt and the amino acid hydrochloride salt AVE8062 are now in clinical development as vascular disrupting agents (Fig. 1).

The SAR of combretastatins revealed that: 1) two non-coplanar aromatic rings is required, 2) the trimethoxyphenyl ring is almost essential for high cytotoxicity and tubulin polymerization inhibitory effects, 3) the guaiacol moiety accepts many modifications at position 2 or 3 and its replacement by bicyclic systems such as naphthalene or indole also maintain the cytotoxicity and TPI effects, and 4) the *cis-*
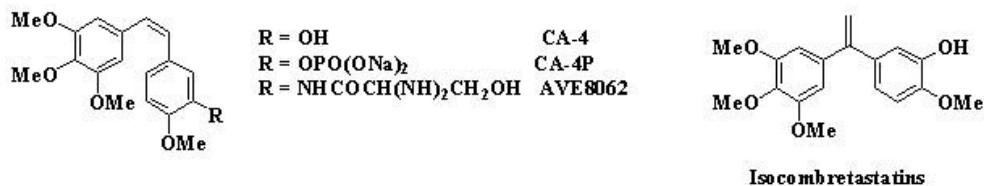
Fig. 1- Structure of combretastatin CA-4 and related compounds.
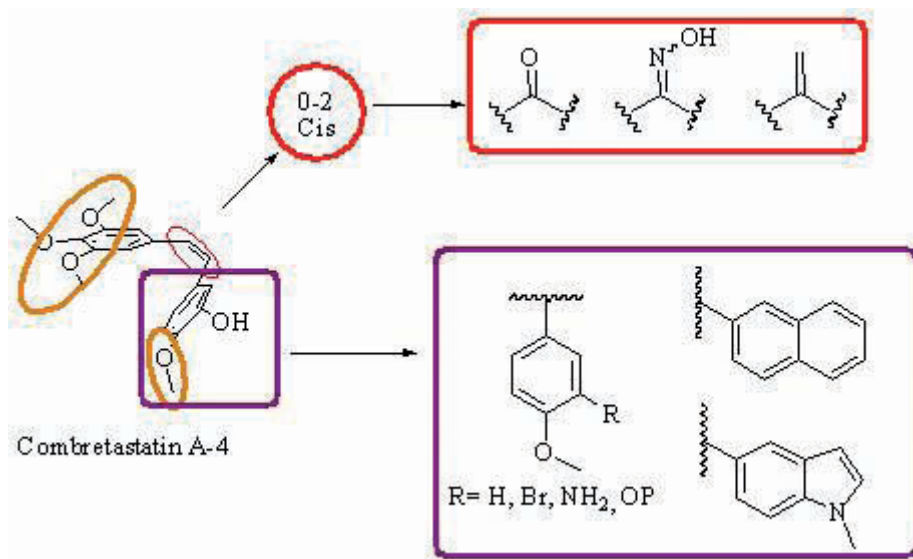
Fig. 2- SAR of combretastatins

oid disposition of the rings is one of the structural keys to preserve their antimitotic activity. In order to avoid the possible *cis-trans* isomerization of combretastatins*,* we decided to synthesize related compounds with only one atom bridge: phenstatins (diarylketones), diaryloximes and isocombretastins (1,1-diarylethenes), which have shown good activity profiles (Fig. 2).

Substitution of the guaiacol moiety by a *N*-methylindole has led to potent compounds that maintain or even improve the efficacy of CA-4[2]. Consequently, we decided to start from these indole analogues (Fig. 3) to design new tubulin ligands employing a scaffold-hopping strategy, that consist of backbone replacements to improve either the activity profile or the physicochemical properties. Usually, carbon atoms replacement by nitrogen atoms is used to this purpose.

In this communication we present the results obtained when the trimethoxyphenyl ring is maintained and the indole moiety is replaced by other heterocycles with one or more nitrogens, in an attempt to increase their water solubility. The selected heterocycles are shown in the figure 4.

Fig. 3- Biological activity of CA-4 in comparison with indole analogues
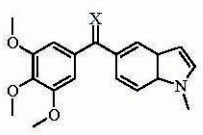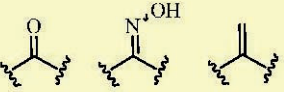
	O (ketone)	N-OH (oxime)	ethene	CA-4
TPI	7.9	1.8	0.7	1-4
HL-60	0.027	0.33	0.003	0.016
A-549	0.19	>10	0.028	0.003
HeLa	0.025	0.36	0.003	0.003
HT-29	0.027	0.11	0.003	0.032
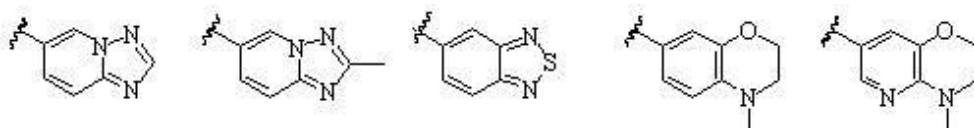
Fig. 4- Structure of proposed analogues
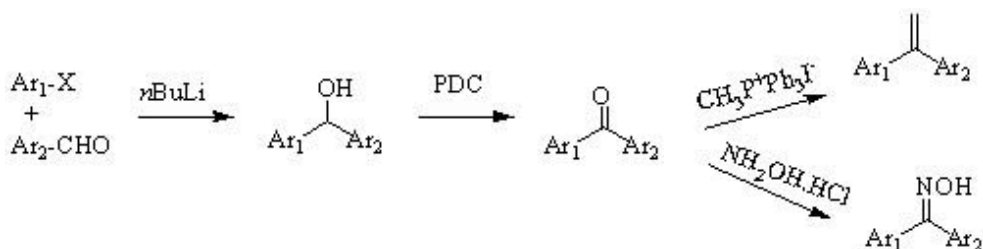
Fig. 5- General synthetic route

Methods and Results.

The compounds were synthesized as outlined in figure 5. The oxime analogues were obtained after treatment of the diarylketones with hydroxylamine hydrochloride, while the 1,1-diarylethenes were produced by Wittig olefination of the corresponding diarylketones, that came from oxidation of diarylmethanols with PDC. The diaryl-methanols were synthesized by reacting the aldehyde of one aromatic moiety with the organolithium or organomagnesium aromatic salts of the other. The organometallic and aromatic ring combination used varied depending on the nature and reactivity of the aromatic systems implied. Thus, for the synthesis of compounds with a triazolopy-
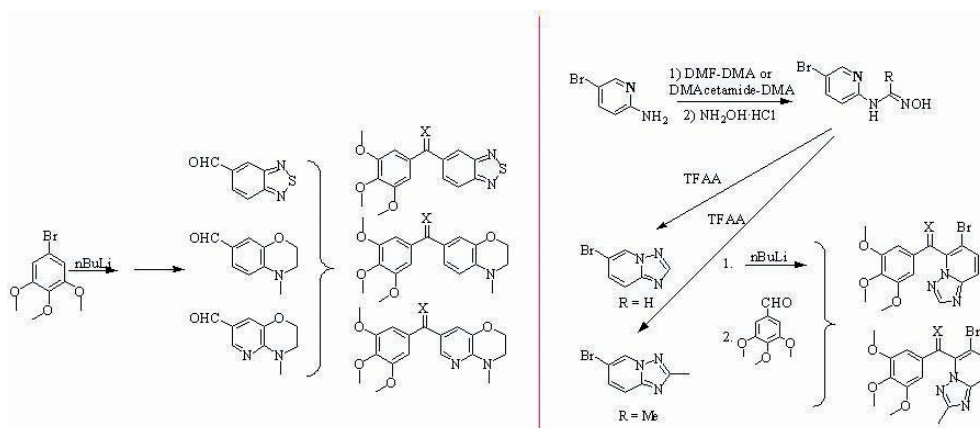
Fig. 6- Structure of the synthesized phenstatins, isocombretastatins and oximes.

ridine moiety we started from its bromo derivate and the trimethoxybenzaldehyde, while for the rest of compounds we employed 5-bromo-1,2,3-trimethoxybenzene and the corresponding aromatic aldehydes, that were comercially available.

The bromotriazolopyridines were obtained by cyclization of the amidoximes syntesized from 2-amino-5-bromopyridine.[3] During BuLi treatment of the triazolopyridines there is a competition between the bromine atom and the acid hydrogen at 5-position, leading to products of condensation at C-5, which maintaine the bromine at C-6 (Fig. 6).

In vitro tubulin assembly studies were carried out with microtubular protein isolated from bovine brains. The samples were preincubated in the cuvettes for 30 min at 20 °C in order to allow binding of the ligand, then cooled on ice for 10 min and placed in the spectrophotometer at 4 °C. The assembly process was initiated by a shift in the temperature to 37 °C and the increase in turbidity followed using a thermostated Thermospectronic Helios α simultaneously in a batch of six cuvettes (containing 1.0 mg/mL MTP in 0.1 M MES buffer, 1 mM EGTA, 1 mM $MgCl_2$, 1 mM, β-ME, 1.5 mM GTP, pH 6.7, and the measured ligand concentration). Each assay contains a negative control (with no ligand) and a positive control (with a ligand that completely inhibits tubulin polymerization).

Unfortunately, none of the synthesized compounds has shown remarkable tubulin polymerization inhibition, being their IC_{50} above 20 μM.

Conclusions.

Scaffold hopping methodology has allowed us to design a new family of polynitrogenated phenstatins with improved water solubility that has been obtained by a useful synthetic methodology to introduce different rings. The design and synthesis of new compounds is still required in order to improve their antimitotic activity.

References

1. J. HYAMS, C. W. LLOYD, *Microtubules*, New York, Wiley-Liss, 1994.
2. C. ALVAREZ, R. ALVAREZ, P. CORCHETE, C. PEREZ-MELERO, R. PELAEZ, M. MEDARDE, Exploring the effect of 2,3,4-trimethoxy-phenyl moiety as a component of indolephenstatins
3. *Eur. J. Med. Chem*. 45, 588-597, 2010.
4. E. HUNTSMAN, J. BALSELLS, New method for the general synthesis of [1,2,4]triazolo[1,5-a]pyridines. *Eur. J. Org. Chem*. **2005**, 3761-3765.

Design of Non-secosteroidal VDR Ligands and Binding Mode to VDR-LBD

Demizu Y.[a],*, Sato Y.[a], Horie K.[b], Takagi K.[b], Kakuda S.[b], Takimoto-Kamimura M.[b], Okuda H.[a], Kurihara M.[a]

[a]Division of Organic Chemistry, *National Institute of Health Sciences*, Tokyo 158-8501, Japan
[b]*Teijin Institute for Biomedical Research, Tokyo 191-8512, Japan*

Summary

We synthesized, evaluated, and analyzed the X-ray structure of stereoisomers of nonsecosteroidal VDR ligands LG190178, and revealed that (*S,R*)-isomer, YR301 had potent activity comparable to natural ligand Vitamin D_3. Furthermore, we designed new ligands based on YR301 structure, and YR335 showed potent transcriptional activity, which was comparable to that of YR301.

Introduction

Vitamin D receptor (VDR) ligands are therapeutic agents used for the treatment of psoriasis, osteoporosis, and secondary hyperparathyroidism. VDR ligands also show immense potential as therapeutic agents for autoimmune diseases and cancers of the skin, prostate, colon, and breast as well as leukemia. In 2000, Moras et al. revealed the binding mode between $1\alpha,25$-dihydroxyvitamin D_3 [$1\alpha,25(OH)_2D_3$] and the ligand binding domain (LBD) of VDR by X-ray analysis (Figure 1).[1] This enabled the novel design of VDR ligands using structure-based drug design. Non-secosteroidal ligands for VDR have thus become an attractive target for the development of new therapeutics. LG190178 is the first novel non-secosteroidal ligand to be developed and shows potential as a therapy for cancer, leukemia, and psoriasis with fewer calcium mobilization side effects than are associated with secosteroidal $1\alpha,25(OH)_2D_3$ analogues;[2] however, although LG190178 has four stereoisomers, there is no apparent active isomer of LG190178 (Figure 1). Here, we synthesized four isomers of LG190178, evaluated their transcriptional activities on HOS-cells,[3,4] and solved the crystal structure of the rat VDR LBD bound with YR301.[5] Furthermore, we designed the new non-secosteroidal ligands based on docking model of YR301 bounded to the VDR, and evaluated the osteocalcin transcriptional activity on HOS-cells.
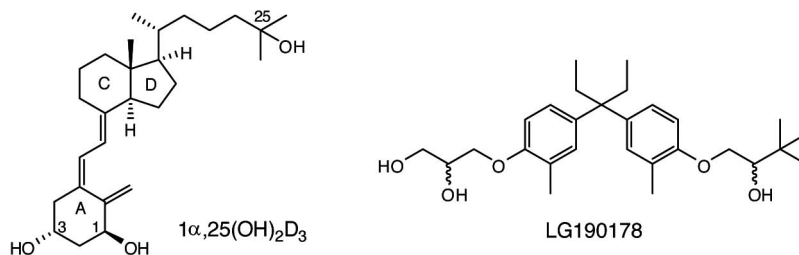
Figure 1. Chemical structures of 1α,25(OH)2D3 and LG190178.
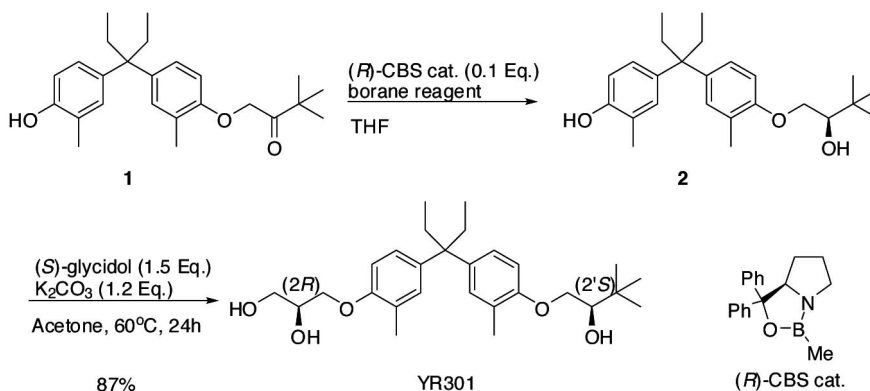
Scheme 1. Facile synthesis of the (2S,2'R)-isomer (YR301) of LG190178.

Ligands	Transcription EC_{50} (nM)[1]	VDR affinity
1α,25(OH)$_2$D$_3$	0.01	100
YR301 (2S,2'R)	0.04	28.3
YR302 (2S,2'S)	1.66	0.831
YR303 (2R,2'R)	4.68	0.482
YR304 (2R,2'S)	15.6	0.112

[1] Human Osteosarcoma cell, serum free.

Table 1. Transcriptional activity and VDR affinity of nonsecosteroidal VDR ligands YR301-304.

Results

The (2*S*,2'*R*)-isomer of LG190178 was synthesized starting from bisphenol derivative **1** (Scheme 1). The asymmetric center at the 2'-position was constructed by (*R*)-CBS-oxazaborolidine-catalyzed (CBS, Corey-Baski-Shibata) asymmetric borane reduction to give (*R*)-**2** with a high yield and excellent enantioselectivity. After treatment of (*R*)-**2** with (*S*)-glycidol, the desired (2*S*,2'*R*)-isomer YR301 was obtained in
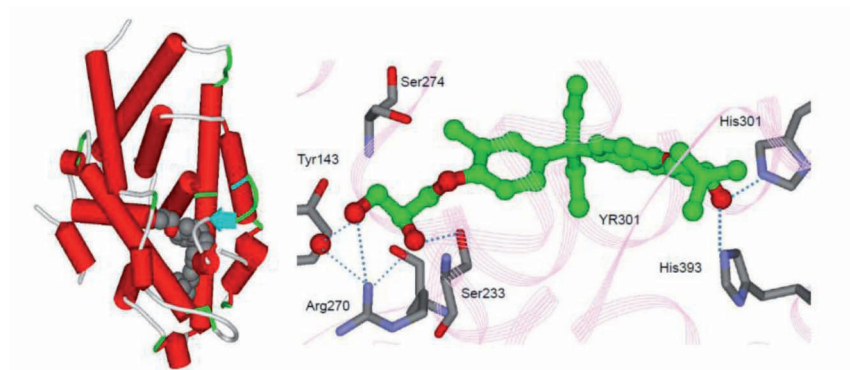
Figure 2. H-bond networks detected in the X-ray structure of the complex between the VDR LBD and YR301.
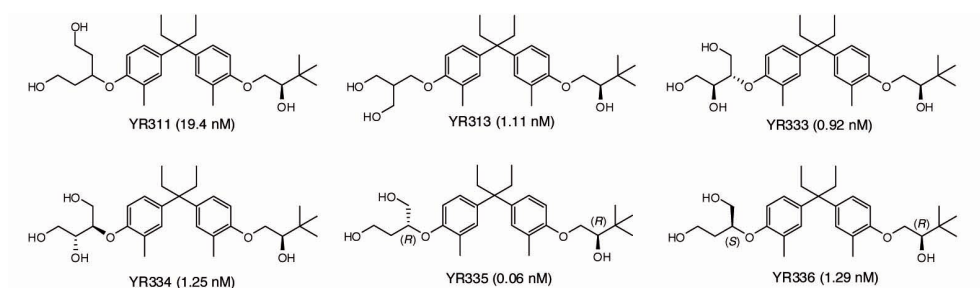
Figure 3. Chemical structures and transcriptional activities of new nonsecosteroidal VDR ligands.

a sufficient yield. In a similar manner, the (2S,2'S)-isomer YR302, (2R,2'R)-isomer YR303, and (2R,2'S)-isomer YR304 were also synthesized.[4]

Next, we evaluated the transcriptional activity using osteosarcoma cells (HOS-cells) and VDR affinity of synthetic ligands (Table 1). YR301 exhibited potent transcriptional activity, comparable to natural ligand Vitamin D$_3$.[3] YR302 and YR303 decreased activity by two orders of magnitude compared with YR301. YR304, the enantiomer of YR301 exhibited the weakest activity. YR301 also shows the highest VDR affinity compared with other ligands.

To understand the strong activity of YR301, the crystal structure was solved with YR301 and the rat VDR.[5] YR301 embeds in the ligand-binding pocket in the same position as Vitamin D$_3$ and four hydrogen bonds are observed. YR301 formed H-bonds with Ser233, Arg270, His301, and His393, but not with Tyr143 or Ser274. YR301 formed an H-bond network containing just four residues.

We therefore attempted to design non-secosteroidal ligands with the ability to bind with all six residues of the VDR. We synthesized new non-secosteroidal ligands and examined using a transactivation assay involving the human osteocalcin promoter (Figure 3). YR335 exhibited potent transcriptional activity (0.06 nM), which was comparable to those of 1α,25-dihydroxyvitamin D$_3$ (0.01 nM) and YR301 (0.04 nM).

Most of the ligands except YR311 showed moderate activity. YR336 displayed activity that was two orders of magnitude lower than that of YR335.

Conclusions

We synthesized, evaluated, and analyzed the X-ray structure of stereoisomers of nonsecosteroidal VDR ligands LG190178, and revealed that (*S,R*)-isomer, YR301 had potent activity comparable to natural ligand Vitamin D_3. Furthermore, we developed new ligands based on YR301 structure, and YR335 showed potent transcriptional activity, which was comparable to that of YR301.

References

1. ROCHEL, N.; WURTZ, J. M.; MITSCHLER, A.; KLAHOLZ, B.; MORAS, D. The Crystal structure of the nuclear receptor for vitamin D bound to its natural ligand, *Mol. Cell. 5*, 173-179 (2000).

2. BOEHM, M. F.; FITZGERALD, P.; ZOU, A.; ELGORT, M. G.; BISCHOFF, E. D.; MERE, L.; MAIS, D. E.; BISSONNETTE, R. P.; HEYMAN, R. A,; NADZAN, A. M.; REICHMAN, M.; ALLEGRETTO, E. A. Novel nonsecosteroidal vitamin D mimics exert VDR-modulating activities with less calcium mobilization than 1,25-dihydroxyvitamin D_3, *Chem. Biol. 6*, 265-275 (1999).

3. HAKAMATA, W.; SATO, Y.; OKUDA, H.; HONZAWA, S.; SAITO, N.; KISHIMOTO, S.; YMASHITA, A.; SUGIURA, T.; KITTAKA, A.; KURIHARA, M. (2*S*,2□*R*)-Analogue of LG190178 is a major active isomer, *Bioorg. Med. Chem. Lett. 18*, 120-123 (2008).

4. DEMIZU, Y.; NAKATSU, A.; SATO, Y.; HONZAWA, S.; YAMASHITA, A.; SUGIURA, T.; KITTAKA, A.; KATO, S.; OKUDA, H.; KURIHARA, M. Facile synthesis of stereoisomers of the non-secosteroidal ligand LG190178 and their evaluation using the mutant vitamin D receptor, *Lett. Org. Chem. 8*, 43-47 (2011).

5. KAKUDA, S.; OKADA, K.; EGUCHI, H.; TAKENOUCHI, K.; HAKAMATA, W.; KURIHARA, M.; TAKIMOTO-KAMIMURA, M. Structure of the ligand-binding domain of rat VDR in complex with the nonsecosteroidal vitamin D_3 analogue YR301, *Acta Cryst. F64*, 970-973 (2008).

Sol-Gel Synthesys Applied for Immobilization of Trichoderma viride Cellulase

Dragomirescu M.[1], Preda G.[2]

[1]*Banat University of Agricultural Science and Veterinary Medicine, Faculty of Animal Sciences and Biotechnologies, Timisoara, Romania,*
[2]*West University of Timisoara, Faculty of Chemistry Biology Geography, Timisoara, Romania*

Summary

In our work CM-cellulose was hydrolyzed using *Trichoderma viride* cellulase, free or entrapped in silica and alginate gels. As alkoxysilane precursors, TMOS and TEOS were used in a two step sol-gel synthesis. Ethanol and ethylene glycol were used comparatively as alcohols in the sol synthesis. The enzyme-substrate affinity modification was investigated based on the functional parameters of native and immobilised enzymes. Enzymes stability was analyzed after reuse in six operational cycles.

Introduction

Cellulosolytic enzymes act collectively to convert cellulose to glucose molecules. They are used in several biotechnological applications including bioremediation and industrial applications such as food and feed, paper and textile industry. In the last years cellulases are intensively studied because they are key enzymes in producing biofuels and chemicals from agricultural products and lignocellulosic biomass [1, 2]. The performance of cellulase mixtures in biomass conversion processes depends on several of its properties including stability. The physical, chemical and biological environmental parameters can do changes in the spatial configuration and the activity of an enzyme molecule. There are different ways to stabilize such an enzyme molecule. Stabilized enzymes by immobilization have significant applications in extensive areas. Silica based mesoporous materials obtained by sol-gel method have been found to be valuable host matrixes for immobilized enzymes due to their biocompatibility, mild obtaining conditions and tailored pore size [3].

Materials and Methods. CM-cellulose sodium salt (CMC, low viscosity), (+)-glucose, hexane, Folin-Ciocalteus phenol reagent, bovine serum albumin (BSA) and tetraethoxysilane (TEOS) were purchased from Merck. Alginic acid sodium salt and tetramethoxysilane (TMOS) were obtained from Fluka. Potassium sodium tartrate was from Sigma-Aldrich. Ethylene glycol (EG) was from Scharlau. All the other

Gel precursor	CMCase activity mmol·min^{-1}·g^{-1}	Protein content mg$_{BSA}$/g	Immobilization yield[a], %
TEOS/EtOH	2.68	5.72	3.48
TEOS/EG	4.40	8.27	15.95
TMOS/EtOH	1.80	4.59	2.75
TMOS/EG	1.97	6.56	4.21
Alginate	12.88	7.92	25.50
TEOS/EG/ Alginate	6.32	9.12	11.22
TMOS/EG/ Alginate	7.52	8.88	17.11

[a]Immobilization yield (%) = 100.total units of immobilized enzyme / total units of native enzyme used for immobilization

Table 1. Entrapment of CMCase in silica, Ca-alginate and mixed gels

chemicals were obtained from local suppliers or were commercially available reagent grade products and were used without further purification. The *T. viride* CMGB 1 strain is preserved in the collection of the Industrial Microbiology Laboratory of USAMVB Timisoara. The *T. viride* CMGB 1 cells were cultured in solid state fermentation [4]. The aqueous extracted enzymatic preparation with CMCase activity was centrifuged (10 minutes, 4ºC, 6000 rpm) and lyophilized (24 h, -56ºC, iLShin Europe Dry Freezer).

Immobilization methods

1. Enzyme solution (0.7 mL, 40 units) and NaF (50 µL, 1 M) were added to a sol obtained from TEOS or TMOS (3 mmol), alcohol (0.5 mL EtOH or EG) and HCl (10 µL, 0.1 N). The obtained gel was aged (24 h, 4°C), washed (5 mL hexane) and dried at vacuum [5].

2. A mix of sodium alginate (1.18 mL, 2%) and enzyme solution (0.7 mL, 40 units) was dropped in a 0.2 M CaCl$_2$ solution. The pearls (2 mm diameter) were washed with Millipore water and used as wet gels [6].

3. The sol was partially replaced by natrium alginate (2%) solution, to obtain a final solution with a sol content of 4% [6]. Than the enzymes were immobilized and the pearls were treated as described in method 2.

Enzyme assay. The CMCase activity was measured according to the Petterson and Porath method (CMC substrate, DNS reagent) [7]. The protein content was assayed according to the Lowry method [8].

Stability test. The immobilized enzyme from *T. viride* (method 1 and 2, 600 mg) and CMC solution (5 mL, 1%, pH 4.6) were incubated at 50ºC for six cycles of 30 min. At the end of each cycle the CMCase activity was assayed and than the CMC solution was replaced with a fresh one.

Results

T. viride cellulase with CMCase activity (286.67 mmol·min^{-1}·g^{-1}) was immobilized by entrapment in two different sol-gels, using ethanol and EG as cosolvent for TEOS

T. viride CMCase	Free	TEOS/EtOH based sol-gel
Optimum pH	3.0	4.0-5.0
Optimum temperature, °C	50-70	50-75
V_{max}, $mmol_{glucose}/mL\cdot min$	0.95	0.89
K_M, mg_{CMC}/mL	6.10	7.85

Table 2. Functional parameters of free and immobilized anzymes

Gel precursor	Relative CMCase activity, %					
Cycle	I	II	III	IV	V	VI
Alginate beads	57.59	31.42	10.59	8.83	8.16	6.62
TEOS/EG silica gel	54.35	18.70	8.67	6.96	5.65	5.42

Table 3. Cyclic use of immobilized CMCase

and TMOS. For comparison the enzyme was immobilized in Ca-alginate beads also (Table 1).

TEOS and EG used as precursor and cosolvent respectively leaded to better activities and immobilization yields than TMOS and ethanol, due to different physico-chemical properties of the matrix (according to SEM, BET, IR and thermal analysis, data not shown here). Ca-alginate gels gave the best results. But alginate gels are more leachable than silica gels. For this reason we entrapped the *T. viride* enzyme in mixed silica/alginate gels. The CMCase activity of enzymes entrapped in mixed gels was higher than in silica gels.

The main properties of free and entrapped enzyme in TEOS/EtOH based sol-gel are shown in Table 2, as described in [9]. Optimum pH and temperature are slightly shifted to higher values. A decrease of V_{max} and an increase in K_M is observed after immobilization, leading to a decrease of overall catalytic efficiency (65.55 %). This has to be overcome by the stabilizing effect of immobilization.

To test the stability of the immobilized *T. viride* CMCase, the alginate beads and the TEOS/EG-derived gels were reused in six operational cycles, in the presence of CMC solution (Table 3).

During the first two operational cycles the most amount of immobilized enzyme was released. Starting with the third cycle, an operational stabilization is observed.

Conclusions

Even though an efficient immobilization of enzymes having macromolecular substrates is a difficult task, our results suggest that matrixes with mesoporous structures may allow substrates to migrate to the active site of the enzyme, in a hydrophilic environment. Optimization of surface parameters is necessary to control the enzyme leakage. Mixed gels can be effective alternatives, when valuable enzymes are used.

Our studies suggest also that EG is a good solvent for TEOS or TMOS as sol-gel precursors and a protective environment for the enzyme molecule.

Acknowledgement

References

[1] J.Y. ZHU, X.J. PAN, Woody biomass pretreatment for cellulosic ethanol production: technology and energy consumption evaluation Bioresource Technology, 101, 4992-5002, 2010.

[2] M. K. BHAT, Cellulases and related enzymes in biotechnology, Biotechnol. Adv., 18(5), 355-383, 2000.

[3] T. CORADIN, J. ALLOUCHE, M. BOISSIÈRE, J. LIVAGE, Sol-Gel Biopolymer/Silica Nanocomposites in Biotechnology**,** Current Nanoscience, 2(3), 1-12, 2006.

[4] T. VINTILĂ, M. DRAGOMIRESCU, S. JURCOANE, D. VINTILA, R. CAPRITA, M. MANIU, Production of cellulase by submerged and solid-state cultures and yeasts selection for conversion of lignocellulose to ethanol, **Rom. Biotechnol. Lett.,** 14(2), 4275-4281, 2009

[5] M.T. REETZ, P. TIELMANN, W. WIESENHÖFER, W. KÖNEN, A. ZONTA, Second generation sol-gel encapsulated lipases: robust heterogeneous biocatalysts, Adv. Synt. Catal. 345, 717-728, 2003

[6] Z. KONSOULA, M. LIAKOPOULOU-KYRIAKIDES, Starch Hydrolysis by the action of an entrapped in alginate capsules α-amylase from Bacillus subtilis, Process Biochem. 41, 343–349, 2006

[7] D. IORDACHESCU, I. F. DUMITRU, Biochimie practica, Tipografia Universitatii Bucuresti, Bucuresti, 1980

[8] O.H. LOWRY, N.J. ROZBROUGH, L.A. PAN, R.J. RANDALL, Protein measurement with the Folin phenol reagent, J. Biol. Chem. 193, 265-275, 1951

[9] M. DRAGOMIRESCU, T. VINTILA, G. PREDA, Entrapment of microbial amylases and cellulases in silica-gels, Rev.Roum.Chim., submitted

SDSL-EPR as a tool for grasping topological information on the interaction between proteins and nanoparticles

Ghibaudi E.M.[1], Boscolo B.[1], Turci F.[1,2], Fenoglio I.[1,2], Fubini B.[1,2]

[1]*Dept.Inorganic, Physical and Material Chemistry, University of Torino, Via Giuria 7 I-10125, Torino, Italy; elena.ghibaudi@unito.it*
[2]*Center "G. Scansetti" for Studies on Asbestos and other Toxic Particulates, University of Torino, Via Giuria 7 I-10125, Torino, Italy*

Summary

The main event associated with the interaction of nanoparticles with biological fluids is the formation of a protein corona. Predicting the fate of NPs in biological environments implies a thorough characterization of such protein layer in terms of chemical composition of the NP surface as well as structural characterization. Both the changes in protein fold and the selective orientation of proteins onto NPs may influence the final outcome of NP in the body. In this paper we provide some examples of how EPR spectroscopy coupled to site-directed spin-labeling (SDSL) may shed light on these specific aspects related to the protein adsorption mechanisms.

Introduction

Any attempt to predict the effect and the fate of nanoparticles (NPs) inside biological systems implies a thorough knowledge of the phenomena occurring at the interface between NPs and biological media, in order to spot the chemico-physical determinants of such events [1]. A NP in contact with a biological fluid is quickly covered by a layer of proteins found in the medium, known as "protein corona". As the cell "sees" protein-coated NPs rather than bare NPs, the chemical and topological characterization of the protein corona is essential to understand the mode of interaction of NPs with cells, hence to predict the fate of NPs inside cells [2].

Adsorption may perturb the protein structure

Protein adsorption onto solid surfaces may bring about structural perturbations that result in modifications of the protein activity or may affect molecular recognition proc-

esses. Changes of the folding state of the adsorbed proteins are influenced by several factors [1]: i) the intrinsic protein stability (related with the hard or soft character of the protein [2]); ii) the characteristics of the sorbent surface (i.e. the presence of chemical moieties able to establish specific chemical and or physical interactions with the proteins (e.g., surface hydrophobicity seems to relate with the ability of bringing about irreversible folding changes); iii) the surface curvature (large interaction area between the protein and the NP has been reported to affect the secondary structure more than a small one [3,4]); iv) the protein concentration at the surface (molecular crowding influences both the extent and the kinetic of unfolding of the adsorbed proteins, due to protein-protein interactions); v) pH and ionic strength.

The importance of protein orientation in the adsorption phenomena

The orientation of proteins with respect to the surface is an often neglected aspect in adsorption studies. Even if the general fold of a protein is not compromised, the interaction with the surface may hinder the entrance of the enzyme substrate channel or may hide epitopes of proteins involved in molecular recognition processes.

Site-directed spin-labeling (SDSL) associated with electron paramagnetic resonance (EPR) is a unique tool for getting information on molecular orientation as EPR is one of the few biophysical techniques sensitive to orientational disorder. The technique was developed in the late '90 [5] and has been applied in structural biology for the investigation of the conformational dynamics of proteins and nucleic acids in solution and for assessing the orientation of proteins in membranes. In spite of its potentialities, however, this strategy has not yet been fully exploited for investigating the phenomena that occur upon protein adsorption onto solid surfaces. This approach is based on the conjugation of a specific protein site with a spin-label, which acts as a probe of its local environment. The labelling site may be naturally present in the protein or introduced by site-directed mutagenesis and it is usually, but not necessarily, a Cys.

The Continuous Wave EPR spectrum associated with the label reflects its degree of rotational freedom. Any perturbation undergone by the local environment of the paramagnetic probe may affect the motional state of the spin label and reflects on the EPR pattern. The parameters that can be extracted from spectral analysis and de-convolution are: the number of spectral components; their relative weight; the order parameter (that quantifies the isotropic character of each component and provides a measure of the degree of order in the system); the rotational correlation time (related with the tumbling rate of the spin-label).

SDSL-EPR in protein adsorption studies onto solid surfaces

Only few cases of SDSL-EPR studies on the orientation of proteins adsorbed onto solid surfaces are reported in the literature.

Nicholov et al. applied this strategy to BSA and HSA [6,7] interacting with controlled pore glass beads and polystirene beads. In both cases 3-(maleimidomethyl)-proxyl was conjugated to Cys34 and the authors were able to show that the protein region involved in the interaction with solid surface does not lie close to the labelling site. In addition, unfolding of HSA adsorbed onto polystyrene-butadiene beads at pH 7.0
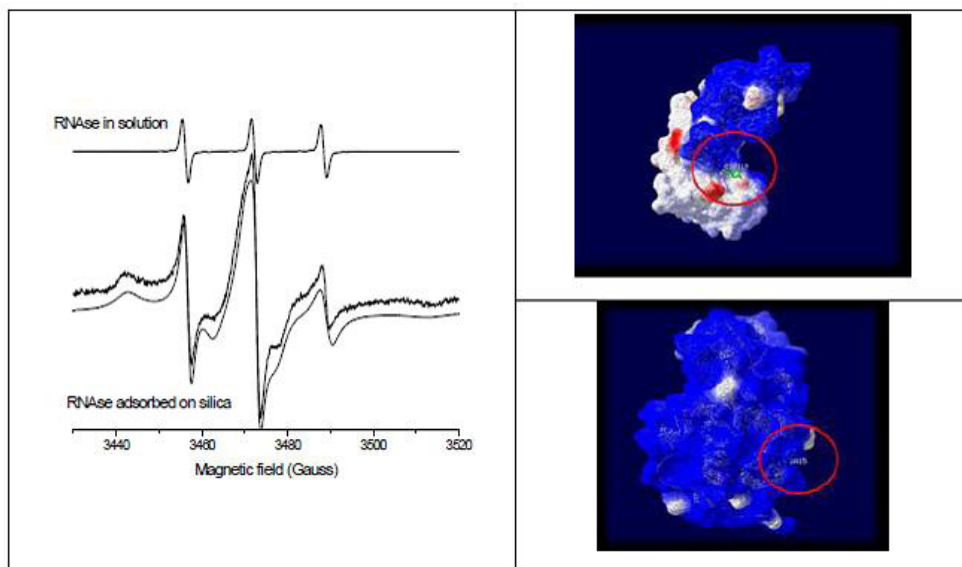
Figure 1: Left: EPR spectra of His119-labelled RNase in solution (top) and adsorbed on silica NPs (bottom) [9]; Right: the structure of RNase (top) and lysozyme (bottom) and their labeling sites

was shown to occur as a consequence of coulombic interactions between the protein and the negatively charged surface.

Jacobsen et al. [8] investigated the orientation and structural changes of a series of T4 lysozyme mutants adsorbed on planar quartz-supported lipid bilayer. They were able to reveal a global conservation of the secondary and tertiary structure of T4L upon adsorption. In addition, the orientation of the entire protein was deduced on the basis of an anisotropic motional model for the spin-labeled side chain and - based on the comparison of EPR spectra - the authors were able to show that the C-terminal part of the protein is actively involved in the adsorption process.

Finally, our group employed SDSL–EPR to investigate the interaction of lysozyme and ribonuclease with nanostructured silica particles [9] (Fig.1). Lysozyme was labelled on His15 and RNase on His119: both residues are exposed on the protein surface. EPR provided clear evidence that both proteins bind to the surface through the labelled-region, although with distinct adsorption modes. In fact, based on the spectral parameters, the labelled domain of lysozyme was shown to adhere quite flatly to the silica NP, whereas RNase adsorption results in a probe-containing cavity that is almost inaccessible from the outside, but it still assures a certain degree of motional freedom to the spin-probe trapped inside. In both cases, some protein desorption occurred with time; in the case of RNase, some structural rearrangements of the adsorbed molecules is likely to occur.

References

[1] Fenoglio I., Fubini B., Ghibaudi E.M., Turci F. Multiple aspects of the interaction of biomacromolecules with inorganic surfaces Adv.Drug Deliv.Rev., 2011, in press.

[2] Norde W., My voyage of discovery to proteins in flatland and beyond, Coll.Surf.B-Biointerfaces, 61, 1-9, 2008

[3] Lynch I., Dawson K.A., Protein-nanoparticle interactions, Nano Today, 3, 40-47, 2008.

[4] Lundqvist M., Sethson I., Jonsson B.H., Protein adsorption onto silica nanoparticles: Conformational changes depend on the particles' curvature and the protein stability, Langmuir, 20, 10639-10647, 2004

[5] Hubbell W.L., Cafiso D.S., Altenbach C., Identifying conformational changes with site-directed spin labeling, Nature Struct.Biol., 7, 735-739, 2000.

[6] Nicholov R. Protein adsorption at the solid/liquid interface monitored by ESR spectroscopy. Coll.and Surf.A: Physicochem. and Engineer. Aspects, 70, 159-166, 1993.

[7] Nicholov R. HSA adsorption at solid-liquid interface monitored by ESR spectroscopy in Proteins at Interfaces: Fundamentals and applications, ACS Symposium Series, 602, 280-295, 1995.

[8] Jacobsen K., Hubbell W.L., Ernst O.P., Risse T., Details of the partial unfolding of T4 lysozyme on quartz using site-directed spin labeling, Angew. Chem., 45, 3874-3877, 2006.

[9] Turci F., Ghibaudi E., Colonna M., Boscolo B., Fenoglio I., Fubini B., An Integrated Approach to the Study of the Interaction between Proteins and Nanoparticles Langmuir, 26, 8336-8346, 2010.

Mechanism of the Uranyl-Transferrin Complex Formation. Uranium Uptake by Transferrin.

Hémadi M., Ha-Duong N. T. and El Hage Chahine J. M.

Univ Paris Diderot, Sorbonne Paris Cité, ITODYS, UMR 7086 CNRS, 15 rue J-A de Baïf, 75205 Paris Cedex 13, France

Summary:

Uranium is a toxic heavy metal, the investigation of its incorporation and transport in biological media is of considerable public health interest. In vitro, uranyl is transferred from one of the major plasma complexes, $UO_2(CO_3)_3^{4-}$ to Transferrin (T) in four kinetic steps. The first is very fast and accompanied by HCO_3^- loss. It yields a first intermediate ternary complex between $UO_2(CO_3)_2^{2-}$ and the C-lobe of T; k_1: $(7.0 \pm 0.4) \times 10^5$ M^{-1} s^{-1}; $k_{-1} = (4.6 \pm 0.2) \times 10^3$ M^{-1} s^{-1}; $K_1 = (6.7 \pm 0.6) \times 10^{-3}$. This first kinetic product undertakes a fast rate-limiting conformation change leading to the loss of a second HCO_3^-: $k_2 = (33 \pm 14)$ s^{-1}. This second ternary complex undergoes in turn two very slow conformation changes, at the end of which both the C- and N-lobes become loaded with uranyl. When unexposed to uranium, the uranyl concentrations in the bloodstream are much too low to favor receptor-mediated transport. However, in the case of exposure, these concentrations can grow considerably. This added to the fast uranyl complex formation with the C-lobe and the fast interaction of the $T(UO_2)_2$ with the receptor can allow a possible internalization in the cell by the iron-acquisition pathway.

Introduction

Iron is an indispensable trace element that plays an important role in the basic metabolism of all living species. However, in nature iron exists as Fe(III), which is not soluble in neutral media and, therefore, not bioavailable. In order to acquire it, vertebrates and invertebrates use "transferrin". In mammals, iron acquisition is mediated by transferrin-receptor endocytosis [1]. Human serum transferrin is an 80 kD a bilobal protein. Each lobe (–N and –C) contains an iron binding site in which iron is coordinated to four protein ligands: one histidine, one aspartate, two tyrosines as well as a synergistic carbonate anion without which, the protein loses its affinity for iron [2]. Iron free transferrin or apotransferrin (T) is in the so-called open conformation.

When T becomes iron loaded (TFe$_2$), its conformation changes from "opened" to "closed" [3]. The transferrin receptor 1 (TFR) is a homodimeric 190 kDa glycosylated transmembrane protein arranged in two identical subunits which are linked by two disulfide bridges. Each of the two subunits consists of a transmembrane endodomain and an ectodmain directed toward the biological fluid and responsible of the interaction with T [4].

T in the bloodstream binds iron. Iron-loaded transferrin interacts then with receptor 1 at the cell surface and the TFR-TFe$_2$ adduct is internalized via endocytosis. Following the internalization, the endosome is acidified, leading to iron release. The apotransferrin-receptor 1 adduct is afterward recycled back to the cell surface, where T is released ready for another cycle of iron transport. T recycling takes between 4-15 minutes [5].

In serum, only about 30% of T is complexed with iron. The remaining protein has then the capacity to bind other metals than iron. As a matter of fact, T forms stable complexes with more than 40 different metals such as, Al^{3+}, Ga^{3+}, Co^{3+}, Bi^{3+}, Ru^{3+}, etc[6].

At least two essential steps are required for a metal to be transported by the main iron acquisition pathway: 1-formation of a strong complex between T and metal. 2-Interaction of the metal loaded T with receptor 1.

In this chemical relaxation and thermodynamic assay, uranium transport via the iron acquisition pathway is investigated. Uranium is the second most common naturally occurring actinide [7]. It is highly toxic in all its oxidation states. It also accumulates in the brain and causes serious damage to bones and kidneys. Uranium is mainly present in aqueous and biological media, as the uranyl ion (UO_2^{2+}, U(VI)) [8].

Materials and Methods

Protein preparation: Uranyl loaded T is prepared as described elsewhere [9]. The complete receptor 1 including the ectodomain is extracted from human placenta and purified according to published procedures [10]. The methods and techniques of chemical relaxation are explained elsewhere [11].

Results

When a solution of apotransferrin is mixed with a solution of uranyl in the presence of HCO_3^-, four kinetic processes are observed (Fig. 1). The first occurs in the range of tens of milliseconds and leads to a first kinetic intermediate. The second process occurs in the range of seconds and leads to a second kinetic intermediate. These two processes are characterized by exponential decreases in fluorescence and are followed by two slow kinetic phenomena. The third process occurs in the thousands seconds range and the fourth lasts about twenty thousand seconds. Both are characterized by exponential increases in absorption.

First kinetic process

The first kinetic process (Fig. 1A) depends on c_0 (apotransferrin concentration), c_1 (uranyl carbonate concentration), $[HCO_3^-]$ and pH. It involves the C-site (T$_C$) and the carbonated metal species. In neutral media and in the presence of carbonate, two uranyl carbonate complexes coexist: $UO_2(CO_3)_2^{2-}$ and $UO_2(CO_3)_3^{4-}$ (eq 1)[9].
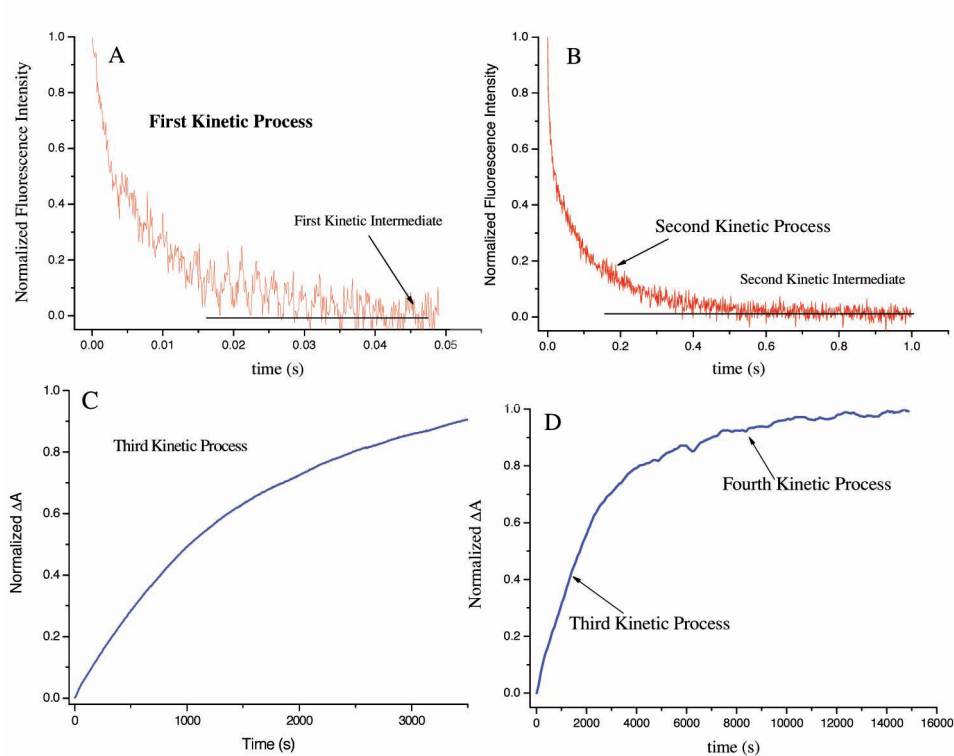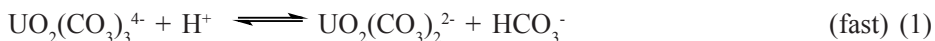
Figure 1: Variation of the normalized fluorescence intensity (A, B for λ_{ex} 280 nm and $\lambda_{em} \geq 310$ nm) and of the normalized differential absorption (C, D) with time when a solution of apotransferrin (T) (A, B: $c_0 = 6$ µM ; C, D: $c_0 = 2$ µM) is mixed with a solution of uranyl (A, B: $c_1 = 30$ µM ; C, D: $c_1 = 20$ µM) at pH 8.3 for A, B and pH 7.7 for C, D at 25 ± 0.5 °C with $[HCO_3^-] = 20$ mM and $\mu = 0.2$.

$$UO_2(CO_3)_3^{4-} + H^+ \rightleftharpoons UO_2(CO_3)_2^{2-} + HCO_3^- \qquad \text{(fast) (1)}$$

We show that the first process describes eq 2 in which T_C reacts with $UO_2(CO_3)_3^{4-}$ to yield the ternary complex kinetic intermediate T_CUO_2Z:

$$UO_2(CO_3)_3^{4-} + TC \underset{k_{-1}}{\overset{k_1}{\rightleftharpoons}} T_CUO_2Z + HCO_3^- \qquad \text{(rate-limiting) (2)}$$

with $K_{2a} = [UO_2(CO_3)_3^{4-}][H^+]/[UO_2(CO_3)_2^{2-}][HCO_3^-]$ and $K_1 = [UO_2(CO_3)_3^{4-}][T_C] / [T_CUO_2Z][HCO_3^-]$.

Indeed, the experimental data obey reciprocal relaxation time equation 3, which is associated with reaction 2.

$$\tau_1^{-1}/[HCO_3^-] = k_1 K_{2a} c_1 /([H^+] + K_{2a}[HCO_3^-]) + k_{-1} \qquad (3)$$

A good linear least-squares regression of the data against eq 3 is obtained (Fig. 2). From the slope and intercept of the best line, $k_1 = (7.0 \pm 0.4) \times 10^5$ M^{-1} s^{-1} and $k_{-1} = (4.7 \pm 0.2) \times 10^3$ M^{-1} s^{-1} and $K_1 = (6.7 \pm 0.6) \times 10^{-3}$ are determined.
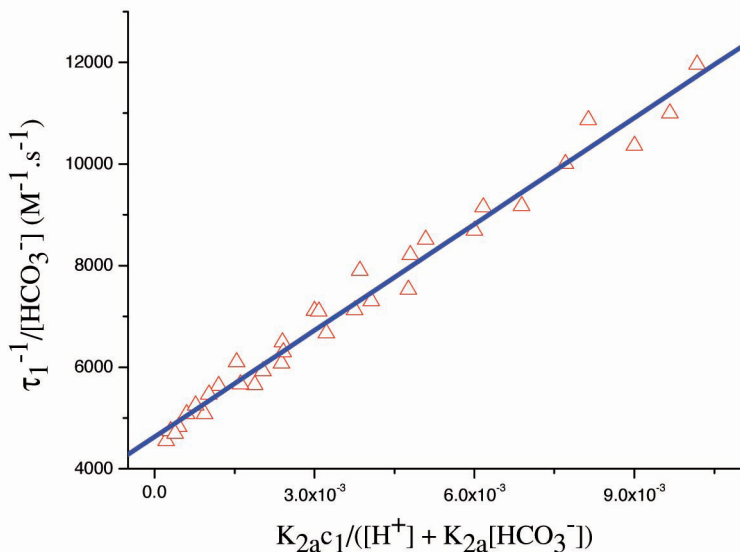
Figure 2: Plot of $\tau_1^{-1}/[HCO_3^-]$ against $K_{2a} c_1/(([H^+] + K_{2a}) [HCO_3^-])$. Intercept, $(4.7 \pm 0.2) \times 10^3$ $M^{-1}.s^{-1}$; slope, $(7.0 \pm 0.4) \times 10^5$ $M^{-1}.s^{-1}$, $r = 0.99062$.

Second kinetic process

The second kinetic process (Fig. 1B) depends on c_1, $[HCO_3^-]$ and pH. It is not observed with a C-lobe iron-loaded T. It describes a rate-limiting change in the conformation of the first kinetic intermediate accompanied by the loss of a second HCO_3^- (eqs 4 and 5):

$$T_C UO_2 Z \underset{k_{-2}}{\overset{k_2}{\rightleftharpoons}} T_C UO_2' \qquad \text{(rate-limiting) (4)}$$

$$T_C UO_2' \rightleftharpoons T_C UO_2 + HCO_3^- \qquad (5)$$

with $K_3 = [T_C UO_2][HCO_3^-]/[T_C UO_2']$ and $K_2 = [T_C UO_2']/[T_C UO_2 Z]$

where $T_C UO_2'$ is a kinetic intermediate and $T_C UO_2$ is a kinetic product, in which the C-site is coordinated to one carbonated uranyl.

The experimental data associated with this process obey eq 6 , which is related to rate-limiting eq 4.

$$\tau_2^{-1} = k_{-2}[HCO_3^-]/K_3 + k_2 c_1 \alpha (K_3 + [HCO_3^-])/[(c_1 \alpha + K_1[HCO_3^-])K_3] \qquad (6)$$

Indeed, a good linear regression against eq 6 is obtained (Fig. 3). This allows the determination of $k_{-2}/K_3 = (766 \pm 56)$ M^{-1} s^{-1} and $k_2 = (33 \pm 14)$ s^{-1}, which leads to the overall equilibrium constant involved in the second bicarbonate loss: $K_3 K_2 = [T_C UO_2][HCO_3^-]/[T_C UO_2 Z] \approx (0.04 \pm 0.01)$ M. The $K_3 K_2$ value implies that at the end of the second kinetic process, 70% to 80% of the C-lobe of T is loaded with uranyl.

Third and Fourth kinetic processes

The two slow phenomena (Figs 1C and 1D) are independent of all experimental
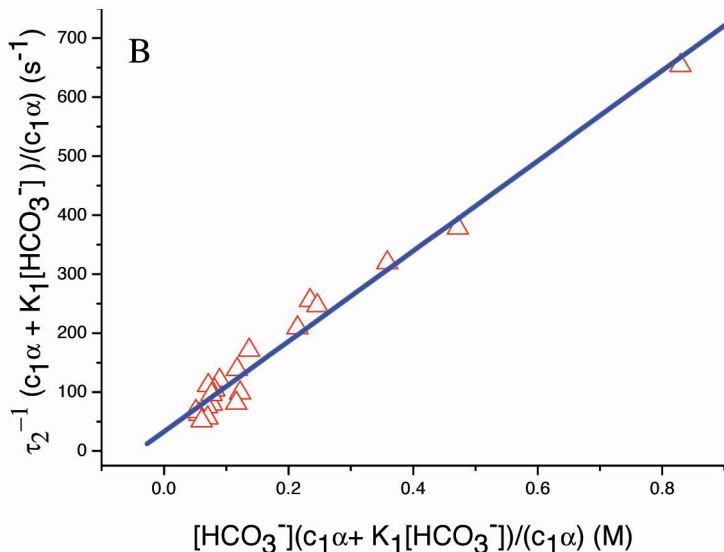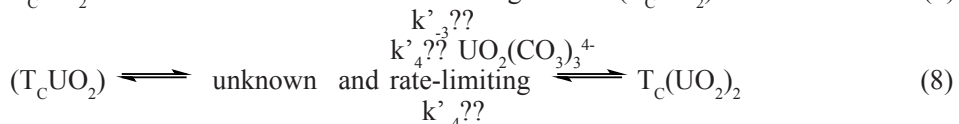
Figure 3: Plot of τ_2^{-1} $(c_1\alpha + K_1[HCO_3^-])/(c_1\alpha)$ against $[HCO_3^-](c_1\alpha + K_1[HCO_3^-])/(c_1\alpha)$. Intercept, (33 ± 14) s^{-1} ; slope, (766 ± 56) $M^{-1}.s^{-1}$; $r = 0.98772$.

parameters. Furthermore, at the end of the final phenomenon, the protein becomes saturated with uranyl. These two processes describe changes in the conformation of the protein which rate-controls uranyl uptake by the N-lobe (eqs 7 and 8):

$$T_C UO_2 \underset{k'_{-3}??}{\overset{k'_3??}{\rightleftharpoons}} \text{unknown and rate-limiting} \rightleftharpoons (T_C UO_2) \qquad (7)$$

$$(T_C UO_2) \underset{k'_{-4}??}{\overset{k'_4?? \; UO_2(CO_3)_3^{4-}}{\rightleftharpoons}} \text{unknown and rate-limiting} \rightleftharpoons T_C(UO_2)_2 \qquad (8)$$
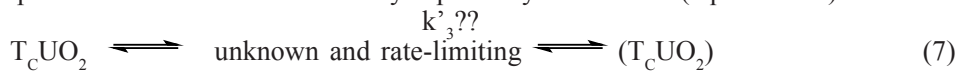
The reciprocal relaxation time associated with equations 7 and 8 can be expressed as eqs 9 and 10. These two equations are independent of the concentrations of the species present in the medium:

$$\tau_3 \approx k'_{-3} + k'_3 \qquad (9)$$
$$\tau_4 \approx k'_{-4} + k'_4 \qquad (10)$$

Discussion

Both Uranyl and iron uptakes occur in four kinetic steps (Fig. 4). The first step in iron uptake by T consists of a metal transfer from an Fe(III) chelator to the C-lobe in interaction with synergistic hydrogencarbonate.[12] However, with $UO_2(CO_3)_3^{4-}$, a first ternary complex involving the loss of one hydrogencarbonate occurs very rapidly with the C-lobe (eq 2). This first kinetic product loses another hydrogencarbonate to yield a second ternary complex (eq 5). The latter undergoes a series of changes in conformation, which rate-control a second uranyl uptake by the N-lobe and lead to the final thermodynamic product (eqs 7 and 8). In the case of iron, the third and

Figure 4: Mechanisms of uranyl and iron uptake by transferrin.
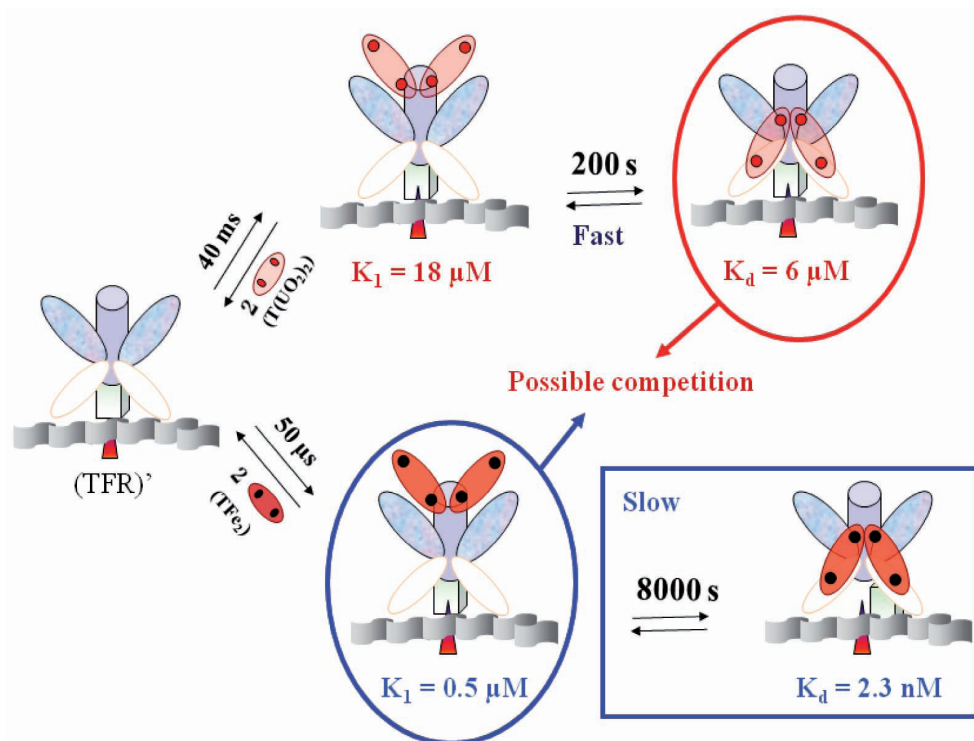
Figure 5: Competition between TFe_2 and $T(UO_2)_2$ towards the interaction with TFR.

fourth steps are much faster and lead to a second iron uptake by the N-lobe of T. The affinities involved are largely in favor of iron (logK: 22 for iron and 13 for uranyl) [13]. This can be explained by the fact that the structure of $T(UO_2)_2$ is different from that of TFe_2 because of the size of the uranyl group. The complexation cavity in $T(UO_2)_2$ is not in fully closed conformation and uranyl is partly in contact with bulk medium [14].

Uranyl forms a stable complex with T, which constitutes the first condition required for its transport by the iron acquisition pathway. In a recent article, we showed that the uranyl-loaded T interacts with transferrin receptor 1 in about 200 s and in two steps with an overall dissociation constant $K_D(TFR\text{-}T(UO_2)_2) = 6$ µM (Fig. 5). We have also shown that TFe_2 interacts with TFR in two steps, the first occurs in 50 µs and corresponds to the interaction of the C-lobe whereas the second occurs in two hours and corresponds to that of the N-lobe. The dissociation constant involved with the first process is of 0.5 µM [15]. T recycling via receptor mediated endocytosis lasts a few minutes. This implies that TFe_2 is internalized in the cytosol with mainly its C-lobe interacting with TFR. In this case a possible competition becomes possible between $T(UO_2)_2$ and TFe_2 towards the interaction with receptor 1 (Fig. 5) [16]. This associated to the fact that 70% of the circulating T is iron-free indicate that in the case of a strong contamination by uranium, the latter can enter the cells via the iron-acquisition pathway.

References

1. Ward, R. J.; Zhang, Y.; Crichton, R. R., Aluminium toxicity and iron homeostasis. *J Inorg Biochem* **2001,** *87* (1-2), 9-14.

2. MacGillivray, R. T.; Mendez, E.; Shewale, J. G.; Sinha, S. K.; Lineback-Zins, J.; Brew, K., The primary structure of human serum transferrin. The structures of seven cyanogen bromide fragments and the assembly of the complete structure. *J Biol Chem* **1983,** *258* (6), 3543-53.

3. (a) Wally, J.; Halbrooks, P. J.; Vonrhein, C.; Rould, M. A.; Everse, S. J.; Mason, A. B.; Buchanan, S. K., The crystal structure of iron-free human serum transferrin provides insight into inter-lobe communication and receptor binding. *J Biol Chem* **2006,** *281*, 24934-24944; (b) Zuccola, H. J., *The crystal structure of monoferric human serum transferrin, Ph. D. Thesis*. Ann Arbor, 1992.

4. Lawrence, C. M.; Ray, S.; Babyonyshev, M.; Galluser, R.; Borhani, D. W.; Harrison, S. C., Crystal structure of the ectodomain of human transferrin receptor. *Science* **1999,** *286* (5440), 779-82.

5. Dautry-Varsat, A.; Ciechanover, A.; Lodish, H. F., pH and the recycling of transferrin during receptor-mediated endocytosis. *Proc Natl Acad Sci U S A* **1983,** *80* (8), 2258-62.

6. Ha-Duong, N. T.; Hemadi, M.; Chikh, Z.; Chahine, J. M., Kinetics and thermodynamics of metal-loaded transferrins: transferrin receptor 1 interactions. *Biochem Soc Trans* **2008,** *36* (Pt 6), 1422-6.

7. Lestaevel, P.; Bussy, C.; Paquet, F.; Dhieux, B.; Clarencon, D.; Houpert, P.; Gourmelon, P., Changes in sleep-wake cycle after chronic exposure to uranium in rats. *Neurotoxicol Teratol* **2005,** *27* (6), 835-40.

8. Sutton, M.; Burastero, S. R., Uranium(VI) solubility and speciation in simulated elemental human biological fluids. *Chem Res Toxicol* **2004,** *17* (11), 1468-80.

9. Hemadi, M.; Ha-Duong, N. T.; El Hage Chahine, J. M., Can Uranium Be Transported by the Iron-Acquisition Pathway? Ur Uptake by Transferrin. *J Phys Chem B* **2011**.

10. Hemadi, M.; Kahn, P. H.; Miquel, G.; El Hage Chahine, J. M., Transferrin's mechanism of interaction with receptor 1. *Biochemistry* **2004,** *43* (6), 1736-45.

11. Eigen, M., Nobel Lecture. **1967**.

12. Pakdaman, R.; Bou Abdallah, F. B.; El Hage Chahine, J. M., Transferrin, is a mixed chelate-protein ternary complex involved in the mechanism of iron uptake by serum-transferrin in vitro? *J Mol Biol* **1999,** *293* (5), 1273-84.

13. Averseng, O.; Hagege, A.; Taran, F.; Vidaud, C., Surface Plasmon Resonance for Rapid Screening of Uranyl Affine Proteins. *Anal Chem* **2010,** *82* (23), 9797-9802.

14. Vidaud, C.; Gourion-Arsiquaud, S.; Rollin-Genetet, F.; Torne-Celer, C.; Plantevin, S.; Pible, O.; Berthomieu, C.; Quemeneur, E., Structural consequences of binding of UO2(2+) to apotransferrin: can this protein account for entry of uranium into human cells? *Biochemistry* **2007,** *46* (8), 2215-26.

15. Mukhopadhyay, C. K.; Mazumder, B.; Lindley, P. F.; Fox, P. L., Identification of the prooxidant site of human ceruloplasmin: a model for oxidative damage by copper bound to protein surfaces. *Proc Natl Acad Sci U S A* **1997,** *94* (21), 11546-51.

16. Hemadi, M.; Ha-Duong, N. T.; Plantevin, S.; Vidaud, C.; El Hage Chahine, J. M., Can uranium follow the iron-acquisition pathway? Interaction of uranyl-loaded transferrin with receptor 1. *J Biol Inorg Chem* **2010,** *15* (4), 497-504.

A Theoretical Study on Aβ₄₂ Oligomers, the Effectors in Alzheimer's Disease

Horn Anselm H. C., Sticht Heinrich

Bioinformatik, Institut für Biochemie, Emil-Fischer-Zentrum,
Friedrich-Alexander-Universität Erlangen-Nürnberg
Fahrstr. 17, 91054 Erlangen, Germany

Summary

We studied the stability of Aβ42 oligomers (monomer through pentamer) by means of molecular dynamics simulations starting from the experimentally known fibrillar structure. While the monomer lost its initial U-shaped conformation and formed an antiparallel β-sheet, the trimer to pentamer retained their fibril conformation with two parallel β-sheets, although they exhibited a significant flexibility at the C-terminal β-sheet. The Aβ42 dimer adopted a barrel-like structure with both parallel and antiparallel β-sheet elements thus shielding the central hydrophobic core (L17, F19, A21).

Introduction

Alzheimer's disease (AD) has evolved a major threat to public health in modern society. AD belongs to a group of neuropathological disorders, where conformational changes of an otherwise soluble peptide lead to a refolded compound that in turn aggregates into oligomers, filaments and fibrils accumulating in plaques in the brain of patients. However, AD's nature is still not fully understood and a viable medication is not available.

The experimentally determined structures of Aβ40 and Aβ42 in the fibril state consistently reveal two β-strands connected by a turn, thus forming a U-shaped topology (Fig. 1A). The monomeric Aβ subunits form a longitudinal stack, thus creating parallel in-register β-sheets (Fig. 1B) and growth can proceed longitudinally and laterally. Originally, the fibrillar structures were assumed to be the neurotoxic species, but converging lines of evidence suggest that small soluble oligomers, especially Aβ dimers, are the disease mediating substances, that can be enriched by dissolving the non-toxic fibrils.

Because their aggregation tendency renders experimental studies of small Aβ oligomers inherently difficult, molecular dynamics simulations are well suited to address this question.
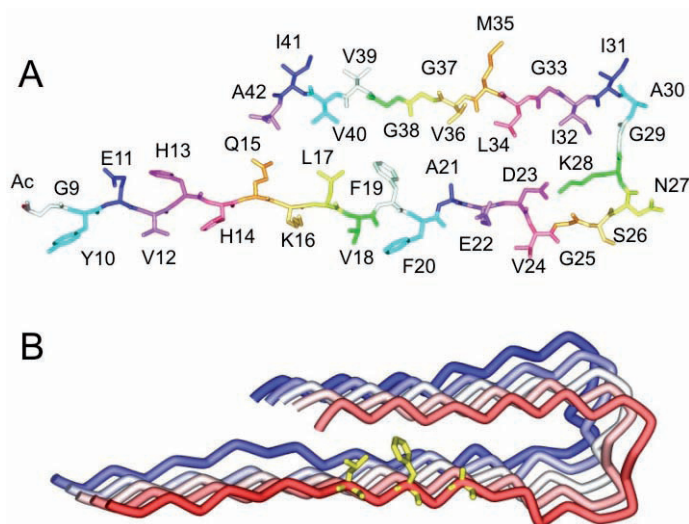
Figure 1 A) Sequence of monomeric Aβ9-42 in fibril conformation B) Aβ pentamer initial structure with CHC residues L17, F19, A21 of chain A in yellow sticks.
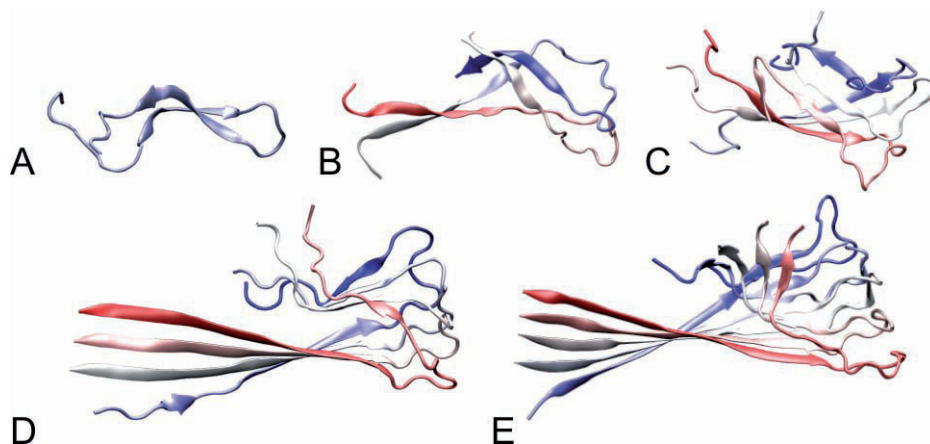
Figure 2 Representative structures for A) pentamer B) tetramer C) trimer, D) dimer, E) monomer obtained by hierarchical clustering.

Materials and Methods

The available pentameric Aβ17-42 protofibril structure was N-terminally extended to residue 9. From this Aβ pentamer the other oligomer structures were created. Molecular dynamics simulations were performed under standard NPT conditions in explicit solvent for at least 100 ns.[1]
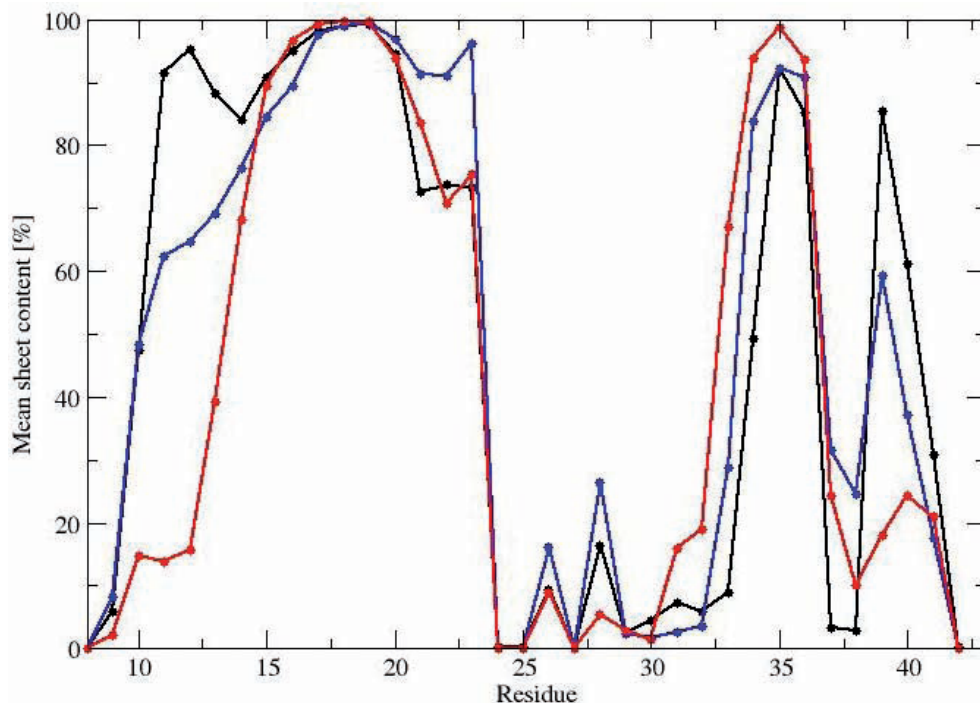
Figure 3 Mean β-sheet content (in %) of higher oligomers: pentamer (black), tetramer (blue), trimer (red).

Results

In the simulations, the higher oligomers (trimer, tetramer, pentamer) retained the main characteristics of the initial fibrillar conformation, i.e. the stack of β-sheets, the overall U-shaped topology and the turn-stabilizing bifurcated salt bridge D23-K28. While the N-terminal parallel β-sheet displayed a high structural stability, the C-terminal sheet showed an increased conformational flexibility at the diglycine motif G37-G38 leading to a pronounced kink at this position (Fig. 2C-E, Fig. 3).

The monomer, on the other hand, lost its initial fibrillar structure already in the early steps of the simulation, because stabilizing interactions between adjacent Aβ layers are missing. Instead, a β-hairpin with two antiparallel β-sheets (F19-V24, I31-V36) forms (Fig. 2A), in accord with other simulation studies.

For the dimer a distinct conformation is found that owns structural characteristics of both, the monomer and the higher oligomers. The initial U-shaped stack confor-mation evolves into a barrel-like structure by rotating the C-terminal β-strand of chain B towards its N-terminal counterpart. Thus, an antiparallel β-sheet is formed in addition to parallel β-sheet elements still present in the dimer (Fig. 2B). A further difference to the higher oligomers is the decreased population of the D23-K28 salt bridge, instead of which the new interaction D23-N27 is established not present in the fibril structure. Interestingly, this conformational change does not result in an increa-sed overall number of hydrogen bonds: antiparallel and parallel H-bond interactions
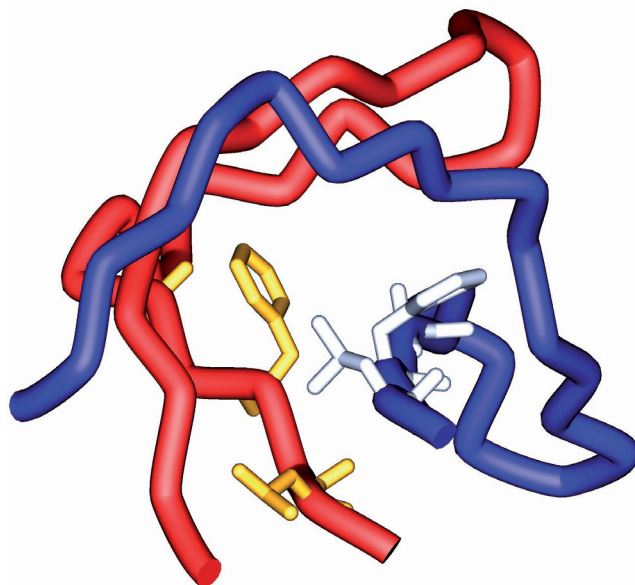
Figure 4 Shielding of the CHC in the barrel-like structure of the Aβ dimer (detail). Chain A: blue, chain B: red. CHC residues L17, F19, A21 are depicted in sticks.

together are constant during the simulation. However, the barrel-like structure shields the central hydrophobic core (CHC) residues of chain B as effectively as adjacent layers in higher oligomers protect the inner chains from the solvent (Fig. 4). The relevance of this conformation for neurotoxicity was proven by engineered disulfide bonds stabilizing either the N- or C-terminal sheet in the dimer (S8C, M35C). The thus stabilized dimer exhibits enhanced neurotoxicity.[2]

Conclusions

Our simulations reveal a structural explanation for the fact that higher oligomers (trimer, tetramer, pentamer) are effective seeds for fibril formation. The unique Aβ dimer conformation found seems to be related to the dimer's unique neurotoxicity. This structure served as basis for the design of stabilized Aβ oligomers to study their neurotoxicity and will aid the design of specific inhibitors.

References

[1] A. H. C. HORN, H. STICHT, Amyloid-β42 Oligomer Structures from Fibrils: A Systematic Molecular Dynamics Study, J. Phys. Chem. B, 114, 2219-2226, 2010. DOI 10.1021/jp100023q

[2] A. MÜLLER-SCHIFFMANN, A. ANDREYEVA, A. H. C. HORN, K. GOTTMANN, C. KORTH, H. STICHT, Molecular Engineering of a Secreted, Highly Homogeneous, and Neurotoxic Aβ Dimer, ACS Chem. Neurosci., 2, 242–248, 2011. DOI: 10.1021/cn200011h

Focused ligand libraries as tools for in silico design of anti-apoptotic proteins inhibitors

Colas C., Roussi F., Iorga B.I.*

Institut de Chimie des Substances Naturelles, CNRS UPR 2301, Centre de Recherche de Gif-sur-Yvette, Avenue de la Terrasse, 91198 Gif-sur-Yvette, France

Summary

The Bcl-2 family of proteins is involved in cell death regulation and encompasses both anti- and pro-apoptotic members.[1] In many cancers, the anti-apoptotic proteins Bcl-xL and Mcl-1 are overexpressed, which makes these proteins interesting drug targets. The development of new molecules mimicking the interactions of pro-apoptotic proteins with pro-survival proteins is thought to be the next step towards anticancer therapeutics development.

Meiogynine A, isolated recently from the bark of *Meiogyne cylindocarpa*,[2] has been shown to act as an antagonist of the Bcl-xL/Bak association.[3] The goal of the present project is the development, using molecular modelling techniques, of new active molecules derived from meiogynine A able to bind on Bcl-xL.

Introduction

Apoptosis is a critical process in the development of multicellular organisms, any deregulation of this process resulting in a variety of diseases. The proteins belonging to Bcl-2 family are important regulators of apoptosis, as they possess either anti- or pro-apoptotic functions. Anti-apoptotic proteins are localized in the mitochondrial outer membrane and are characterized by one to four homologous regions (BH1-4).[4] Pro-apoptotic proteins can be either multi-domain (Bak, Bax) or mono-domain (Bid, Bim, Noxa), the latter being also known as BH3-only proteins. The X-ray structure of Bcl-xL reveals that the BH domains form a hydrophobic groove that constitutes the binding site of the BH3 domain from the pro-apototic protein (Figure 1).[5]

It is believed that the pro-survival proteins (e.g. Bcl-xL, Bcl-2, Mcl-1) are in complex with different pro-apoptotic proteins (Bak, Bax) until a cytotoxic signal occurs.[6] This signal activates BH3-only proteins that can disrupt the complexes, thus releasing the pro-apoptotic proteins which are now free to accomplish their function. In many cancers, a surexpression of the pro-survival proteins leads to an accumulation of tu-
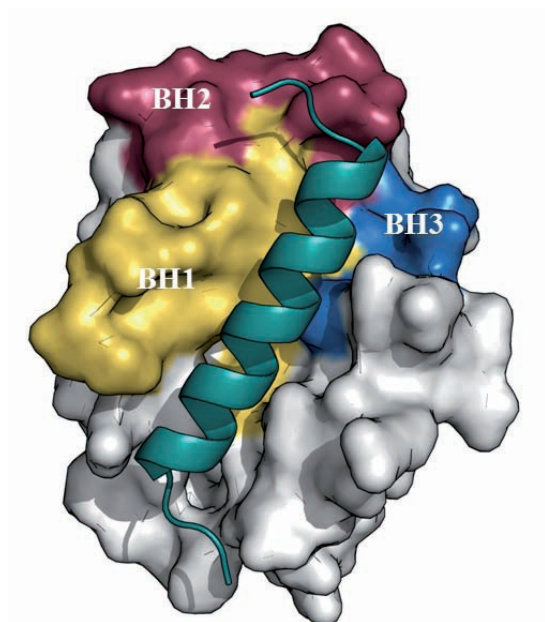
Figure 1: Binding groove of Bcl-xL (surface) in complex with the peptide Bim (cartoon).

mour cells and a resistance to chemotherapy, which makes these proteins interesting targets for the design of new anticancer drugs.

In this project, the structure of meiogynine A, an inhibitor of the interaction Bcl-xL/Bak, has been used for building focused ligand libraries. These libraries represent key tools for the design, using molecular modelling, of new active molecules with improved biological activity targeting this class of proteins.

Materials and Methods

Structural studies were performed *in silico* using representative X-ray structures of Bcl-xL: the apo form (1MAZ) and the complexes with ABT-737 (2YXJ), W119542 (3INQ) and the peptide Bim (3FDL). The fragment containing the helix α1 and the loop α1-α2 is not present in all X-ray structures available, and it was removed from all structures used in this study.

Molecular dynamics (MD) simulations were performed with GROMACS 4.5.4[7] using the OPLS-AA force filed.[8] Trajectories of 20 ns were produced in each case, the root mean square fluctuation (RMSF) calculated with g_rmsf module and plotted as B-factors using Pymol.[9] All MD simulations were concatenated and clustered with the g_cluster module, in order to generate an ensemble containing 40 representative protein conformations, to be used for the subsequent molecular docking step.

Three-dimensional structures of meiogynine A and its diastereoisomers were gene-rated with Corina[10] and then used in flexible docking with Gold 5.0[11] on the ensemble of conformers generated previously. The binding site was defined as a sphere with
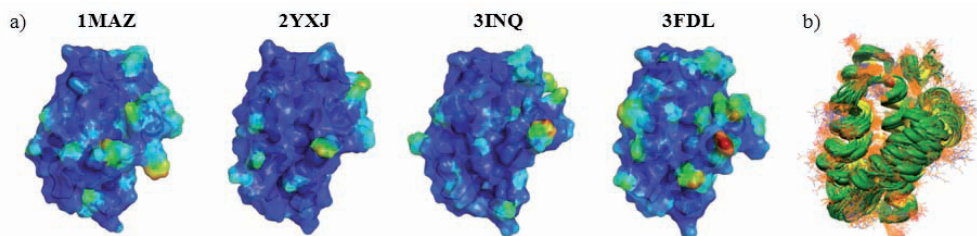
Figure 2: a) RMSF of Bcl-xL from MD simulations plotted as B-factors. The residues are colored from less flexible (blue) to more flexible (red); b) Representative ensemble of 40 protein conformers extracted from MD simulations by clustering.

17 Å radius around the OH group of Tyr91. GoldScore scoring function was used, while all other parameters had default values, to generate 200 docking conformations for each ligand.

Focused ligand libraries were built using the Sigma-Aldrich subset of ZINC database[12] (18 579 compounds) and an in-house developed script based on CACT-VS Scripting Toolkit.[13] Library A, targeting the South region of the Bcl-xL binding groove, contained 3 354 ester derivatives, whereas Libraries B and C, which target the North region, contained 1 672 and 1 796 compounds obtained from aldehydes and ketones, respectively.

Results

The recent identification of the natural product meiogynine A as an antagonist of the interaction between the proteins Bcl-xL and Bak makes this compound an appealing starting structure for the development of more potent inhibitors, with applications in anticancer therapy. However, the mode of interaction between meiogynine A and Bcl-xL is presently unknown. In this study, we have identified the molecular determinants governing this interaction, using molecular dynamics and flexible docking calculations. This information has been subsequently used to design new meiogynine A derivatives using focused ligand libraries.

The conformational flexibility of Bcl-xL has been explored using molecular dynamics, starting from four representative X-ray structures. The root mean square fluctuation (RMSF) has been calculated from these simulations for all residues and plotted as B-factors (Figure 2a). It appears that, starting from different conformations, the protein flexibility is observed in different regions. However, in all cases Arg100 is found as the most flexible residue. The other arginine residues are less flexible, being generally involved in interactions with neighbouring amino acids. These MD simulations were used to improve the sampling of the protein conformational space and to generate by clustering a representative ensemble of 40 conformers of Bcl-xL (Figure 2b).

These ensembles of conformers were further used for flexible molecular docking of meiogynine A and its diastereoismers[3] on Bcl-xL. In this way, binding conformations are obtained for the most active compounds, meiogynine A, 1"-*epi*-meiogynine A and enantio-meiogynine A, whereas the fourth compound, 1»-*epi*-enantio-meiogynine A,
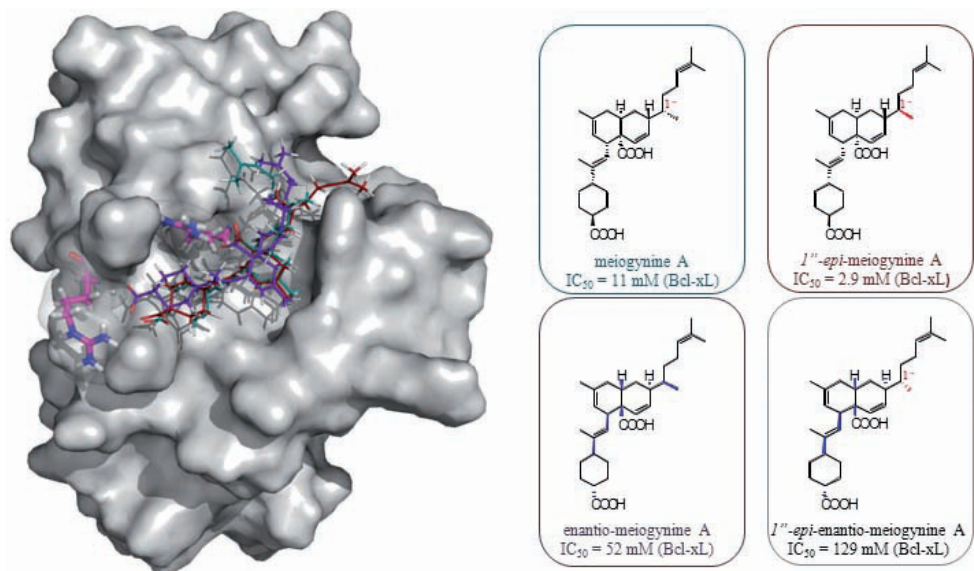
Figure 3: Binding modes of meiogynine A and its diastereoisomers on Bcl-xL, as predicted by docking (left); molecular structures and biological activities of ligands3 (right).

less active, is unable to bind into the groove. Furthermore, this step led to the identification of only one protein conformation for which docking results are in agreement with the biological data. In addition to hydrophobic contacts stabilizing the protein-ligand interface, key electrostatic interactions were observed between the two carboxyl groups of the ligand and the side chains of Arg132 and Arg139 (Figure 3).

We used the binding conformation of the most potent derivative in this series, 1"-*epi*-meiogynine A, for the design of three focused ligand libraries targeting the North and South regions of binding groove. These libraries are generated *in silico* using commercially available reagents and user-defined reactions, according to a methodology developed in our laboratory: i) Library A, targeting the South region, was generated by the esterification of commercially available carboxylic acids with an alcohol derived from 1"-*epi*-meiogynine A; ii) Libraries B and C, targeting the North region, were generated using the Wittig reaction between an ylide derived from 1»-*epi*-meiogynine A and commercially available aldehydes and ketones, respectively (Figure 4). These three focused libraries were used for virtual screening on the Bcl-xL conformation identified above and the results are currently being analyzed in order to identify meiogynine A derivatives with improved biological activity.

Conclusions

We present here the identification of molecular determinants for the interaction between Bcl-xL and meiogynine A and its diastereoisomers, using molecular modelling techniques. These results are in good agreement with the available experimental data. Additionally, three focused ligand libraries, targeting the North and South regions of
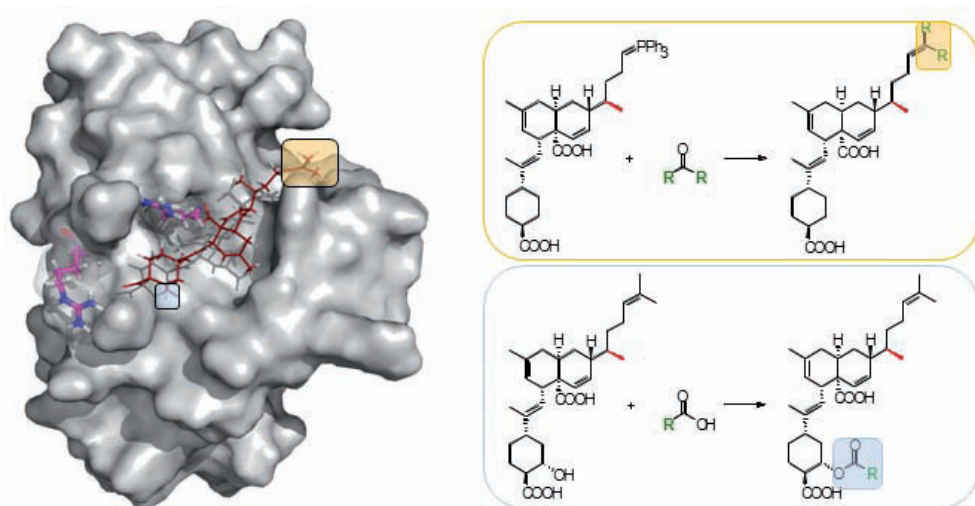
Figure 4: Positions on the structure of 1"-epi-meiogynine A used for the design of focused ligand libraries targeting the North and South regions of Bcl-xL binding groove (left); chemical reactions used for in silico building of these libraries (right).

the binding groove, were generated *in silico* using the 1"-*epi*-meiogynine A as core structure. These libraries were further used for virtual screening with Bcl-xL and the analysis of the results, which is currently ongoing in our laboratory, will allow the selection of meiogynine A derivatives with improved biological activity and extended protein-ligand surface contact.

Acknowledgements

References

1. Petros, A. M., Olejniczak, E. T., Fesik, S. W. Structural biology of the Bcl-2 family of proteins. *Biochim. Biophys. Acta* **1644**, 83-94 (2004).

2. Litaudon, M., Bousserouel, H., Awang, K., Nosjean, O., Martin, M. T., Dau, M. E., Hadi, H. A., Boutin, J. A., Sevenet, T., Gueritte, F. A Dimeric sesquiterpenoid from a Malaysian Meiogyne as a new inhibitor of Bcl-xL/BakBH3 domain peptide interaction. *J. Nat. Prod.* **72**, 480-483 (2009).

3. Fotsop, D. F., Roussi, F., Leverrier, A., Breteche, A., Gueritte, F. Biomimetic total synthesis of meiogynin A, an inhibitor of Bcl-xL and Bak interaction. *J. Org. Chem.* **75**, 7412-7415 (2010).

4. Gross, A., McDonnell, J. M., Korsmeyer, S. J. Bcl-2 family members and the mitochondria in apoptosis. *Genes and Dev.* **13**, 1899-1911 (1999).

5. Lee, E. F., Sadowsky, J. D., Smith, B. J., Czabotar, P. E., Peterson-Kaufman, K. J., Colman, P. M., Gellman, S. H., Fairlie, W. D. High-resolution structural characterization of

a helical alpha/beta-peptide foldamer bound to the anti-apoptotic protein Bcl-xL. *Angew. Chem. Int. Ed. Engl.* **48**, 4318-4322 (2009).

6. Willis, S. N., Chen, L., Dewson, G., Wei, A., Naik, E., Fletcher, J. I., Adams, J. M., Huang, D. C. Proapoptotic Bak is sequestered by Mcl-1 and Bcl-xL, but not Bcl-2, until displaced by BH3-only proteins. *Genes and Dev.* **19**, 1294 (2005).

7. Hess, B., Kutzner, C., van der Spoel, D., Lindahl, E. GROMACS 4: Algorithms for highly efficient, load-balanced, and scalable molecular simulation. *J. Chem. Theory Comput.* **4**, 435-447 (2008).

8. Kaminski, G. A., Friesner, R. A., Tirado-Rives, J., and Jorgensen,W. L. Evaluation and reparametrization of the OPLS-AA force field for proteins via comparison with accurate quantum chemical calculations on peptides. *J. Phys. Chem. B* **105**, 6474-6487 (2001).

9. The PyMOL Molecular Graphics System, Version 0.99, Schrödinger, LLC.

10. Corina, version 3.44 (http://www.molecular-networks.com/products/corina/).

11. Verdonk, M. L., Cole, J. C., Hartshorn, M. J., Murray, C. W., Taylor, R. D. Improved protein-ligand docking using GOLD. *Proteins* **52**, 609-623 (2003).

12. Irwin, J. J., Shoichet, B. K. ZINC - a free database of commercially available compounds for virtual screening. *J. Chem. Inf. Model.* **45**, 177-182 (2005).

13. CACTVS Scripting Toolkit, version 3.384, Xemistry Chemoinformatics (http://www.xe-mistry.com/).

Stereochemistry of nucleophilic HCN addition to C-glycosyl-imines

Sipos S., Jablonkai I.

Department of Carbohydrate Chemistry, Institute of Biomolecular Chemistry, Hungarian Academy of Sciences, Chemical Research Center, Pusztaszeri ut 59-67, Budapest, Hungary

Design and synthesis of glycoconjugate mimetics opened new frontiers for the research and development of new pharmaceuticals. Membrane transport, *in vivo* half life, and tissue-specific binding of the parent peptide sensitive to chemical and enzymatical hydrolysis were increased by conjugation to carbohydrates.[1] Since natural *N*- and *O*-glyco-amino acids are sensitive to hydrolysis extensive research has been conducted for the preparation of *C*-glycoaminoacids. Therefore our objectives were a) to prepare 2-amino-2-*C*-(α/β-D-glycopyranosyl) acetonitriles as *C*-glycosyl glycine precursors from α- and β-anomeric *C*-glycosyl aldehydes in Strecker reactions (Figure 1), and b) to study the stereochemistry of the hydrocyanation reaction of *C*-glycosyl-methyleneimines.

Strecker-reaction for the preparation of *C*-glyco-aminonitriles (**4**) were carried out with 1-*C*-formyl-glycals (**1**), 2-deoxy-glycosyl- (**2**), and glycosyl formaldehydes (**3**) using chiral ((*S* and *R*)-1-phenylethylamines (*S*- or *R*-PEA)) or achiral benzylamine (BA) and various cyanide donors such as NaCN, acetone cyanohydrine (ACH), or TMSCN. In case of chromatographically inseparable diastereomeric mixtures of aminonitriles **4** diastereomeric ratios (dr) were calculated from the ^{1}H NMR integral values of the CH protons at the new stereogenic center (C-7 as indicated on the numbered structure of **4** on Figure 1). Strecker reaction with protected 1-*C*-formyl-D-galactal and glucal derivatives (**1**) resulted in the respective aminonitriles in 78% and 38% yields with 3.0 and 1.5 dr values, respectively. The reaction exhibited higher stereoselectivity when *S*-PEA was used as compared to *R*-PEA indicating that in the imine intermediate formed with the *S*-configured amine the *Re* diastereotopic face at the prochiral CH=N group was preferred. The Strecker reactions carried out with 2-deoxy-β-D-glycosyl aldehydes (**2**) and *S*-PEA employing TMSCN in CH_2Cl_2 or ACH in THF exhibited higher dr values (8.25 and 5.17, respectively). However, low yields (30-50%) and diastereoselectivities (1.3-3.3) were obtained when the reaction was carried out with α- and β-linked *C*-glycosyl aldehydes (**3**) derived from glucose, galactose and mannose. The low yields can be attributed to the decomposition of these unstable aldehydes by 2-alkyloxy elimination.[2] Higher dr values were obtained with β-linked aldehydes as compared to those from the α-linked derivatives using *S*-PEA.
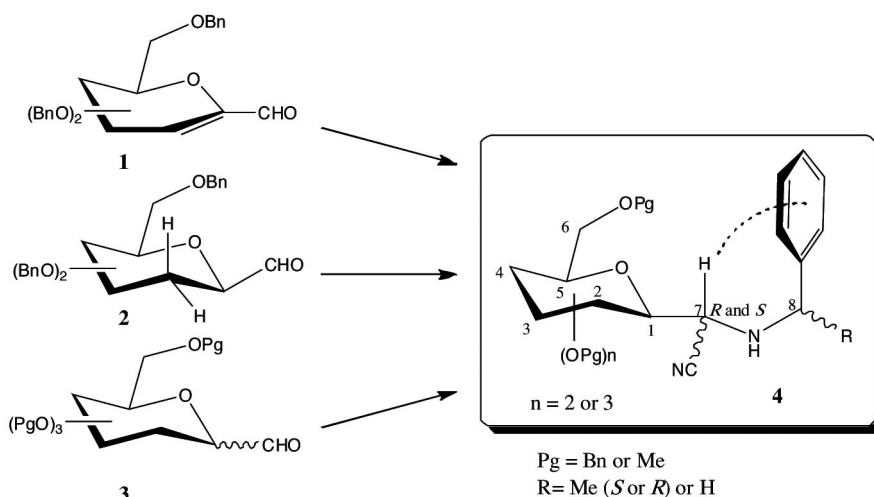
Figure 1. Synthesis of 2-amino-2-C-(α/β-D-glycopyranosyl) acetonitriles by Strecker reaction.
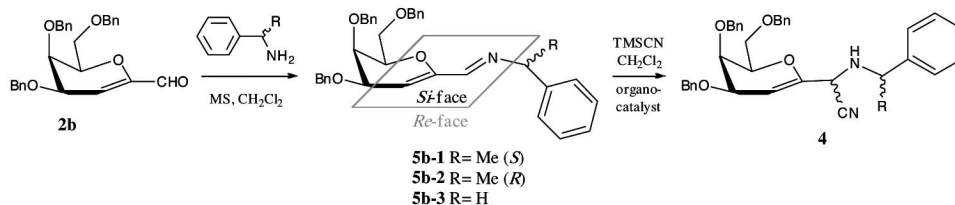
Figure 2. Preparation of D-galactal-linked α-aminonitriles via galactal imines

The assignment of the configuration at the newly formed stereocenter was a crucial problem in our work. While diastereomers of benzyl-protected glycal- and 2-deoxy-glycosyl-linked aminonitriles were inseparable, isolated diastereomers of benzyl-protected *C*-glycosyl-acetonitriles were oily materials unsuitable for an X-ray crystallographic structure determination. However, the absolute configuration of the new stereocenter in the crystalline major product of derived from permethyl α-mannopyranosyl aldehyde was established *R* by X-ray crystallography. In this diastereomer the methine proton (H-7) is located above the benzene ring (Figure 1). For all other compounds, the configurations of the major and minor diastereomeric products were determined by comparing the ^{1}H NMR chemical shifts of methine protons (H-7) at the new stereocenter as described in the literature.[3] In the aminonitriles formed from achiral aldehydes, the signals due to the methine protons of the new stereocenter in the major isomers always appeared at a higher field than those in the minor isomers. The observed upfield methine shift is due to the magnetic shielding effect by the phenyl group from the chiral amine in the major diastereomers. In case

Substrate	Amine (1 eq)	HCN donor (1.25 eq)	Catalyst (0.02 eq)	Product C-7 config.	Yield (%)	dr
2b	*S*-PEA	TMSCN	-	*R*	65	5.82
5b-1	-	TMSCN	**Jacobsen**	*R*	78	4.80
2b	*R*-PEA	TMSCN	-	*R*	61	2.44
5b-2	-	TMSCN	**Jacobsen**	*R*	77	2.11
2b	BA	TMSCN	-	*R*[b]	72	3.36
5b-3	-	TMSCN	**cinchona**[a]	*R*[b]	77	2.85

[a] 0.10 equiv. of catalyst was used. [b] Suggested configuration based on preferred *Re*-face attack by ⁻CN.

Table 1. Diastereoselectivity of Strecker reaction depending on the chirality of the amine and the effect of thiourea organocatalysts in the hydrocyanation of preformed imines

of aminonitriles prepared from *C*-glycosyl aldehydes similar pattern was established using *S*-PEA chiral auxiliary. Consistent differences in the range of 0.2–0.4 ppm were noticed. In asymmetric Strecker reaction with *S*-PEA and achiral aliphatic or substituted benzaldehydes *re*-face selectivity was observed.[3] With glycosyl aldehydes *Re*-face addition of the cyano group to the prochiral center yielded *R*-configured major products since the Cahn-Ingold-Prelog priority of C-1 (anomeric carbon) is higher than that of CN (Figure 2). In the reaction of **2b** with chiral amines and TMSCN predominantly *R*-configured products were obtained. Higher dr value was achieved with *S*-PEA (dr 5.82) than with *R*-PEA (dr 2.44) (Table 1) indicating that in the Strecker reaction **2b** and S-PEA react as a matched pair. It is noteworthy that employing TMSCN as cyanide donor resulted in higher diastereoselectivities as compared to reactions carried out with ACH. With achiral benzylamine 3.66 of dr was observed. Our results indicate that the asymmetric induction by the reacting sugar is dominant over the 1,3-asymmetric induction by the *R*-PEA. Diastereoselectivity of the reaction from preformed imines (**5**) prepared from galactal aldehyde was not influenced by the use of thiourea organocatalysts.[4]

In summary, synthesis and structure elucidation of new 2-amino-2-*C*-D-glycosyl-acetonitriles in a Strecker reaction from various *C*-glycosyl aldehydes, chiral amines and HCN was carried out. While aminonitriles from glycal and 2-deoxy-β-glycosyl aldehydes were prepared in satisfactory yields, lower yields were obtained with *C*-glycosyl aldehydes due to the decomposition of these aldehydes by β-elimination. The configurations of the major and minor diastereomeric products were assigned based on the ¹H NMR chemical shifts of methine protons at the new stereocenter. Strecker reaction with the benzyl-protected 1-*C*-formyl-D-galactal and *S*-PEA or *R*-PEA yielded predominantly the *R*-configured *C*-glyco-aminonitrile via *Re*-face nucleophilic addition of HCN in both cases. Since higher dr values were obtained with *S*-PEA as compared to *R*-PEA, we can conclude that the aminonitrile formation from the 1-*C*-formyl-D-galactal derivative, *S*-PEA and TMSCN takes place in a matched pair reaction. The direction of the nucleophilic addition appears to be governed by the configuration of the anomeric carbon with β-linked sugars. In order to improve stereoselectivity of the Strecker reaction the complex-forming ability of carbohydrates can be exploited.

Coordination of Lewis acids to glycosyl imines formed from glycosyl amines has been found to have strong influence on the stereodifferentiation in the nucleophilic cyanide addition.[5]

References

1. POLKOWSKI, K. et al., Cytostatic and cytotoxic activity of synthetic genistein glycosides against human cancer cell lines. Cancer Letters, 203, 59-69, 2004.
2. SOMSAK, L., Carbanionic reactivity of the anomeric center in carbohydrates. Chem. Rev., 101, 81-135, 2001**.**
3. INABA, T. et al., Thermodinamically controlled 1,3-asymmetric induction in an acyclic system: Equilibration of α-amino nitriles derived from α-alkylbenzylamines and aldehydes. J. Org. Chem., 56, 1274-1279, 1991.
4. SIPOS, S. and JABLONKAI. I., One-pot synthesis of □-aminonitriles from alkyl and aryl cyanides: a Strecker reaction via aldimine alanes. Tetrahedron Letters, 50, 1844-1846, 2009.
5. TIETGEN, H. et al., Glycosylamines as auxiliaries in stereoselective synthesis of chiral amino compounds. In *Modern Amination Methods*, Ricci, A., Ed, Wiley-VCH: Weinheim, 2000, pp 103-128.

Efficient Water Splitting by Single Site Ruthenium Catalyst

Joya, K.S.[*1,2] **and de Groot, H.J.M.**[1*]

[1]*SSNMR, Leiden Institute of Chemistry, Leiden University, 2300 RA, Leiden, The Netherlands,*
[2]*Department of Chemistry, University of Engineering and Technology, GT-Road, 54890, Lahore, Pakistan.*
e-mail: ssnmr@chem.leidenuniv.nl

Summary: To develop a water splitting system operating at high efficiency and rate is challenging. We recently found a class of mononuclear artificial water oxidation complexes (WOC) that show a consecutive four-step proton coupled electron transfer (PCET) mechanism for oxygen generation. Surface anchored electrocatalytic assemblies generate > 250,000 turnover number at rapid rates up to 80 per sec with a moderate overpotential at high current densities.

Introduction: There is a growing concern for affordable and efficient catalytic materials for solar driven water splitting to generate oxygen and hydrogen with high efficiency [1]. In spite of many attempts, developing an artificial equivalent of the Mn_4CaO_x cluster in photosystem-II that is capable of oxidizing water with a high rate for hundred thousands of cycles is a challenging hurdle in this pursuit [2]. A four-step PCET pathway is beneficial to produce four redox couples that avoid high energy intermediates during a multi-electron water oxidation cycle [3]. We here describe a mono-site electrocatalytic water oxidation assembly based on a bidentate nitrogen ligand (N-N) derived Ru-complex with an aromatic (Ar) non-bonding ligand (Fig. 1) that operates at moderate overpotential with high activity for oxygen generation along a consecutive four-step PCET reaction coordinate [4].

Materials and Methods: Ligands and complexes were synthesized in argon atmosphere. Solutions were prepared in deoxygenated Millipore (MilliQ®) water and all measurements were taken at room temperature. Catalyst was anchored on ITO coated glass slides (1 cm^2) and electrolysis was conducted in a three electrode H-type glass cell using Pt-wire as counter electrode. Reference electrode was SSCE. An Autolab PG-stat10 potentiostat was used and oxygen was measured with YSI 550A electrode.

Results and Discussion: The chloro Ru complexes underwent rapid aqua conversion into $[(Ar)Ru^{II}(N-N)-OH_2]^{2+}$ catalysts accompanied by spectral changes [4]. Complexes display pH dependent oxidation involving $[Ru^{III}-(OH)]^{2+}/[Ru^{II}-(OH_2)]^{2+}$, $[Ru^{IV}(=O)]^{2+}/$
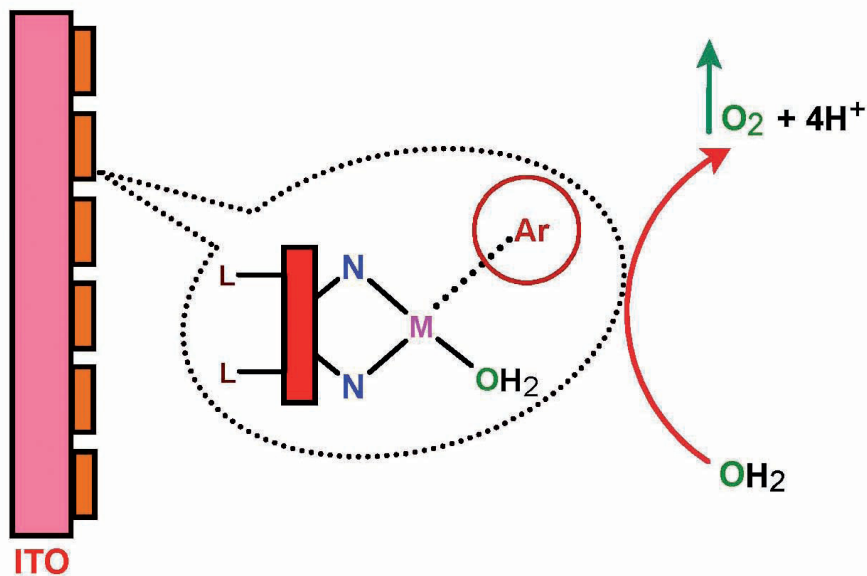
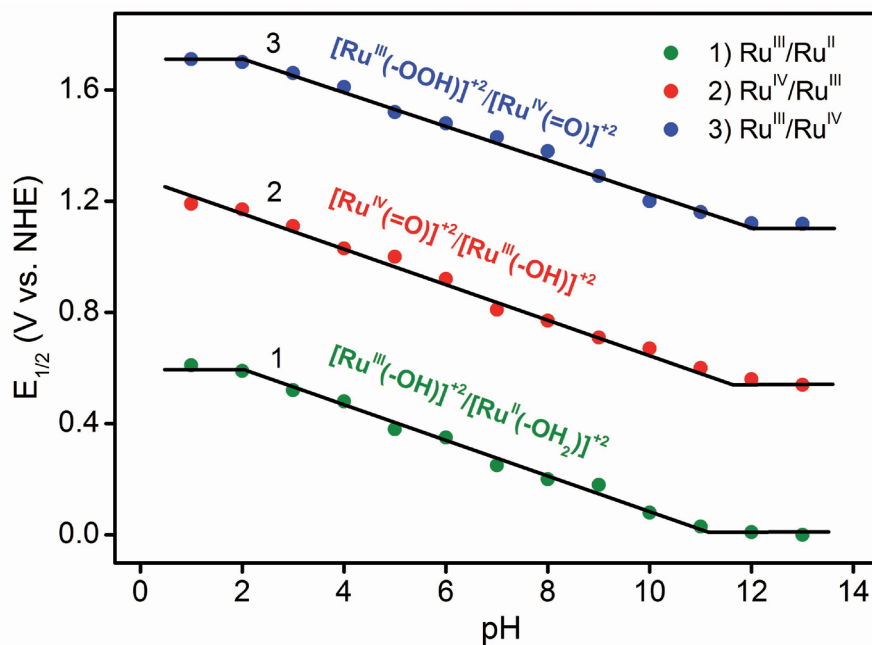Fig.1. Catalytic water oxidation assembly.

Fig.2. Potential vs pH plot for various ruthenium couples.
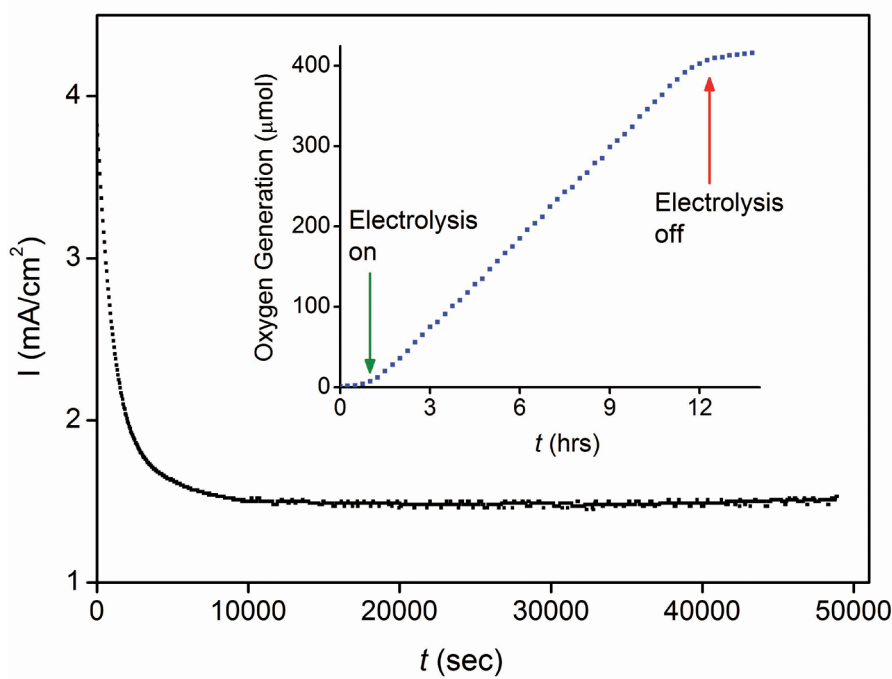
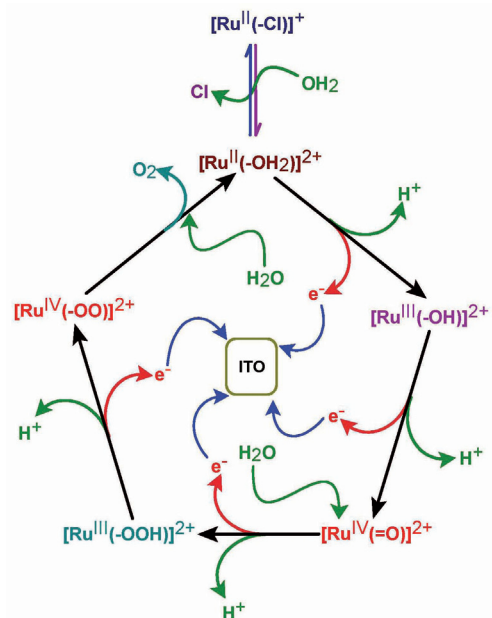*Fig.3. Controlled-potential catalytic water oxidation and oxygen evolution.*

Fig.4. A pentacyclic mechanism for catalytic water oxidation and O2 evolution.

$[Ru^{III}\text{-}(OH)]^{2+}$ and $Ru^{III}\text{-}(OOH)]^{2+}/[Ru^{IV}(=O)]^{2+}$ redox couples, thus avoiding the formation of a high energy $[Ru^V(=O)]^{3+}$ intermediate. The Pourbaix diagram reveals a ~60 mV/pH shift from 2 to 12 pH range (Fig. 2). Catalyst-ITO in neutral solution generated more than 400 μmol of oxygen in 11 hours in a controlled-potential water electrolysis setup at a relatively low overpotential with a current density >1.5 mA/cm^2. The catalyst turnovers were more than 3.1×10^5 in 12 hours at a turnover rate of ~7.14 moles of O_2 per sec (Fig. 3). A pentacyclic mechanism deduced from the electrochemical analysis shows that a double positive charge is maintained throughout the water oxidation cycle. The oxidative transitions $[Ru^{III}\text{-}(OH)]^{2+}/[Ru^{II}\text{-}(OH_2)]^{2+}$ and $[Ru^{IV}(=O)]^{2+}/[Ru^{III}\text{-}(OH)]^{2+}$ are realized by two successive PCET steps in the first half of the water oxidation cycle. The $[Ru^{IV}(=O)]^{2+}$ intermediate, on second aqua insertion, also undergoes a pH dependant transformation into $[Ru^{III}\text{-}(OOH)]^{2+}/[Ru^{IV}(=O)]^{2+}$ and higher potential species before oxygen onset (Fig. 4).

Conclusions: We have developed a group of mononuclear water splitting catalysts and disclose a novel four-step PCET mechanism. Our system manifests the highest turnover numbers and a turnover rate up to 80 was realized during full cell water electrolysis between 1.8–2.4 V. Our results thus open new doors towards efficient, stable and easy accessible water splitting catalytic system for clean fuel generation.

References:

[1] Lewis, N.S. Light work with water. *Nature* 414, 589–590 (2001);

[2] Dau, H., et al. The mechanism of water oxidation: from electrolysis via homogeneous to biological catalysis. *ChemCatChem.* 2, 724–761 (2010);

[3] Huynh, M.H.V., et al. Proton-coupled electron transfer. *Chem. Rev.* 107, 5004–5064 (2007);

[4] Joya, K.S., et al. Metal complex and use as multi-electron catalyst, *Patent Application* no. 2005512, Oct., 2010.

Synthesis of catechin derivative with basic amino acid as a promising antioxidant

Imai K.[1,2], Nakanishi I.[3,4], Nakanishi S.[1], Takagaki R.[1], Matsumoto K.[3], Anzai K.[3,5], Ozawa T.[3,6], Okuda H.[1], Nakamura A.[2], Fukuhara K.[1]

[1] *Division of Organic Chemistry, National Institute of Health Sciences, Setagaya-ku, Tokyo 158-8501, Japan.*
[2] *Department of Applied Chemistry, Shibaura Institute of Technology, 307 Fukasaku, Minuma-ku, Saitama-shi, Saitama 337-8570, Japan*
[3] *Research Center for Charged Particle Therapy, National Institute c of Radiological Sciences, Inage-ku, Chiba 263-8555, Japan*
[4] *Graduate School of Engineering, Osaka University, SORST, Japan Science and Technology Agency, Suita, Osaka 565-0871, Japan*
[5] *Nihon Pharmaceutical University, Ina-cho Kita-adachi-gun, Saitama, 362-0806, Japan*
[6] *Yokohama College of Pharmacy, Tozuka-ku, Yokohama, Kanagama, 245-0066, Japan*

Summary

Planar catechin derivatives with amino acids were synthesized to increase radical scavenging activity of catechin. Among them, lysine and arginine derivatives were showed 400-fold increased radical scavenging activity relative to naturally occurring (+)-catechin.

Introduction

The prevention of natural polyphenols toward coronary diseases, brain dysfunction and cancer is due to their antioxidative properties to inhibit oxidative stress contributing to the incidence of such pathologies. Previouly, we have synthesized planar catechin analogue by which catechol (B ring) and chroman moieties (AC rings) in (+)-catechin structure are constrained to be planar. The planar catechin showed 5-fold radical scavenging activity compared with that of (+)-catechin.[1,2] (**Scheme. 1**)

The radical-scavenging activity of planar catechin is enhanced by way of introduction of electron donating isopropyl moiety that results in the stabilization of radical cation. In addition, it is known that not only catechin but also antioxidant agents have ability of enhanced radical-scavenging activity under basic condition. The radical-scavenging reaction of a vitamin E model is significantly accelerated by the presence of a base, such as pyridine.[4] As vitamin E is oxidized to form the corresponding radical cation by a radical scavenging reaction, the acceleration is attributed to the stabilization of
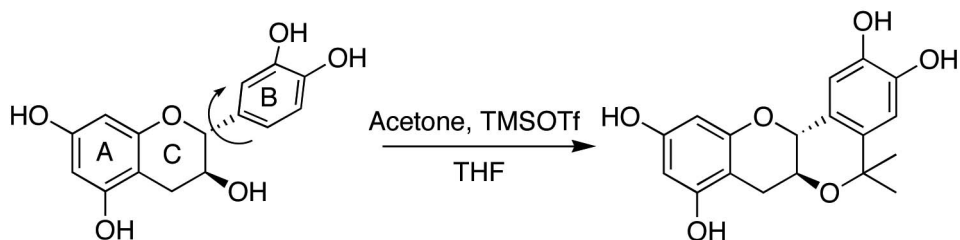
Scheme.1. Synthesis of Planar Catechin
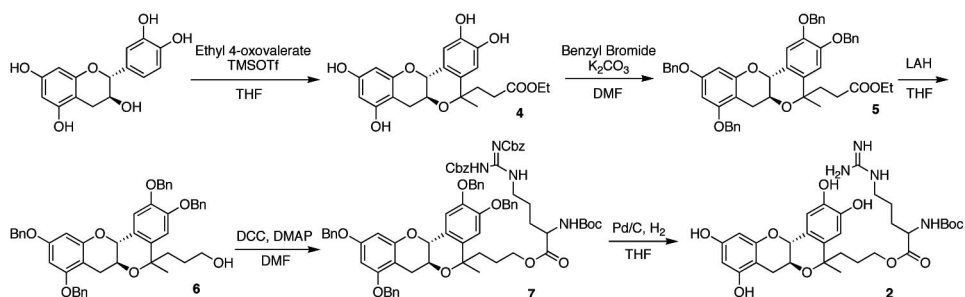
Scheme. 2. Synthesis of Planar Catechin Derivative with Lysine

the radical cation by base. However, it is very difficult to make basic condition in vivo. Our idea is, if a basic functional group were introduced into planar catechin, the radical-scavenging activities of planar catechin would be increased even in neutral conditions without addition of base, thereby leading to the development of a super antioxidant effective for the prevention and treatment of oxidative stress-related diseases. [5] In this study, planar catechin derivatives with lysine **1**, arginine **2** and histidine **3** were synthesized and their radical scavenging activities were determined.

Methods and Result

We designed and synthesized planar catechin derivatives with basic amino acids of lysine, arginine or histidine. These compounds were synthesized as shown **scheme.2**. B ring and AC rings in catechin structure are constrained to be planar with 4-oxova-leric acid ethyl ester **4**. After protection of phenolic OH with benbyl bromide **5**, the ethyl ester was reduced with LAH to afford the alcohol derivative **6**, which is then reacted with N^a-Boc-N^e-Z lysine, N^a-Boc-N^e-Z arginine or N^a-Boc-N^e-benzyl histidine using DCC, followed by deprotection with hydrogenation (Pd/C, H$_2$) to furnish planar catechin derivative with amino acid.

The radical scavenging activities of these compounds were compared using the galvinoxyl radical as an oxyl radical species, showing the stronger radical scavenging activities than (+)-catechin and planar catechin derivative without amino acid. The experiment is performed using stopped flow technique in acetonitrile. We determined that ability of radical scavenging (k_{HT}) for hydrogen abstraction of catechin by GO•
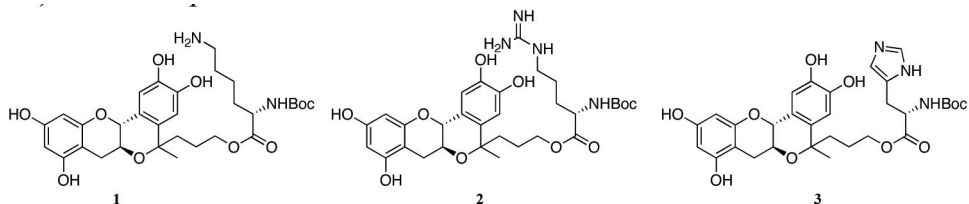
Figure. 1. Planar Catechin Derivative with Basic Amino Acid

Plot of the pseudo-first-order rate constants (K_{obs}) vs [Catechin] for the reaction of Planar Catechin-His Deriv. or Catechin and Planar Catechin-Lys Deriv. with GO·(6.9×10^{-6}M) in deaerated MeCN at 298K
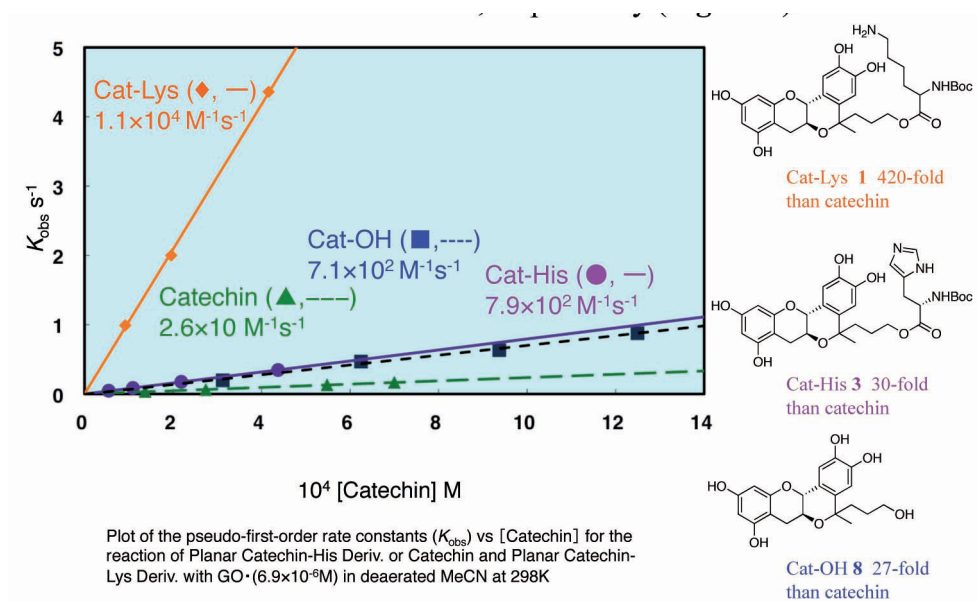
Figure. 2. Enhanced Radical Scavenging Activity of Catechin Derivative with Amino Acid

was 2.6×10 M^{-1}s^{-1}. The k_{HT} values for **1**, **3** and planar catechin derivative without amino acid **8** were determined in the same manner to be 1.1×10^4 M^{-1}s^{-1}, 7.9×10^2 M^{-1}s^{-1} and 7.1×10^2 M^{-1}s^{-1}, respectively (**Figure.2**)

The k_{HT} value for **2** was not determined in the same manner, because **2** did not solve in acetonitrile. So radical scavenging activity was performed in ethanol. Showing that k_{HT} values for **1**, **2** were 3.6×10^4 M^{-1}s^{-1}, 1.0×10^5 M^{-1}s^{-1}, respectively (**Figure. 3**).

Conclusions

A planar catechin derivative incorporating the basic amino acid was synthesized. Among them, arginine derivative was shown the most strongest antioxidant in the our knowledge.

Plot of the pseudo-first-order rate constants (K_{obs}) vs [Catechin] for the reaction of Planar Catechin-Arg Deriv. or Catechin and Planar Catechin-Lys Deriv. with GO · (5.1×10^{-6} M) in deaerated EtOH at 298K
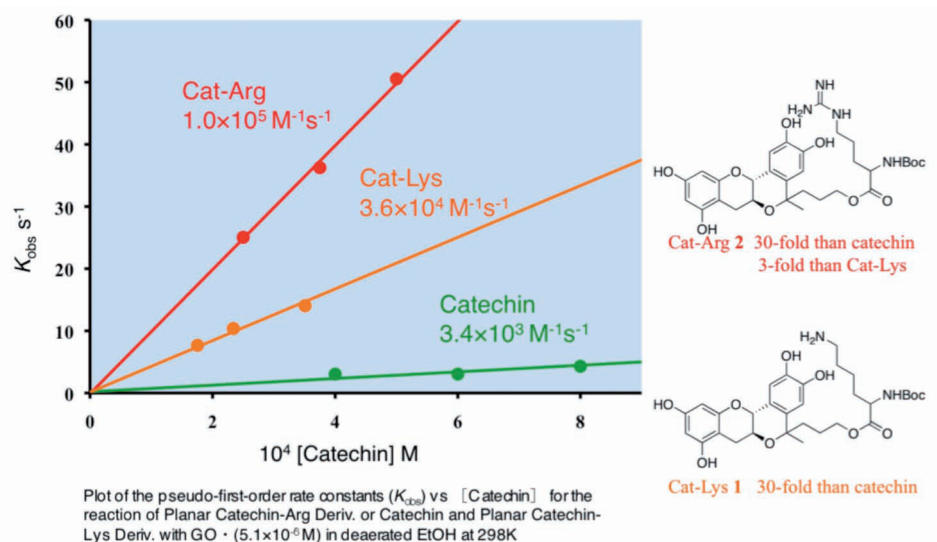
Figure. 3. Enhanced Radical Scavenging Activity of Catechin Derivative with Arginine

References:

[1] K. Fukuhara, I. Nakanishi, H. Kansui, E. Sugiyama, M. Kimura, T. Shimada, S. Urano, K. Yamaguchi and N. Miyata, Enhance Radical-Scavenging Activity of a Planar Catechin Anagogue *J. Am. Chem. Soc.,* **124**, 5952–5953, (2002).

[2] W. Hakamata, I. Nakanishi, Y. Masuda, T. Shimizu, H. Higuchi, Y. Nakamura, S. Saito, S. Urano, T. Oku, T. Ozawa, N. Ikota, N. Miyata, H. Okuda and K. Fukuhara, Planar Catechin Analogue with Alkyl Side Chains; A Potent Antioxidant and an α-Glucosidase Inhibitor, *J. Am. Chem. Soc*., **128**, 6524–6525, (2006).

[3] I.Nakanishi,T.Kawashima,K.Ohkubo,H.Kanazawa,K.Inami, M. Mochizuki, K. Fukuhara, H. Okuda, T. Ozawa, S. Itoh, S. Fukuzumi and N. Ikota, Electron-Transfer Mechanism in Radical-Scavnging Reaction by a Vitamin E Model in a Protic Medium, *Org. Biomol. Chem*., **3**, 626–629, (2005).

[4] K. Fukuhara, I. Nakanishi, K. Ohkubo, Y. Obara, A. Tada, K. Imai, A. Ohno, A. Nakamura, T. Ozawa, S. Urano, S. Saito, S. Fukuzumi, K. Aznai, N. Miyata, and H. Okuda, Intramolecular base-accelerated radical-scavenging reaction of a planar catechin derivative bearing a lysine moiety, *Chem. Commun.,* **41**, 6180-6182, (2009).

Characteristic conformational patterns of the Trp- and Arg-rich antimicrobial peptides

Leitgeb B.

Institute of Biophysics, Biological Research Centre, Hungarian Academy of Sciences, Szeged, Hungary

Summary

In this study, molecular dynamics simulations were performed on certain stereoisomeric forms of indolicidin and tritrpticin, in order to identify their characteristic conformational patterns. Based on the results, it could be concluded that the stereoisomers of both Trp- and Arg-rich antimicrobial peptides showed typical patterns with regard to their secondary structural elements, as well as to their intramolecular interactions.

Introduction

Indolicidin and tritrpticin are antimicrobial tridecapeptides, which possess remarkable primary structure with a high content of aromatic (*i.e.* Trp and Phe) and basic (*i.e.* Arg and Lys) residues, as well as of Pro amino acids (see Table 1). The former antimicrobial peptide (AMP) was isolated from the cytoplasmic granules of bovine neutrophils [1], while the latter one was identified in the porcine bone marrow [2]. Both of them show a broad spectrum of antimicrobial activity against Gram(+) and Gram(-) bacteria, as well as fungi, however, they exhibit also hemolytic effect.

Indolicidin and tritrpticin contain three and two Pro amino acids, respectively, and according to the *cis-trans* isomerism about the Xaa-Pro peptide bonds, various stereoisomeric forms could be distinguished for these AMPs. In this theoretical study, molecular dynamics calculations were carried out on certain stereoisomers of both Trp- and Arg-rich AMPs, in order to investigate their characteristic conformational patterns, as well as to examine the effects of *cis-trans* isomerism on the structural features of indolicidin and tritrpticin.

Methods

The molecular dynamics (MD) calculations were performed with the AMBER 9

Indolicidin:

H-Ile-Leu-*Pro*-**Trp**-Lys-**Trp**-*Pro*-**Trp**-**Trp**-*Pro*-**Trp**-Arg-Arg-NH$_2$

Tritrpticin:

H-Val-Arg-Arg-**Phe**-*Pro*-**Trp**-**Trp**-**Trp**-*Pro*-**Phe**-Leu-Arg-Arg-OH

Table 1. Primary structures of indolicidin and tritrpticin, possessing a high content of aromatic (i.e. Trp and Phe) and basic (i.e. Arg and Lys) residues, as well as of Pro amino acids.

software [3]. For the MD simulations, the AMBER 99SB force field [4] and the Generalized Born implicit solvent model were used, as well as no cutoff was app-lied in the case of nonbonding interactions. For each peptide, ten independent MD calculations were carried out for 50 ns on 300 K, using the Langevin model for temperature regulation. The simulations were started from geometrically-optimized structures, and random initial velocities were applied for every single calculation. During the MD simulations, the trajectories were sampled in every 1 ps, resulted in 50 000 conformational states for each peptide.

Two different stereoisomeric forms of both Trp- and Arg-rich AMPs were modeled, respectively: *(1)* peptide containing *trans* Xaa-Pro peptide bonds; *(2)* peptide posses-sing *cis* Xaa-Pro peptide bonds. The two stereoisomers of indolicidin were labeled by three letter codes (*i.e. ttt* and *ccc*), as well as the two stereoisomers of tritrpticin were labeled by two letter codes (*i.e. tt* and *cc*), where the letters represented the certain isomer of three or two Xaa-Pro peptide bonds, and the „*t*" and „*c*" indicated the *trans* and *cis* isomers of Xaa-Pro peptide bond, respectively.

Results

On the basis of MD simulations, the appearance and alterations of various con-formational features were studied as a function of time, and they were compared to each other, taking into account the two stereoisomeric forms of indolicidin and tritrpticin, respectively. For the stereoisomers, the presence of different secondary structural elements (*i.e.* types I, III and VI β-turns; as well as 3$_{10}$- and poly-proline II helical structures [5,6]) was investigated. These results indicated that characteristic turn conformations could be identified regarding certain tetrapeptide units of the two stereoisomeric forms of both Trp- and Arg-rich AMPs, which are showed in Table 2. In the case of *ttt* and *tt* stereoisomers, types I and III β-turns were identified in te-trapeptide units containing Pro in the second position, while these types of β-turns also appeared in certain tetrapeptide segments of all four stereoisomeric forms, which possessed Pro in the first position. For the *ccc* and *cc* stereoisomers, types VIa1, VIa2 and VIb β-turns were observed in those tetrapeptide units, in which Pro was located in the third position.

Furthermore, the appearance of two types of intramolecular interactions (*i.e.* H-bonds and proline-aromatic interplays [7]) was examined, which played an important role in the determination and stabilization of above-mentioned secondary structural elements. The *i←i+3* H-bonds formed between the backbone NH donor and CO ac-ceptor groups contributed to the structural stability of types I and III β-turns, as well

Xaa^i-Pro^{i+1}-Xaa^{i+2}-Xaa^{i+3}	types I, III β-turns

ttt-Indolicidin:

Leu^2-Pro^3-Trp^4-Lys^5; Trp^6-Pro^7-Trp^8-Trp^9; Trp^9-Pro^{10}-Trp^{11}-Arg^{12};

tt-Tritrpticin:

Phe^4-Pro^5-Trp^6-Trp^7; Trp^8-Pro^9-Phe^{10}-Leu^{11};

Pro^i-Xaa^{i+1}-Xaa^{i+2}-Xaa^{i+3}	types I, III β-turns

ttt-Indolicidin and ccc-Indolicidin:

Pro^3-Trp^4-Lys^5-Trp^6; Pro^{10}-Trp^{11}-Arg^{12}-Arg^{13};

tt-Tritrpticin and cc-Tritrpticin:

Pro^5-Trp^6-Trp^7-Trp^8; Pro^9-Phe^{10}-Leu^{11}-Arg^{12};

Xaa^i-Xaa^{i+1}-Pro^{i+2}-Xaa^{i+3}	types VIa1, VIa2, VIb β-turns

ccc-Indolicidin:

Ile^1-Leu^2-Pro^3-Trp^4; Lys^5-Trp^6-Pro^7-Trp^8; Trp^8-Trp^9-Pro^{10}-Trp^{11};

cc-Tritrpticin:

Arg^3-Phe^4-Pro^5-Trp^6; Trp^7-Trp^8-Pro^9-Phe^{10};

Table 2. Characteristic turn conformations regarding certain tetrapeptide units for the two stereoisomeric forms of indolicidin and tritrpticin.

as of 3_{10}-helical conformations. The proline-aromatic interactions evolved between the neighboring proline and aromatic amino acids produced a stabilizing effect on the structure of type VI β-turns.

Conclusions

Based on the results obtained by the MD calculations, it could be concluded that the two stereoisomers of indolicidin and tritrpticin showed characteristic patterns regarding their secondary structural elements and intramolecular interactions. Moreover, this theoretical study led to the observation that conformational similarities and dissimilarities could be observed between the two stereoisomeric forms of both Trp- and Arg-rich AMPs, respectively, which proved to be dependent on the *cis-trans* isomerism about the Xaa-Pro peptide bonds.

Acknowledgement

References

[1] SELSTED, M. E.; NOVOTNY, M. J.; MORRIS, W. L.; TANG, Y.-Q.; SMITH, W.; CUL-

LOR, J. S. Indolicidin, a novel bactericidal tridecapeptide amide from neutrophils. J. Biol. Chem. 267, 4292-4295, 1992

[2] LAWYER, C.; PAI, S; WATABE, M.; BORGIA, P.; MASHIMO, T.; EAGLETON, L.; WATABE, K. Antimicrobial activity of a 13 amino acid tryptophan-rich peptide derived from a putative porcine precursor protein of a novel family of antibacterial peptides. FEBS Lett. 390, 95-98, 1996

[3] CASE, D. A.; et al. AMBER 9, University of California, San Francisco, 2006

[4] HORNAK, V.; ABEL, R.; OKUR, A.; STROCKBINE, B.; ROITBERG, A.; SIMMER-LING, C. Comparison of multiple Amber force fields and development of improved protein backbone parameters. Proteins 65, 712-725, 2006

[5] LEITGEB, B.; KERÉNYI, Á.; BOGÁR, F.; PARAGI, G.; PENKE, B.; RÁKHELY, G. Studying the structural properties of polyalanine and polyglutamine peptides. J. Mol. Model. 13, 1141-1150, 2007

[6] JANZSÓ, G.; RÁKHELY, G.; LEITGEB, B. Comprehensive structural characterization of the cyclic disulphide-bridged nonapeptides, Arg- and Lys-conopressins. J. Mol. Graph. Model. 27, 881-888, 2009

[7] LEITGEB, B.; TÓTH, G. Aromatic-aromatic and proline-aromatic interactions in endomorphin-1 and endomorphin-2. Eur. J. Med. Chem. 40, 674-686, 2005

Trehalose and Mannitol Improved Thermal Stability of Salmon Calcitonin in Both Aqueous Solution and Lyophilized Solid Form

Lee TH, Lin SY*, Lin HL, Huang YT, Wu TK and Lin CC.

Department of Biotechnology, Yuanpei University, Hsin Chu, Taiwan, ROC

Summary

The conformational stability and structural similarity of salmon calcitonin (sCT) in aqueous solution and in lyophilized solid form were examined. Two types of additives, sugars/polols and polymers, were selected as a stabilizer for maintain the conformational stability of sCT after incubation in 40ºC aqueous solution or lyophilization. The results of present study illustrate that both trehalose and mannitol would serve as optimal stabilizers for sCT in aqueous solution and in lyophilized formulation.

Introduction

Calcitonin (CT) is well known to participate in many diverse physiological functions of human body, thus it has been always chosen as a suitable model of protein drug for investigation [1]. In the development of protein drugs, the stability of protein is one of the important factors that are closely correlated to the efficacy of final products [2]. To maintain a stable structure of protein drug in different formulations during the development process, storage, transportation and patient administration, the stabilization of protein drugs will be challenged during formulation design [2-3]. Although several additives have been successfully applied in the manufacturing process to improve the stability and the shelf-life of protein drugs, the stabilization effect of such additives varies from types and amounts, and also the kinds of protein drugs being used [2-5].

Salmon calcitonin (sCT) is one of the most popular CTs, and possesses approximately 40-50 times activity than human CT to inhibit osteoclastic bone resorption [6], therefore it is always selected as a candidate of protein drug. In order to study the stability of native sCT in aqueous solution and lyophilized solid product, four sugars/polyols and three hydrophilic polymers were selected as a stabilizer to examine the conformational structure of sCT in both states. A unique and powerful microscopic Fourier transform infrared (FT-IR) spectroscopy using second-derivative spectral

analysis and a structural similarity approach was applied to quickly and accurately screen these additives for sCT formulation.

Materials and methods

Materials

Salmon calcitonin (sCT), four sugars/polyols [trehalose dihydrate, mannitol, sucrose and 2-hydroxypropyl-β-cyclodextrin (HP-βCD)], three hydrophilic polymers [dextran 40, heparin, and human serum albumin (HSA), and KBr crystal were used.

Stability studies of sCT after co-incubation with or without different additives in aqueous solution

One percentage (w/v) of sCT aqueous solution with or without different additives (0.5%, w/v) was respectively incubated in a $40^{\circ}C$ water bath for 35 hrs. At predetermined intervals, the solution incubated was sampled, dropped on the CaF_2 plate and quickly dried under a stream of dry N_2 gas, and the sCT film casted on the CaF_2 plate (CaF_2 method) was formed.

Stability studies of sCT after co-lyophilization with or without different additives

Each lyophilizing solution containing 1% (w/v) of sCT and 0.5% (w/v) of additive was freeze-dried under $-48^{\circ}C$ for 25 hrs. Lyophilization of additive-free sCT aqueous solution was also carried out. A trace amount of the lyophilized powder was smeared on a piece of KBr pellet (smeared method) for spectral analysis.

Transmission FT-IR microspectroscopic studies

The IR spectra of different sCT samples prepared by either CaF_2 or smeared method were directly determined by FT-IR microspectroscopy equipped with a MCT detector using a transmission technique [23, 33-35]. All the spectra were obtained at a 4 cm^{-1} resolution and at 100 scans. Second-derivative spectral analysis was applied to locate the position of the overlapping components in the amide I bands and assigned to different secondary structures [7-8].

Structural similarity

To compare the structural similarity between native sCT and lyophilized sCT samples with or without additive, the spectral correlation coefficient analysis between two second-derivative IR spectra was applied. According to the Prestrelski's equation, the spectral correlation coefficient (r) between two second-derivative IR spectra was calculated [9]. All the spectral comparisons were performed in the amide I region. Each spectrum was baseline-offset corrected and area-normalized. Comparison of identical spectra gives a value of 1.0. The more changes in conformation occurred, the greater difference between two spectra obtained, leading to a small r value.
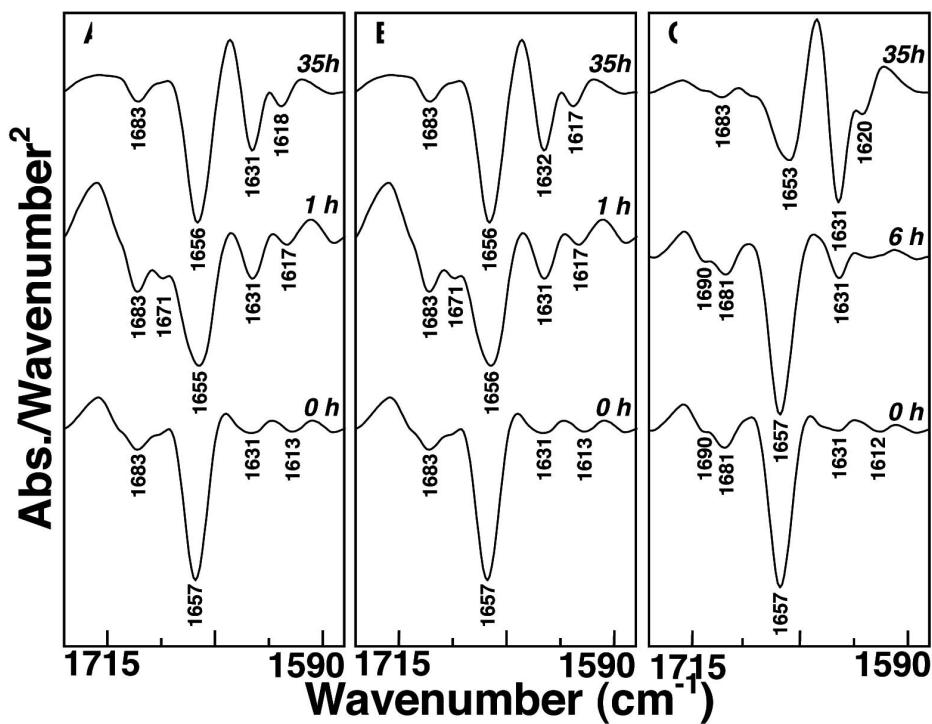
Fig. 1 Time-dependent structural changes in the second-derivative IR spectra of 1% sCT after co-mixing with each 0.5% additive after incubation at 40ºC. Additive: (A) trehalose, (B) mannitol, (C) HP-βCD.

Results and discussion

Additives affecting the conformational stability of sCT in aqueous solution after incubation at 40ºC

Once the sugars or polyols were added into each sCT aqueous solution and incubated at 40ºC with time, the representative time-dependent changes in the second-derivative IR spectra of sCT are indicated in Figs. 1. When the sCT aqueous solution was co-incubated with trehalose, two characteristic peaks at 1631 and 1671 cm^{-1} assigned to β-sheet structure appeared after incubation for 1 hr (Fig. 1A) [8-9]. With the increase of incubation time, the peak intensities at 1631 and 1618 cm^{-1} for sCT-trehalose sample were only slightly increased. The similar result was also found for sCT-mannitol sample (Fig. 1B). Although the stabilization effect of HP-βCD was found up to 6 hrs, beyond 6-hr the IR spectra of sCT were also gradually altered with the incubation time (Fig. 1C). After incubation for 35 hrs, the predominate peak at 1653 cm^{-1} (α-helix/random coil) was shifted from 1657 cm^{-1} (α-helix) and the peak intensity at 1631 cm^{-1} was more pronounced than that in Figs. 2A and 2B [7-9], suggesting that HP-βCD was not a good stabilizer for sCT. A similar tendency for the conformational change of sCT after co-incubation with sucrose was also observed.
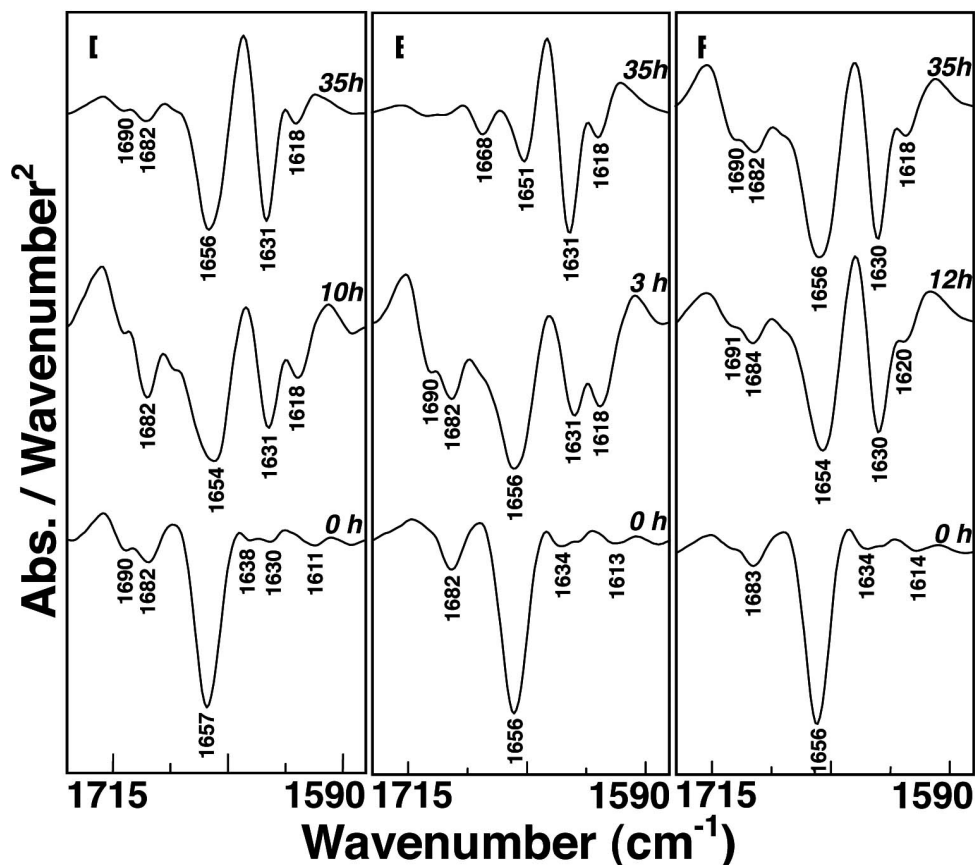
Fig. 2 Time-dependent structural changes in the second-derivative IR spectra of 1% sCT after co-mixing with each 0.5% additive after incubation at 40°C. Additive: (D) dextrin, (E) heparin, (F) HSA.

In this stability study, trehalose and mannitol seemed to less alter the conformation of sCT in aqueous solution after incubation at 40°C.

When dextran, heparin or HSA was added into each sCT aqueous solution, the different phenomena are observed in Fig. 2. At the initial incubation period (1-9 hrs), there was no marked change in the second-derivative IR spectrum for the sCT-dextran sample, as compared to the initial sample. Beyond incubation for 10 hrs, however, two characteristic peaks at 1631 and 1618 cm^{-1} assigned to β-sheet structure markedly appeared (Fig. 2D). Once heparin was added into the sCT aqueous solution, on the other hand, a turbid dispersion was immediately produced from the sCT-heparin aqueous solution. The second-derivative IR spectrum for the precipitate of sCT-heparin sample is shown in Fig. 2E. The turbid or precipitation formation in sCT-heparin aqueous solution might be due to the ionic interaction between sCT and heparin in aqueous solution [10-11].

When HSA was added into the sCT aqueous solution, a clear solution was maintained for about 12 hrs. Beyond 12 hr-incubation time, the turbid dispersion was

Additives	r value*
-	0.823
Trehalose	0.943
Mannitol	0.933
HP-βCD	0.869
Sucrose	0.965
Dextran	0.864
Heparin	0.770
HSA	0.775

* data was calculated from Prestrelski's equation.

Table 1 Effects of various additives on the r value of spectral correlation coefficient of each sCT-additive lyophilized form.

occurred in the sCT-HSA aqueous solution. The second-derivative IR spectra of precipitate are obtained in Fig. 2F. The electrostatic repulsion between the two polymer chains might result in maintenance of a clear solution [12]. After long-tern incubation at 40°C beyond 12-hr, HSA might be absorbed onto the polymer chains of cationic sCT by inter/intra molecular hydrophobic interaction to cause an aggregate [13-14]. A strong peak at 1630 cm^{-1} with a minor peak at 1618 (1620) cm^{-1} was evidenced from the precipitate of sCT-HSA sample, indicating the marked β-sheet formation in the precipitate.

Additives affecting the conformational stability of sCT after co-lyophilization

Various additives affecting the structural stabilization of sCT during lyophilization were investigated by the approach of structural similarity. The effects of various additives on the spectral correlation coefficient between lyophilized sCT and native sCT are listed in Table 1. When the additive-free sCT was lyophilized from the aqueous solution, a high degree of conformational change was obtained as compared with native one, resulting in a poor r value of 0.823. This r value was markedly deviated from 1, strongly indicating that several stresses were applied to the additive-free sCT in the process of lyophilization. After incorporation of different additives, however, the r value was superior to the above data. The r values listed in Table I were 0.943, 0.933 and 0.965 for trehalose, mannitol and sucrose, respectively, higher than that of the additive-free lyophilized sCT, suggesting a good stabilization effect of these additives. The other additives exhibited a poor stabilization effect for the sCT after
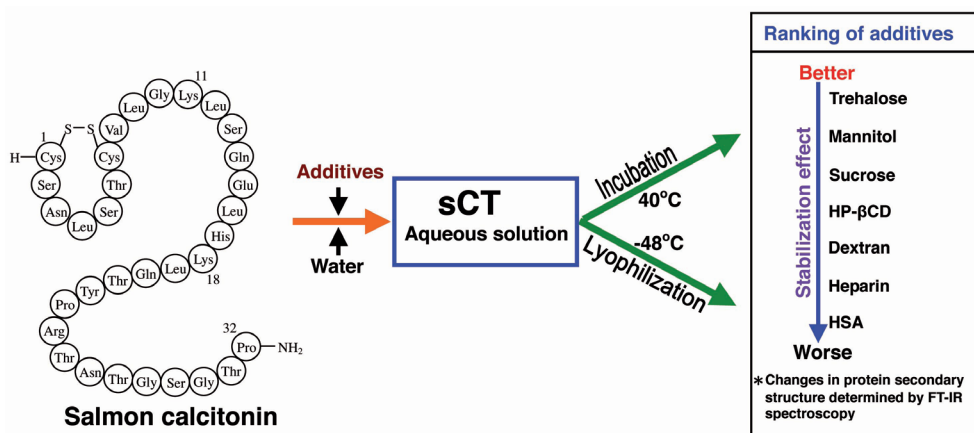
Fig. 3 The schematic ranking results for the additives affecting the structural stability of sCT in both aqueous solution and lyophilized solid state.

lyophilization, due to lower *r* value. The result shows that sCT might retain most of its native structure after co-lyophilizing with trehalose, mannitol or sucrose.

Conclusions

The schematic ranking results for the additives affecting the stability of sCT in both aqueous solution and solid state were illustrated in Fig. 3. The present study reveals that the conformational structure of additive-free sCT whether in aqueous solution or lyophilized form was found to be markedly altered, while both trehalose and mannitol seemed to be acted as good stabilizers for sCT in both aqueous solution and lyophilized form.

Acknowledgement

References

1. Hirsch PF, Baruch H. Is calcitonin an important physiological substance ? Endocrine. 21: 201-208, 2003.
2. Frokjaer S,. Otzen DE. Protein drug stability: A formulation challenge. Nat. Rev. Drug Discov. 4: 298-306, 2005.
3. Rathore N, Rajan RS. Current perspectives on stability of protein drug products during formulation, fill and finish operations. Biotechnol Prog. 24: 504-514, 2008.
4. Wang W. Instability, stabilization, and formulation of liquid protein pharmaceuticals. Int J Pharm. 185: 129-188, 1999.
5. Wang W. Lyophilization and development of solid protein pharmaceuticals. Int J Pharm. 203: 1-60, 2000.
6. Plosker G.L, McTavish D. Intranasal salcatonin: a review of its pharmacological properties

and role in the management of postmenopausal osteoporosis. Drugs Aging. 8: 378-400, 1996.

7. Lin SY, Lin CC, Lee TH. Different solid sample preparation methods affecting the spectral similarity of salmon calcitonin. Spectroscopy-An Int J. 24: 511-516, 2010.

8. Susi H, Byler DM. Protein structure by Fourier transform infrared spectroscopy: second derivative spectra. Biochem Biophys Res Commun. 115: 391-397,1983.

9. Prestrelski SJ, Tedeschi N, Arakawa T, Carpenter JF. Dehydration-induced conformational transitions in proteins and their inhibition by stabilizers. Biophys J. 65: 661-671, 1993.

10. Torres-Lugo M, Peppas NA. Molecular design and in vitro studies of novel pH-sensitive hydrogels for the oral delivery of calcitonin. Macromolecules. 32: 6646-6651, 1999.

11. Szelke H, Schübel S, Harenberg J, Krämer R. Interaction of heparin with cationic molecular probes: probe charge is a major determinant of binding stoichiometry and affinity. Bioorg Med Chem Lett. 20: 1445-1447, 2010.

12. Houska M, Brynda E. Interactions of proteins with polyelectrolytes at solid/liquid interfaces: Sequential adsorption of albumin and heparin. J Colloid Interface Sci. 188: 243-250, 1997.

13. Guo B, Anzai J, Osa T. Adsorption behavior of serum albumin on electrode surfaces and the effects of electrode potential. Chem Pharm Bull (Tokyo). 44: 800-803, 1996.

14. Langer K, Balthasar S, Vogel V, Dinauer N, von Briesen H, Schubert D. Optimization of the preparation process for human serum albumin (HSA) nanoparticles. Int J Pharm. 257: 169-180, 2003.

Synthesis of functionalized RNA: essential tools for the study of RNA structure and ribozyme function

Rublack N., Springstubbe D., Nguyen H., Appel B., Müller S.*

Institut für Biochemie, Ernst-Moritz-Arndt Universität Greifswald, D-17487 Greifswald, Germany

Summary

We report on the synthesis of RNA building blocks carrying amino linkers of distinct length and flexibility that upon incorporation in RNA can be used for post-synthetic attachment of dyes, reporter groups or other functionalities. Furthermore, we introduce a suitably activated flavine mononucleotide (FMN) derivative that can be attached to amino-modified RNA and used for the control of ribozyme activity.

Introduction

Synthetic RNAs carrying site-specific modifications are highly required for structure and function studies. However, only a very limited number of RNA phosphoramidites with a suitable functionality for post-synthetic attachment of dyes, reporter groups or other conjugates at internal positions is available. Therefore, a currently very active part of our research is focussed on the synthesis of 5'-O-dimethoxytrityl-2'-O-*tert*-butyldimethylsilyl protected 3'-O-phosphoramidites of nucleosides that carry amino linkers of different lengths and flexibility at the heterocyclic base, in particular at C5 of the pyrimidines as well as at C8 and C2 of the purines (Fig. 1). These derivatives, once introduced in RNA can be used for post synthetic functionalization [1,2]. In addition, we have synthesized a flavinmononucleotide (FMN) derivative that is post-synthetically attached to an amino-modified hairpin ribozyme derivative [2], constituting an FMN dependent riboswitch [3].

Materials and Methods

Amino-modified nucleosides were prepared as described [1,2]. Preparation of fully protected phosphoramidites of amino-modified nucleosides and their introduction in oligoribonucleotides as well as post-synthetic conjugation of fluorescence dyes are described in the same literature [1,2]. The synthesis of the flavine mononucleotide-linker conjugate and its post-synthetic coupling to amino-modified RNA is described in [2].
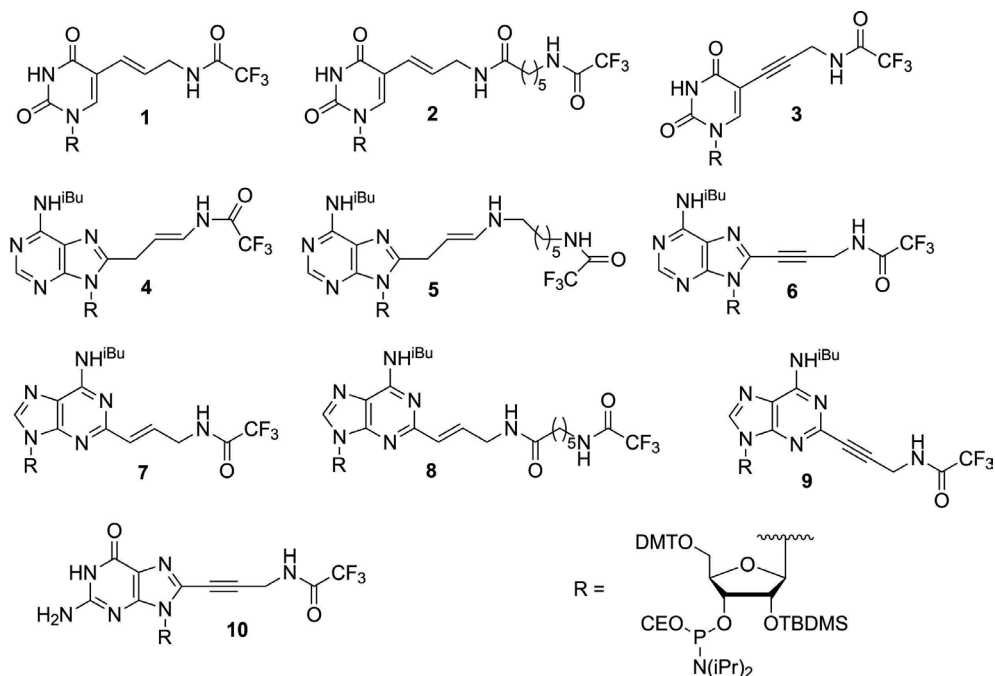
Fig. 1: Structures of amino-modified phosphoramidite building blocks.

Results

With the aim of providing a set of nucleotides that upon incorporation in RNA can be used for RNA functionalization at a desired internal site, we have synthesized various ribonucleoside phosphoramidite building blocks with amino linkers of different lengths and flexibility attached to the heterocyclic base (Fig. 1). In a first row of experiments, we have coupled three different linkers (a short and a long alkenyl and a short alkynyl linker as shown in Fig. 1) to C5 of uridine by palladium catalyzed cross-coupling reactions as described [1]. Adenosine derivatives with alkenyl linkers at C8 or C2 were prepared under analogous conditions as used for uridine derivatives **1** and **2**. However, a striking difference was the formation of double bond isomers in the Heck coupling reaction. Here, we observed a strong influence of the nature of the catalysts on formation of either isomer. Thorough investigation of a variety of catalysts and reaction conditions allowed us to tune reaction towards one of the two possible isomers by the choice of the catalysts. The specific amino-modified adenosine derivatives shown in Figure 1 were obtained with $Na_2[PdCl_4]$ (**4**, **5** and **8**) or with the catalyst palladacycle (**7**). The phosphoramidite building blocks **3**, **6**, **9** and **10** carrying the propargylamino linker were prepared by Sonogashira cross-coupling. The synthesis starts with the introduction of the DMT- and TBDMS protecting group via standard procedures. Then, the propargylamino linker was coupled to the nucleobase by Sonogashira reaction, and finally the phosphoramidite was prepared. Adenosine derivatives with the propargyl amino linker at C8 and C2 were prepared following
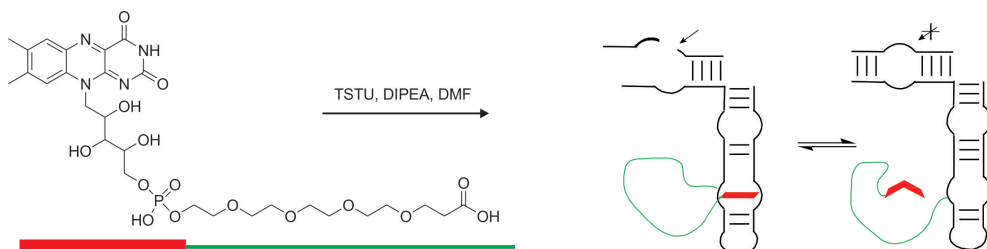
Fig. 2: Attachment of the FMN-linker conjugate to the hairpin ribozyme for conformational switching and activity control.

the same route. However, as an additional step, the exocyclic amino group of the base was protected prior to introduction of the other protecting groups and of the linker unit. The propargylamino linker was also attached to C8 of guanosine starting from 8-bromoguanosine. The synthesized phosphoramidite building blocks were successfully incorporated into oligonucleotides using standard solid phase chemistry. Amino-modified phosphoramidites were coupled for 5 min, as were the standard building blocks. The coupling yield was in the 99% range. Oligonucleotides were deprotected and purified by gel electrophoresis, followed by MALDI-TOF MS analysis. The amino-modified RNAs were subsequently labeled with a variety of fluorescent dyes using dye-linker conjugates carrying a terminal activated carboxyl group. Successful labeling was confirmed by HPLC and MALDI-TOF MS analysis. Several of the synthesized RNAs were used in fluorescence measurements, in particular in single molecule detection (SMD) and time correlated single photon counting (TCSPC) bulk experiments [1].

In addition to structural studies, specific RNA functionalization is also relevant to the study of RNA function. Previously, we have engineered an FMN responsive hairpin aptazyme that can be switched on and off in a reversible mode [3]. In this system, FMN can be removed from its binding pocket by reduction of the isoalloxazin ring, which is associated with a change in geometry and subsequently with loss of binding. Our current work in this project is focused on engineering a hairpin aptazyme with FMN being covalently attached to the aptazyme backbone allowing the FMN unit flipping in and out of the binding pocket dependent on its oxidation state (Fig. 2). For this purpose, a suitable FMN derivative for post-synthetic labeling of amino-modified RNA was to be prepared. Starting from riboflavin, first 2',3',4'-*O*-triacetyl riboflavin was synthesized as described [2]. Then, tetraethylene glycol was reacted with tert-butyl acrylate to yield the carboxylic acid containing linker component, which subsequently was converted to the corresponding phosphoramidite. The coupling reaction between the acetylated riboflavin and the linker phosphoramidite followed by removal of protecting groups delivered the FMN-linker conjugate with terminal carboxyl group, which upon activation as NHS ester was used for post-synthetic functionalization of hairpin ribozyme derivatives. Functional characterization of the resulting FMN-RNA constructs in ribozyme activity assays is in progress.

Conclusions

We have succeeded in the synthesis of a number of monomer building blocks that

upon incorporation in RNA allow for post-synthetic attachment of a desired functionality. Using dye labeled RNAs that were prepared with these building blocks, we have carried out an extensive analysis of the influence of the linker lengths and rigidity on the accuracy of FRET measurements [1]. Our work on FMN modified ribozymes shows, that in combination with the development of synthetic routes to appropriately activated modifiers, RNAs can be conjugated with a large variety of tags, making the nucleic acid not only visible in spectroscopic experiments, but adding also new functionalities.

References

[1] SINDBERT S., KALININ S., NGUYEN H., KIENZLER, A., CLIMA, L., BANNWARTH, W. APPEL B., MÜLLER S., SEIDEL C. A. M. Accurate Distance Determination of Nucleic Acids via Förster Resonance Energy Transfer: implications of Dye Linker Lenght and Rigidity, J. Am. Chem. Soc., 133, 2463-2480, 2011.

[2] RUBLACK N., NGUYEN H., APPEL B., SPRINGSTUBBE D., STROHBACH, D., MÜLLER, S. Synthesis of specifically modified oligonucleotides for application in structural and functional analysis of RNA. J. Nucleic Acids, 2011, in press, 2011.

[3] STROHBACH D., NOVAK N., MÜLLER S. Redox-active riboswitching: Allosteric regulation of ribozyme activity by ligand shape control, Angew. Chem. Int. Ed., 45, 2127-2129, 2006.

Interactions of polyamidoamine dendrimers with the plasmamembrane of neuronal cells

Pál I[*]., Nyitrai G., Kékesi O., Simon Á., Kardos J.

Department of Neurochemistry, Institute of Biomolecular Chemistry, Chemical Research Center, Hungarian Academy of Sciences, Budapest, Hungary.
* correspondence: ildiko.pal@chemres.hu

Summary

We have recently published that polycationic PAMAM generation 5 (G5-NH$_2$-100) dendrimer impairs hippocampal neurons via plasmamembrane depolarization, explained by molecular simulation of interactions of the PAMAM monomer with either the membrane or the membrane-protein potassium channel. Predicted molecular mechanisms were substantiated in measurements of the effects of G5-NH$_2$-100 on potassium channel. G5-NH$_2$-100 (0.1 mg/ml) decreased voltage-dependent potassium currents of pyramidal neurons and increased mixed "leak" currents in rat brain hippocampal slices. Moreover, confocal fluorescence imaging indicated that G5-NH$_2$-100 also depolarized cell mitochondria. Our data supports the hypothesis that G5-NH$_2$-100 may also affect the mitochondria through inhibition of potassium currents and increased mixed conductance.

Introduction

Protein-like polyamidoamine PAMAM dendrimers are capable to cross the plasmamembrane as well as the blood-brain barrier and these features are crucial in their utilization in medical applications (Yang 2010; Huang et al., 2007; Gupta et al., 2006).

In our recent study we revealed short-term functional neurotoxicity of PAMAM dendrimers. Polycationic PAMAM generation 5 dendrimer (G5-NH$_2$-100, 0.01-1.0 mg/ml) increased drastically and irreversibly the permeability of plasmamembrane, depolarized and inactivated most of the neurons and increased the number of dead cells in hippocampal slices. Conjugation by β-D-glucopyranose, however, decreased the toxic effects of G5-NH$_2$-100 applied in lower concentrations (0.01-0.10 mg/ml). By contrast, polyanionic G4.5-COONa, containing surface carboxyl groups affected the membrane potential much less, and did not affect cell viability (Nyitrai et al., 2011). These effects were explained by molecular simulation of interactions of the

PAMAM monomer with either the membrane or the membrane-protein potassium channel. In order to substantiate these findings, G5-NH$_2$-100 action mechanisms were further characterized in measurements of the effects of G5-NH$_2$-100 on voltage-dependent potassium currents as well as on mitochondrial membrane potential in rat brain hippocampal slices.

Methods

PAMAM dendrimer (G5-NH$_2$-100) was purchased from Dendritech Inc. (Dendritech. com, USA). All other chemicals used in this work were obtained from commercial sources.

Animal experiments were carried out in accordance with the European Communities Council Directive of 24 November 1986 (86/609/EEC). Transverse 400 µm thick hippocampal slices of juvenile (10-16 days old) male Wistar rats (Toxicoop, Budapest, Hungary) were prepared as described elsewhere (Nyitrai et al., 2011). Slices were submerged and perfused at 2 ml/min by artificial cerebrospinal fluid (ACSF, composition in mM: 129 NaCl, 10 glucose, 3 KCl, 1.25 NaH$_2$PO$_4$, 1.8 MgSO$_4$, 2 CaCl$_2$ and 21 NaHCO$_3$), saturated with carbogen (5 % CO$_2$ + 95 % O$_2$), pH 7.4).

Whole-cell voltage-clamp recordings were performed as described elsewhere (Nyitrai et al., 2011). Briefly, the intracellular solution (containing in mM: 135 KGluconate, 10 NaCl, 0.05 CaCl$_2$, 2 ATP, 10 4-(2-hydroxyethyl)-1-piperazineethanesulfonic acid, 1 ethylene glycol tetraacetic acid; pH set to 7.3) was filled into 3-5 MΩ pipettes. Recordings were performed with two-channel Multiclamp 700A amplifier (Axon Instruments) and traces were digitized at 10 kHz with a Digidata 1320A A/D board (Axon Instruments) controlled by a computer running pClamp8.

In order to record voltage-dependent potassium currents, slices were perfused with ACSF containing a mixture of inhibitors such as antagonist of voltage activated Na$^+$ and Ca^{2+} channels (1 µM, tetrodotoxin:TTX and 300 µM CdCl$_2$ respectively), NMDA glutamate receptor antagonist (100 µM, DL-2-Amino-5-phosphonopentanoic acid:APV), AMPA/kainate glutamate receptor antagonist (10 µM, 6-Cyano-7-nitroquinoxaline-2,3-dion:CNQX), GABA$_A$ receptor antagonist (100 µM, picrotoxin). After 10 minutes of perfusion with the inhibitors, CA3 pyramidal neurons were voltage-clamped at -80 mV and depolarized with a series of step pulses from -70 to 50 mV with 10 mV increments. G5-NH$_2$-100 (0.1 mg/ml, in ACSF containing the inhibitors) was applied for 15 minutes and the voltage protocol was applied again to the same cell.

In order to monitor changes in mitochondrial membrane potential, rat brain hippocampal slices were loaded with the fluorescent indicator of mitochondrial membrane potential rhodamine-123 (Rh-123, 15 µg/ml) for 50 minutes at 25 ºC (Kovács et al., 2005). Dye-loaded slices were placed into the observation chamber and superfused with ACSF and G5-NH$_2$-100 (0.1 mg/ml in ACSF). Change in Rh-123 fluorescence (λ_{ex} = 488 nm, λ_{em} = 510-530 nm) was imaged by a confocal laser fluorescence microscope (FluoView300, Olympus, Hungary) after 5 minutes of ACSF perfusion (control image) and after 30 minutes application of G5-NH$_2$-100.

Results

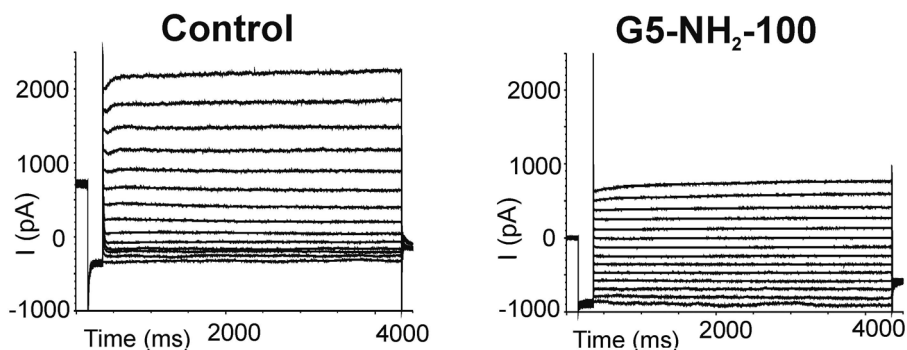In voltage-clamp experiments, 15 min application of G5-NH$_2$-100 (0.1 mg/ml)

Fig. 1. Current traces recorded from a pyramidal neuron depolarized with step pulses from -80 to 50 mV with 10 mV increments after 10 min application of CNQX, APV, Picrotoxin, TTX and CdCl$_2$ (control) and after addition of G5-NH$_2$-100 (0.1 mg/ml, 15 min).
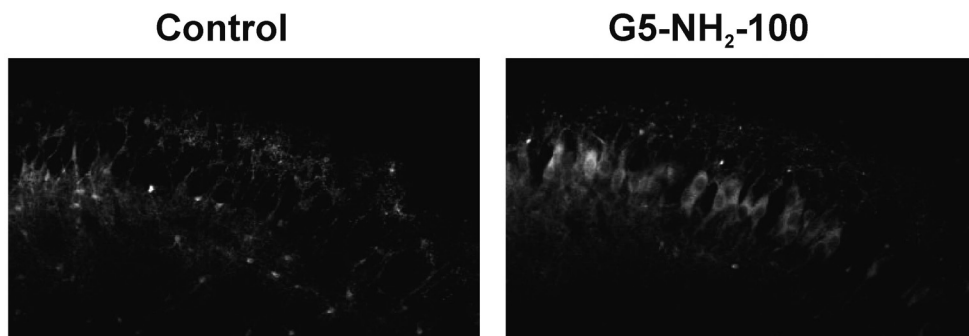

Fig. 2. Rhodamine-123 staining indicated mitochondrial depolarization of cells in the CA3 region of the rat hippocampus after 30 minutes of G5-NH$_2$-100 application (0.1 mg/ml).

decreased the voltage-dependent potassium currents and increased "leak" (probably mixed Na$^+$, K$^+$, Cl$^-$) currents at negative membrane potentials (Fig 1.). These findings support model simulations, predicting interactions of PAMAM dendrimers with the plasmamembrane and integral potassium channels (Nyitrai et al., 2011).

Under control conditions, Rh-123 enters mitochondria and, due to self-quenching, the overall fluorescence is low. When the mitochondria depolarize, dye leaves the mitochondria resulting in fluorescence enhancement. Application of G5-NH$_2$-100 (0.1 mg/ml, 30 min) did increase Rh-123 fluorescence in CA3 pyramidal cells (Fig 2.), indicating mitochondrial depolarization.

Conclusions

Short-term functional neurotoxicity of G5-NH$_2$-100 (Nyitrai et al., 2011) may be explained by mitochondrial depolarization through inhibition of potassium currents and elevation of "leak" currents.

Acknowledgements

References

Gupta U, Agashe HB, Asthana A, Jain NK. 2006. A review of in vitro-in vivo investigations on dendrimers: the novel nanoscopic drug carriers. Nanomedicine 2:66-73.

Huang RQ, Qu YH, Ke WL, Zhu JH, Pei YY, Jiang C. 2007. Efficient gene delivery targeted to the brain using a transferrin-conjugated polyethyleneglycol-modified polyamidoamine dendrimer. FASEB J 21:1117-1125.

Kovács R, Kardos J, Heinemann U, Kann O. 2005. Mitochondrial calcium ion and membrane potential transients follow the pattern of epileptiform discharges in hippocampal slice cultures. J Neurosci 25:4260-4269.

Nyitrai G, Kékesi O, Pál I, Keglevich P, Csíki Z, Fügedi P, Simon A, Fitos I, Németh K, Visy J, Tárkányi G, Kardos J. Assessing toxicity of polyamidoamine dendrimers by neuronal signaling functions. Nanotoxicology. 2011 Jun 20. [Epub ahead of print]

Yang H. 2010. Nanoparticle-mediated brain-specific drug delivery, imaging, and diagnosis. Pharmacol. Res. 27:1759-1771.

Chemical study of the carbon dioxide influence on cultural heritage

Pică E. M.[1], Bolunduţ L. C.[1], Popişter I.[1], Neamţu C. I.[1], Pirău L. C.[1], Duca V.[2]

[1]*Department of Chemistry, Technical University of Cluj-Napoca, Memorandumului Street no. 28, Cluj-Napoca, Romania*
(empica@yahoo.com, liviu.bolundut@chem.utcluj.ro)
[2]*Department of Mineralogy, "Babes-Bolyai" University,*
Cluj-Napoca, Romania

Abstract

A chemical study of the carbon dioxide influence on cultural heritage is presented.

The CO_2 concentration of the solutions used in the study was determined by linear voltammetry and impedance spectra.

We tried to simulate a polluted environment for the building materials used at monuments (in this case, limestone-$CaCO_3$). To estimate the decay process we present X-ray Powder diffractions which determine the initial mineralogical content of the limestone and the mineralogical content after the chemical reactions with the solutions.

Introduction

The historical heritage is very important for any nation, being a source for the development of the tourism and its competitivity. The cultural tourism and historical heritage management operate as parallel activities in most places, with remarkably little dialogue between the two [1, 2]. The purpose of this study was to simulate a polluted environment and to determine the effects of acid rain on building materials used at monuments. A similar study was made in the literature [3], but under different conditions.

Materials and Methods

Materials and apparatus used: sodium carbonate solutions, Vistea limestone, Versa-STAT 3 (V3 Studio software Princeton Applied Research), electrochemical cell (with three electrodes: working electrode with a copper surface, saturated calomel reference
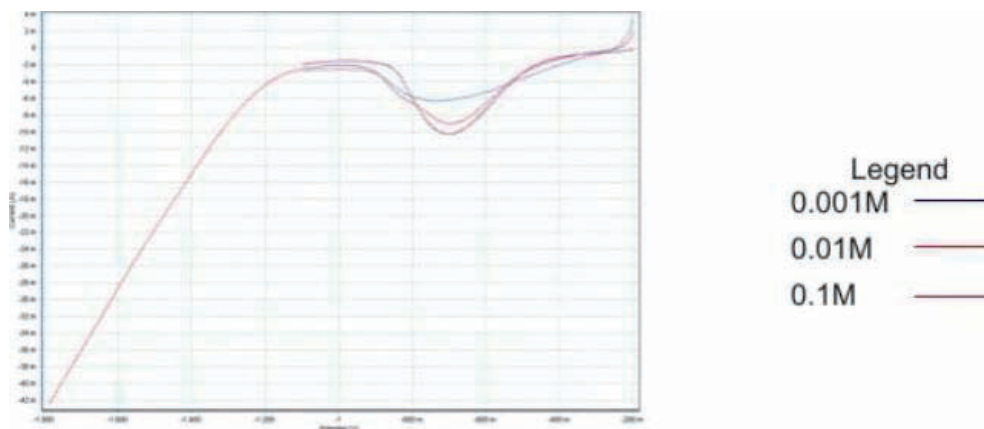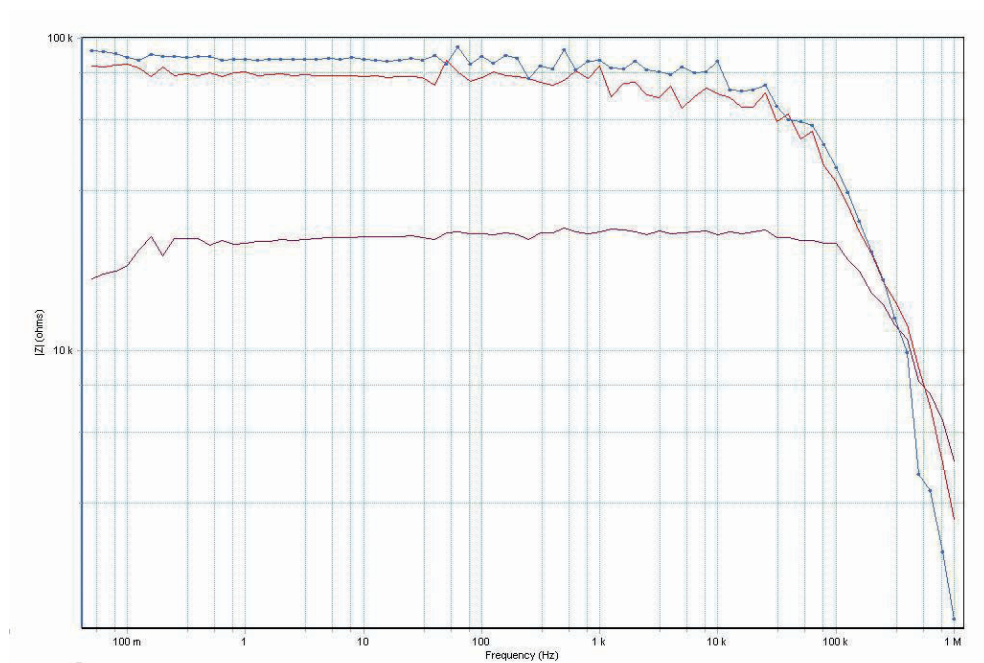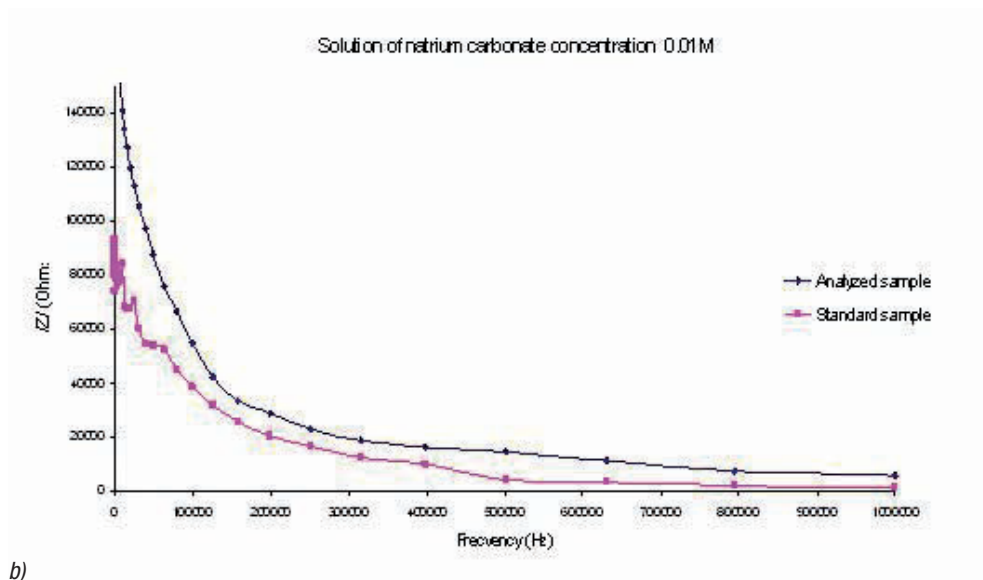
Fig.1. Linear voltammograms

a)

Fig.2. Impedance spectra: a) standard solutions (10^{-1}-10^{-3} M), b) standard solution and analyzed 0.01M solution.

electrode and platinum counter electrode), optical microscope (Metaloplan/Orthoplan Leitz Wetzlar) and X-ray diffraction apparatus (DRON 3).

Methods used: voltammetry, impedance spectroscopy, optical microscopy and X-ray powder diffraction.

Results

Standard solutions of sodium carbonate (10^{-1}-10^{-3} M) were used, and linear voltammograms (figure 1) were registered using the specific software [4]. The reduction of CO_2 takes place on the cooper surface. The electro-reduction peak of carbon dioxide appear at -0.7 V.

The results of impedance spectra are presented in figure 2.

The linear voltammograms and impedance spectra reveal a variation of CO_2 (concentration from the solutions).

The next step in our study was to prepare some samples of Vistea limestone and immerse them in sodium carbonate solutions at various concentrations. After a month the limestone samples were removed from solutions and analyzed.

The optical microscopy study of the Vistea limestone reveals that on the surface small crystals of calcite appear, which means that the samples absorbed the carbonate ions from solutions. This fact is confirmed by the impedance spectra on the solution (figure 2b) in which the solid samples were immersed. Also an erosion process followed by a resedimentation one can be observed (figure 3).

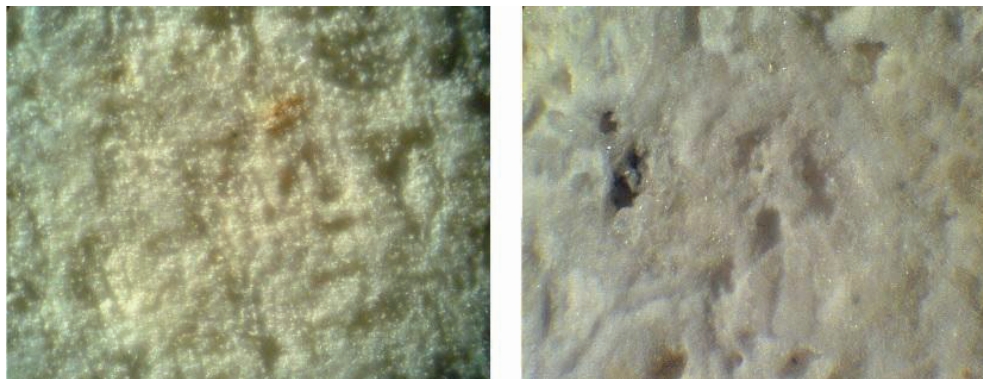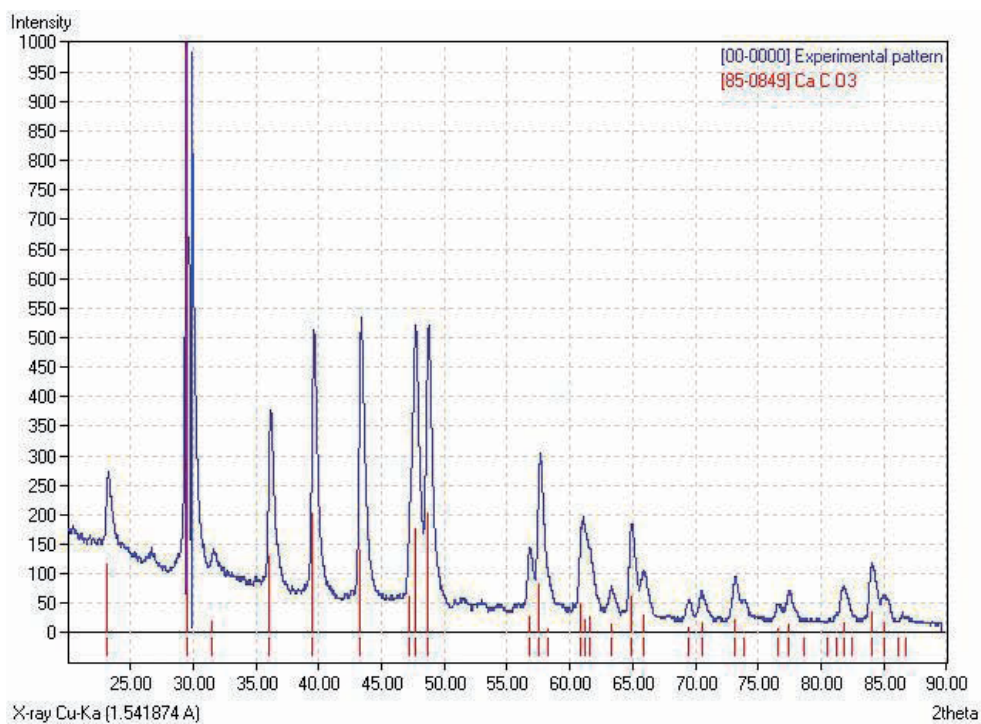X-ray powder diffraction results are showed in figure 4.

Fig.3. Optical microscopy: a) before immersion, b) after immersion.
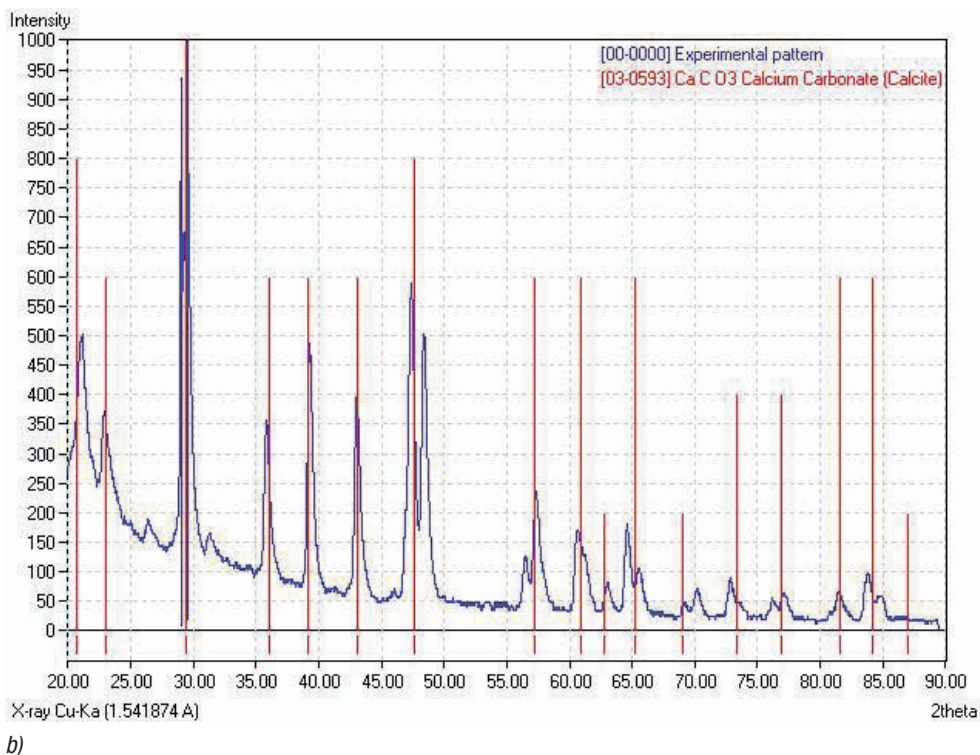

a)

Fig.4. The X-ray powder spectra: a) before immersion, b) after immersion.

Conclusions

➢ After the results were interpreted, we can say that the "recipe" used in our study can recreate a natural acid environment that can cause serious damages to the monuments.

➢ The linear voltammograms and the impedance spectra present a variation with the concentration of carbonate ions (carbon dioxide) from solutions. The impedance spectra show that the concentration of carbon dioxide from the solutions in which the samples were immersed was smaller than the carbon dioxide concentration from the standard solution (before immersion).

➢ The carbon dioxide electro-reduction peak appears at -0.7 V.

➢ The optical microscopy reveals an erosion process followed by a resedimentation process.

➢ The X-ray powder analysis confirms that the calcite ($CaCO_3$) is the major compound.

Acknowledgement

References

BOB Mc KERCHER, HILARY du CROS, Cultural Tourism: The Partnership between Tourism and Cultural Heritage Management, Binghamton, NY, Haworth Hospitality Press 2002. [1]

I. POPIŞTER, L.C. PIRĂU, V. DUCA, E.M. PICĂ Tourism sustainable Development vs. degradation of monuments, Studies and Research, Series Geology-Geography, Bistriţa, RO, 23-28, 2011, in Press. [2]

E. P. HYATT, I. B. CUTLER, M. E. WADSWORTH, Calcium Carbonate decomposition in carbon dioxide atmosphere, J. Am. Ceram. Soc. 41, 70-74, 1958. [3]

* * * Princeton Applied Research V3-Studio Software. [4]

Functionalization of Amide-Building Blocks with endo-Gd-N-Cluster-Fullerene for Synthesis of BioShuttle Conjugates as cell-specific intracellular MR-Contrast Agents

Pipkorn R[1], Wiessler M[2], Dunsch L[3], Bock M[2], Waldeck W[4], Braun K[2]

[1] Core Facility Peptide Synthesis, German Cancer Research Center, INF 580, D-69120 Heidelberg, Germany
[2] Department of Medical Physics in Radiology, German Cancer Research Center, INF 280, D-69120 Heidelberg, Germany
[3] Department of Electrochemistry and conducting Polymers; Leibniz-Institute for Solid State and Materials Research, Helmholtzstraße 20, D-01069 Dresden, Germany
[4] Biophysics of Macromolecules, German Cancer Research Center, INF 580, D-69120 Heidelberg, Germany

Summary

In the field of diagnostics manifold methodologies exist to image morphological structures of tissues. Magnetic Resonance Imaging (MRI) is considered as an excellent tool to investigate detailed anatomical informations. Additionally, the MR got the ability to image metabolic processes and can act in the high field MRI as a new intracellular contrast agent which based on the BioShuttle carrier variant $GdSc_2N@C_{80n}$ called Gd-cluster@-BioShuttle. As a cargo PNA-building blocks like the amide's backbone were attached to the carrier module after functionalization with the Gd-cluster@ by the DAR_{inv}-mediated "Click Chemistry". Here we demonstrate shortly the synthesis and we like to approach this research subject from different angles including the development of tools for better monitoring of therapeutic interventions.

Introduction

The "-Omics" age encompasses comprehensively the bioinformatic-derived –omic approaches like genomics, metabolomics and proteomics and opens the door to the identification, characterization and quantitation of the complete glamorous interplay of the genes and their corresponding products. [1-3] The amounts of resulting data are huge and were increasingly extended by integration of these multifaceted -omics data. Standardization of the procedures and development of databases are essential.
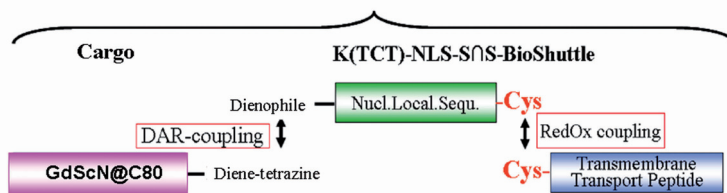
<Figure 1>illustrates the schematic structure of the Gd-cluster@-BioShuttle which consists of the following functional units: The transmembrane transport module (blue/white) which is responsible for the passage across cell membranes. It is connected via a disulfide bridge to the module which enables the active transport into the nucleus (NLS). After the enzymatic cleavage of the disulfide bridge in the cytoplasm the NLS module (green/white) is liberated. This in turn is covalently ligated to the GdScN@C80 MR-imaging component as a cargo (magenta/white) by DARinv Click chemistry.

[4-7] It is evident that the -omics' importance is strongly expanding. The search with "-omics" in the NCBI database "PubMed" finds 1669 publications between the first publication by Aardema and MacGregor in 2002 [8] and recently on September 30 2011 [9] and supports the prediction of the -omics' significance for successful therapeutic interventions. [10] The -omics' development does not stop at the diagnostic fields but it is less investigated. Manifold technologies, like antibody microarrays [11], metabolic biomarkers [12, 13], optical imaging of molecular signatures in inflammatory processes [14], and mass spectrometry methods [15], contribute to the refinement of the diagnostic precision towards improved treatments for personalized medicine. [16-18] Design and development of "-omics" approaches puts high demands on the chemical synthesis. Methodologies like the solid phase peptide synthesis (SPPS) and ligation strategies based on the "Click Chemistry" Diels-Alder-Reaction with inverse electron demand (DAR$_{inv}$), introduced by Merriefield [19] and Sharpless [20] respectively, are qualified for the production of pharmacologic active molecules and imaging components under non stringent chemical reaction conditions, in high yields and purity. From the "-omics" point of view, here we present again the chemical design of a promising diagnostic molecule as first documented by Wiessler [21] eligible as a MR contrast agent and its preliminary tests.

Chemical Procedures & Results

The BioShuttle carrier is modularly constructed as illustrated in Figure 1. It consists of a module facilitating the passage across the cell membrane (blue/white). This is connected via a disulfide bridge to a module, responsible for active transport into the cell nucleus (green/white), at which in turn a dienophile component is attached. It acts as a reaction partner of the imaging molecule (magenta/white) functionalized with a diene component for ligation via the DAR$_{inv}$ based Click Chemistry as documented by Braun 2010 [21].
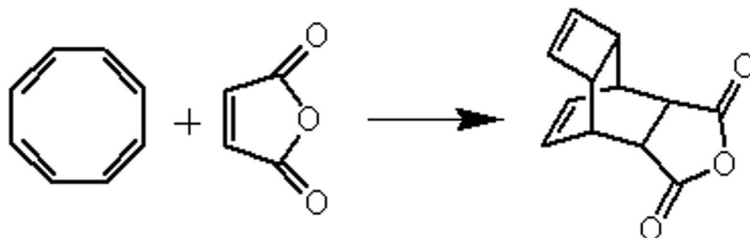
<Figure 2>illustrates the classical chemical reaction of the cyclooctotetraene with maleic anhydride to the reaction product tetracyclo-3,5-dioxo-4-aza-9,12-tridecadiene (dienophile) ("Reppe anhydride").
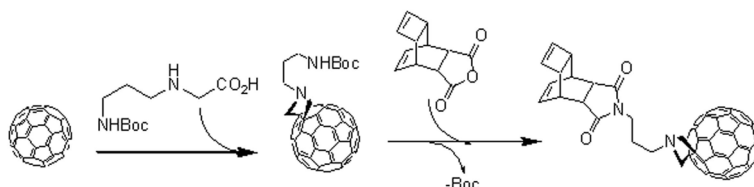
<Figure 3>exemplifies the functionalization of the GdxSc3-xN@C80. The Reppe anhydride (after reaction with the 1,3-dipolar cycloaddition of the Boc protected N-1.3.-diamino propane linker substituted glycine) reacts with the GdxSc3-xN@C80.

Syntheses of the dienophile component

Figure 2 describes the scheme of the classical chemical reaction of cyclooctote-traene with maleic anhydride to the resulting reaction product tetracyclo-3,5-dioxo-4-aza-9,12-tridecadiene (TcT) called "Reppe anhydride" used as dienophile reaction partner [22].

Syntheses & functionalization of the Gd-Cluster@C80

The synthesis of the imaging component Gd-Cluster@C_{80}(TcT-N-propyl]-N-glycyl-GdSc2@C80n) was carried out by a modified Kraetschmer-Huffmann direct current (DC) arc-discharge method [23]. The chemical reaction steps first documented by Kordatos in 2001 [24] for functionalization are shown in the scheme of Figure 3.

Figure 4 highlights the reaction of the reaction of N-(2-aminopropyl)-4-(6-(pyrimidine-2-yl)-1,2,4,5-tetrazine-3-yl)benzamide with the NLS-Cys and its subsequent coupling to the cell penetrating peptide (CPP-Cys) via disulfide bridge formation to the tetrazine-NLS-S∩S-CPP.

The final reaction product [diene] of Figure 4 reacts with the product [dienophi-le] in Figure 3 to N-(2-Aminopropyl)-4-(6-(pyrimidine-2-yl)-1,2,4,5-tetrazine-3-yl) benzamide (4)-NLS-S∩S-CPP (Gd-cluster@-BioShuttle) by the DAR_{inv} chemistry as pictured in Figure 5 and documented in detail [21].

We incubated and tested the Gd-cluster@-BioShuttle in MDA-MB231 breast adeno-carcinoma cells in a dilution series which resulted in substantially reduced measurement
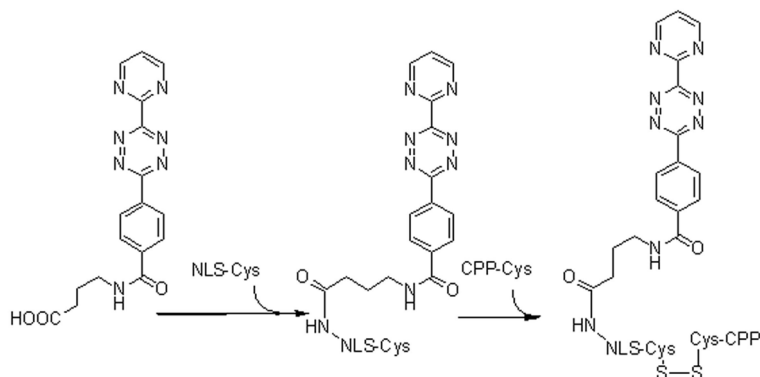
<Figure 4>the resulting intermediate is composed of N-(2-aminopropyl)-4-(6-(pyrimidine-2-yl)-1,2,4,5-tetrazine-3-yl)benzamide (diene) and connected via a linker sequence to the nuclear localization sequence (NLS). This is ligated via a disulfide bridge to the cysteines of the transmembrane transport and the NLS modules.
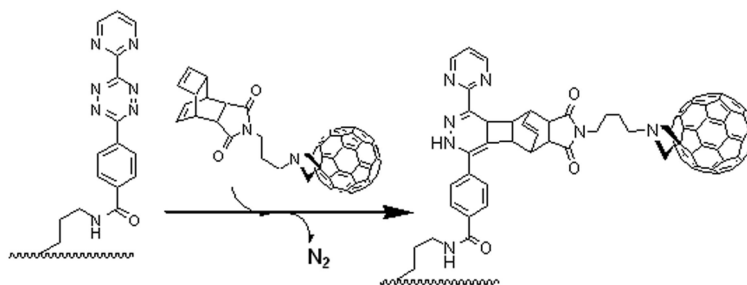
<Figure 5>elucidates the DAR with inverse electron demand as the ligation step to the Gd-cluster@-BioShuttle for use in MR imaging tests as detailed [21]
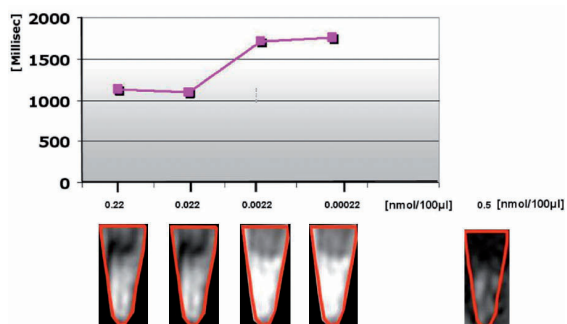
<Figure 6>shows an imaging of T1 weighted relaxation times. The ordinate of the graph in the upper part of the figure shows the relaxation times [msec], the axis of the abscissa represents the concentrations of the dilution series of the Gd-cluster@-BioShuttle, as documented in 2010 [21]. As a reference Gd-DTPA (Magnevist®) was used [0.5 nmol/ 100 µL].

periods (T1 relaxation) and increased tomographically generated signal intensities at the same time as shown in the graph together with the MR-imaged in MDA-MB231 cells in reaction tubes in Figure 6. As documented [21], the single tube (right) represents the probe with the commonly used 2-[bis[2-[carboxymethyl-(2-oxido-2-oxoethyl) amino]ethyl]amino]acetate; Gd^{+3} (2R,3R,4R,5S)-6-methylaminohexane-1,2,3,4,5-pentol (gadopentetate dimeglumine [Gd-DTPA]) as a control.

References

[1] Casado-Vela J., Cebrian A., Gomez Del Pulgar M.T., Lacal J.C. Approaches for the study of cancer: towards the integration of genomics, proteomics and metabolomics. *Clin Transl Oncol* ;**13**:617-28;2011

[2] Okubo K., Matsumoto K., Ssito H. ["Omics" study of diseases]. *Nihon Jibiinkoka Gakkai Kaiho* ;**114**:51-9;2011

[3] Yang J.Y., Karr J.R., Watrous J.D., Dorrestein P.C. Integrating '-omics' and natural product discovery platforms to investigate metabolic exchange in microbiomes. *Curr Opin Chem Biol* ;**15**:79-87;2011

[4] Kumar V. Omics and literature mining. *Methods Mol Biol* ;**719**:457-77;2011

[5] Rogers S. Statistical methods and models for bridging Omics data levels. *Methods Mol Biol* ;**719**:133-51;2011

[6] Schneider M.V., Orchard S. Omics technologies, data and bioinformatics principles. *Methods Mol Biol* ;**719**:3-30;2011

[7] Gehlenborg N., O'Donoghue S.I., Baliga N.S., Goesmann A., Hibbs M.A., Kitano H. et al. Visualization of omics data for systems biology. *Nat Methods* ;**7**:S56-S68;2010

[8] Aardema M.J., MacGregor J.T. Toxicology and genetic toxicology in the new era of "toxicogenomics": impact of "-omics" technologies. *Mutat Res* ;**499**:13-25;2002

[9] Jin H., Lee H.C., Park S.S., Jeong Y.S., Kim S.Y. Serum cancer biomarker discovery through analysis of gene expression data sets across multiple tumor and normal tissues. *J Biomed Inform* ;2011

[10] Yang X., Jiao R., Yang L., Wu L.P., Li Y.R., Wang J. [New-generation high-throughput technologies based 'omics' research strategy in human disease]. *Yi Chuan* ;**33**:829-46;2011

[11] Wingren C., Borrebaeck C.A. Antibody microarrays: current status and key technological advances. *OMICS* ;**10**:411-27;2006

[12] Paolucci U., Vigneau-Callahan K.E., Shi H., Matson W.R., Kristal B.S. Development of biomarkers based on diet-dependent metabolic serotypes: characteristics of component-based models of metabolic serotypes. *OMICS* ;**8**:221-38;2004

[13] Serkova N.J., Christians U. Biomarkers for toxicodynamic monitoring of immunosuppressants: NMR-based quantitative metabonomics of the blood. *Ther Drug Monit* ;**27**:733-7;2005

[14] Ntziachristos V. Optical imaging of molecular signatures in pulmonary inflammation. *Proc Am Thorac Soc* ;**6**:416-8;2009

[15] Zhang X., Wei D., Yap Y., Li L., Guo S., Chen F. Mass spectrometry-based "omics" technologies in cancer diagnostics. *Mass Spectrom Rev* ;**26**:403-31;2007

[16] Sorlie T. Molecular classification of breast tumors: toward improved diagnostics and treatments. *Methods Mol Biol* ;**360**:91-114;2007

[17] Jain K.K. Challenges of drug discovery for personalized medicine. *Curr Opin Mol Ther* ;**8**:487-92;2006

[18] Wiwanitkit V. Cancer immunomics and application of 'omics' for cancer management. *Expert Rev Clin Immunol* ;**3**:807-12;2007

[19] Merriefield R.B. Solid Phase Peptide Synthesis. I The Synthesis of a Tetrapeptide. *J Americ Chem Soc* ;**85**:2149-54;1963

[20] Kolb H.C., Finn M.G., Sharpless K.B. Click Chemistry: Diverse Chemical Function from a Few Good Reactions. *Angew Chem Int Ed Engl* ;**40**:2004-21;2001

[21] Braun K., Dunsch L., Pipkorn R., Bock M., Baeuerle T., Yang S. et al. Gain of a 500-fold sensitivity on an intravital MR contrast agent based on an endohedral gadolinium-cluster-fullerene-conjugate: a new chance in cancer diagnostics. *Int J Med Sci* ;**7**:136-46;2010

[22] Reppe W., Schlichting O., Klager K., Toepel T. Cyclisierende Polymerisation von Acetylen I. *Justus Liebigs Annalen der Chemie* ;**560**:1-92;1948

[23] Dunsch L., Yang S. Endohedral clusterfullerenes--playing with cluster and cage sizes. *Phys Chem Chem Phys* ;**9**:3067-81;2007

[24] Kordatos K., Bosi S., Da R.T., Zambon A., Lucchini V., Prato M. Isolation and characterization of all eight bisadducts of fulleropyrrolidine derivatives. *J Org Chem* ;**66**:2802-8;2001

Amyloid Protein Aggregation: Structural Transitions Observed by Atomic Force Microscopy and Force Spectroscopy

Pires RH[1,2§], Saraiva MJ[2,3], Damas AM[2,3§], Kellermayer MS[1§]

[1]*Department of Biophysics and Radiation Biology, Semmelweis University. Budapest, HUNGARY*
[2]*Institute for Molecular and Cell Biology, University of Porto. Porto, PORTUGAL.*
[3]Instituto de Ciências Biomédicas Abel Salazar, University of Porto. *Porto, PORTUGAL.*
§ *To whom all correspondence should be addressed at:*
Ricardo H. Pires: ricardo.pires@eok.sote.hu; Ana M. Damas: amdamas@ibmc.up.pt; Miklós S. Kellermayer: miklos.kellermayer@eok.sote.hu.

Summary

Protein aggregation in the form of amyloid fibrils is associated with highly debilitating and currently incurable neurological and systemic disorders. The cytotoxicity of these amyloid aggregates is currently unknown, but it has been hypothesized to derive from the transient assembly of annular oligomers. In this work, using atomic force microscopy (AFM), we have followed the aggregation of transthyretin (TTR) and identified the presence of annular oligomers. Probing these oligomers by force spectroscopy revealed several saw-tooth force-extension patterns that follow the worm-like chain (WLC) model of entropic elasticity. This observation indicates that annular oligomers are amenable to be studied by already established frameworks of molecular physics in force-induced unfolding of single molecules, from which relevant structural data may be obtained.

Introduction

Amyloid is a general term often referring to abnormal proteinatious deposits that accumulate in the extracellular space and that are associated with a variety of neurological and systemic disorders (1). When observed with high-resolution microscopy methods the amyloid deposits of different diseases reveals the ubiquitous presence of straight and long fibrils exhibiting a periodic helical pattern (1). These fibrils typically result from the self-assembly of misfolded protein molecules that under normal conditions should have been processed and cleared away through proteolytic degradation. From *in vitro* studies it was found that the formation of amyloid fibrils is preceded by the formation of intermediate oligomeric species (2). Recent reports suggest that it is at

this intermediate stage of aggregation that amyloid exhibits its highest toxic potential (3). In particular, electrophysiology studies suggest that cytotoxicity of intermediates may be derived from increased permeation of the cell membrane that may disturb ionic balances thus ultimately leading to cell injury and death (4). This "ion-channel" hypothesis for amyloid toxicity has also been supported by the observation of annular oligomers in pre-fibrillar stages in several amyloidogenic preparations (4).

Although annular oligomers appear to be particularly attractive in the study of amyloidogenesis, their occurrence in amyloid preparations is transient. Furthermore, often at intermediate stages of aggregation a variety of different oligomers can be observed (2) which altogether complicates their individual structural analysis by conventional structure determination methods. On the contrary, the atomic force microscope allows the visualization of individual protein molecules and assemblies and, when coupled to force spectroscopy, allows the determination of their molecular properties (5).

Here we investigated the amyloid aggregation pathway of transthyretin (TTR), a human protein responsible for the transport of thyroid hormones and co-transport of vitamin A. Aggregation of TTR is associated with two main forms of amyloidosis: senile systemic amyloidosis involving the wild-type form of TTR (6), and familial amyloid polyneuropathy arising from mutations in the TTR gene (7). We found that along the TTR aggregation pathway annular oligomers were formed. We then probed these intermediate species by force spectroscopy and found that they showed force-extension patterns that are typically observed in single-molecule force-induced protein unfolding experiments.

Materials and methods

Recombinant wild-type TTR was purified, incubated to form amyloid aggregates that were imaged with the AFM as described elsewhere (8). A cantilever with its spring constant previously determined (~25 pN/nm), was used to probe annular oligo-mers in force spectroscopy experiments at a constant velocity of 250 nm/s. The force transition events obtained from each pulling experiment were fitted to the worm-like chain model of entropic elasticity.

Results

Annular oligomers were detected for the first time in the first week of incubation (figure 1A). The annuli appeared to have a relatively homogeneous diameter, although their height would vary within 1-2 nm between different annuli indicating some degree of structural heterogeneity. Annular oligomers were then subjected to force spectroscopy (pulling) experiments as schematically represented in figure 1B. The obtained force-extension curves typically showed a succession of force transitions with an apparent hyperbolic profile (figure 1C). Each force transition could be reasonably fitted with the worm-like chain (WLC) model of entropic elasticity restricted to a persistence length of 0.4 nm that is characteristic of pulling single protein molecules and reflects the distance between adjacent residues within a polypeptide chain. The observed transitions are likely associated with different protein domains and possibly represent the successive unfolding of individual secondary or tertiary structural elements.
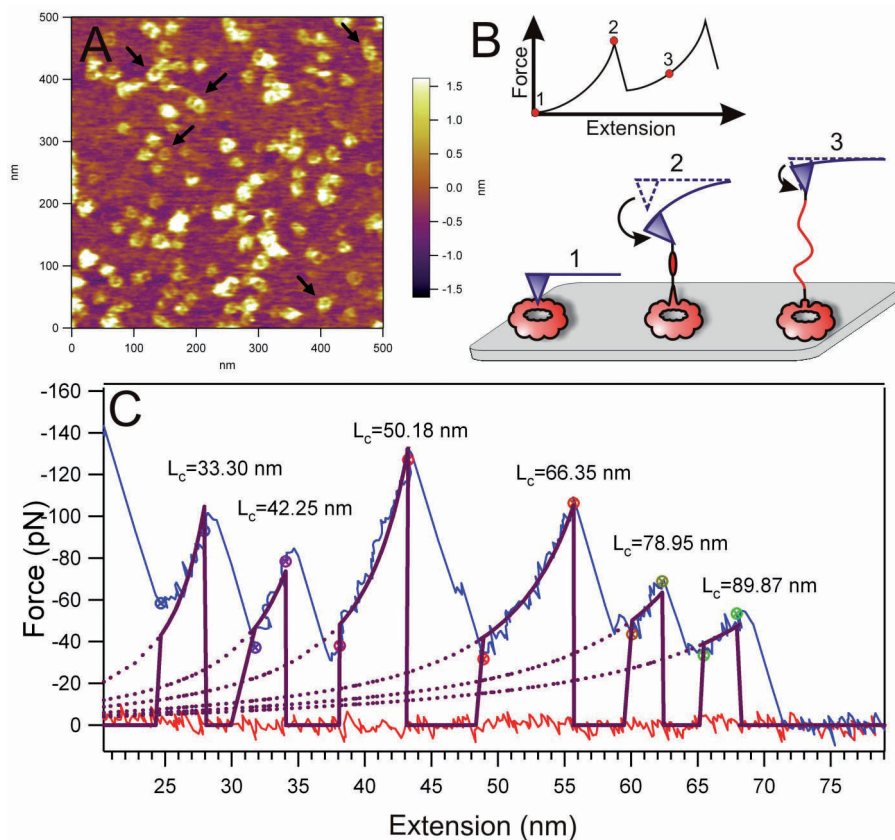
Figure1: Imaging and manipulation of TTR annular oligomers. (A) TTR annular oligomers were observed at early stages of aggregation (arrows indicate some better resolved annuli); (B) Schematic representation of the force-extension traces (upper panel) at each stage of a pulling experiment (lower panel); (C) A typical force-extension curve obtained for TTR annular oligomers showing a saw-tooth pattern where each force transition was fitted (dashed lines) to the WLC model from which the contour length values (LC) were obtained using a persistence length of 0.4 nm.

Conclusions

Force spectroscopy has been previously applied to describe molecular properties of single protein molecules (5). Analysis of the manipulation of annular oligomers showed that despite their condensed state we were able to obtain results that fit the unfolding trajectories of single molecule. Thus, these results suggest that force spectroscopy of annular oligomers can be used to obtain relevant structural information of the TTR monomers within an amyloid intermediate assembly state.

References

1. CHITI, F., and DOBSON, C. M. Protein misfolding, functional amyloid, and human disease. *Annu Rev Biochem* **75**, 333-366. 2006.

2. KODALI, R., and WETZEL, R. Polymorphism in the intermediates and products of amyloid assembly. *Curr Opin Struct Biol* **17**, 48-57. 2007.

3. CAUGHEY, B., and LANSBURY, P. T. Protofibrils, pores, fibrils, and neurodegeneration: separating the responsible protein aggregates from the innocent bystanders. *Annu Rev Neurosci* **26**, 267-298. 2003.

4. LASHUEL, H. A., and LANSBURY, P. T., JR. Are amyloid diseases caused by protein aggregates that mimic bacterial pore-forming toxins? *Q Rev Biophys* **39**, 167-201. 2006.

5. KELLERMAYER, M. S. Visualizing and manipulating individual protein molecules. *Physiol Meas* **26**, R119-153. 2005.

6. WESTERMARK, P., SLETTEN, K., JOHANSSON, B., and CORNWELL, G. G., 3RD. Fibril in senile systemic amyloidosis is derived from normal transthyretin. *Proc Natl Acad Sci U S A* **87**, 2843-2845. 1990.

7. SARAIVA, M. J. Transthyretin mutations in health and disease. *Hum Mutat* **5**, 191-196. 1995.

8. PIRES, R. H., SARAIVA, M. J., DAMAS, A. M., and KELLERMAYER, M. S. Structure and assembly-disassembly properties of wild-type transthyretin amyloid protofibrils observed with atomic force microscopy. *J Mol Recognit* **24**, 467-476. 2011.

Citrullin-containing peptides as B-cell epitopes

Sármay G.[1], Szarka E.[1], Huber K.[1], Pozsgay J.[1], Szili D.[1], Babos F.[2], Nagy Gy.[3], Rojkovich B.[3], Magyar A.[2], Hudecz F.[2]

[1] Department of Immunology, Eötvös Loránd University, Pázmány Péter sétány 1/c, 1117 Budapest, Hungary, [2] HAS-ELTE, Research Group of Peptide Chemistry at Eötvös Loránd University, Pázmány Péter sétány 1/a, 1117 Budapest, Hungary, [3] Buda Hospital of Hospitaller Brothers of St. John, Árpád fejedelem útja 7. 1023 Budapest, Hungary.

Summary

Rheumatoid arthritis (RA) is a chronic, systemic autoimmune disease, characterized by inflammatory polyarthritis. Anti-citrullinated protein antibodies (ACPA) are sensitive and specific markers for diagnosis and prognosis of RA. Citrulline and arginine containing filaggrin, collagen and vimentin peptides were investigated. The citrullin containing peptides were specifically recognized by ACPAs of subgroups of RA patients. We identified a five-mer minimal epitope of a 19-mer filaggrin peptide that were recognized by RA sera with a sensitivity and specificity comparable with the currently used tests. B-cells from RA patients activated by TLR9 and BAFF produced antibodies specific for the 5-mer epitope of citrullinated filaggrin, while B-cells from healthy individuals did not.

Introduction

Rheumatoid arthritis (RA) affects more than 1% of the world population. RA is characterized by an inflammation of synovial joints, which often leads to progressive joint destruction and disability. Recently, antibodies against citrullinated proteins/peptides (ACPA/anti-CCP) are considered as highly specific markers for RA (94-99%), however, only about 70 % of RA patients are positive. ACPAs recognize proteins or peptides with arginine residues converted to citrulline by a posttranslational modification induced by peptidyl arginin deiminase (PAD) [1, 2]. The post-translational changes in self-peptides induce a modulation in the protein conformation, resulting in an altered peptide presentation and the consequent activation of T- and B-cells [3]. Citrullinated proteins and ACPAs form immune complexes that have an important role in the pathogenesis of RA [4]. Here, we compared synthetic peptides corresponding to selected citrullin containing sequences of filaggrin, type II collagen and vimentin. Our aim was to develop new tools for the detection of ACPAs and ACPA producing B-cells of RA patients.

Filaggrin (5-mer)	native	^{311}TRGRS^{315}
	citrullin containing	<u>TX̲GRS</u>, <u>TRGX̲S</u>, <u>TX̲GX̲S</u>
Filaggrin (19-mer)	native	^{311}SHQESTRGRSRGRSGRSGS^{326}
	citrullin containing	SHQESTX̲GX̲SX̲GRSGRSGS
Vimentin	native	^{65}SAVRARSSVPGVRK^{77}
	citrullin containing	SAVRAX̲SSVPGVRK
Collagen	native	^{359}ARGLTGRPGDAK^{369}
	citrullin containing	<u>AX̲GLTGX̲PGDAK</u>

Table 1. Sequences of synthetic peptides

Materials and methods

Patients. Sera samples from RA or SLE patients and age matched controls were collected. The diagnosis of the disease was established on the basis of the revised diagnostic criteria for classification of rheumatoid arthritis, suggested in 1987 by the American Association for Rheumatism.

Peptide synthesis. First, we used conventional solid-phase peptide synthesis, carried out on „MULTIPIN NCP" non-cleavable kit (Mimotopes, Australia). Citrullin containing peptides and the unmodified counterparts containing arginine were synthesized on the pins. The N-terminus of the peptides were acylated. Selected peptides were synthesized manually by SPPS, according to Fmoc/^{t}Bu strategy. The C- or N-terminally biotinylated forms were made using biotin, biotinyl-6-amino-hexanoic acid and 4,7,10-trioxa-1,13-tridecanediamino succinic acid linker (Ttds). The crude products were purified by HPLC. The structure of the peptides was proved by ESI mass spectrometry. (Table 1).

ELISA. ACPA binding to peptides-on-pins were detected by an indirect ELISA using 1:1000 sera dilutions. Alternatively, NeutrAvidin pre-coated plates were loaded with the biotinylated peptides, and sera samples were applied at 1:100 dilutions. The reaction was developed by anti-human IgG-HRP. OD ratios of citrullin-containing/native peptides were plotted, RA and control groups were compared by one-way ANOVA.

In vitro antibody production. B-cells were separated by negative selection using RosetteSep kit (StemCell Technologies) and cultured for 7 days with CpG oligonucleotides and B-cell activating factor of TNF family (BAFF). TXGRS peptide-specific IgG was measured from the culture supernatants by ELISA.
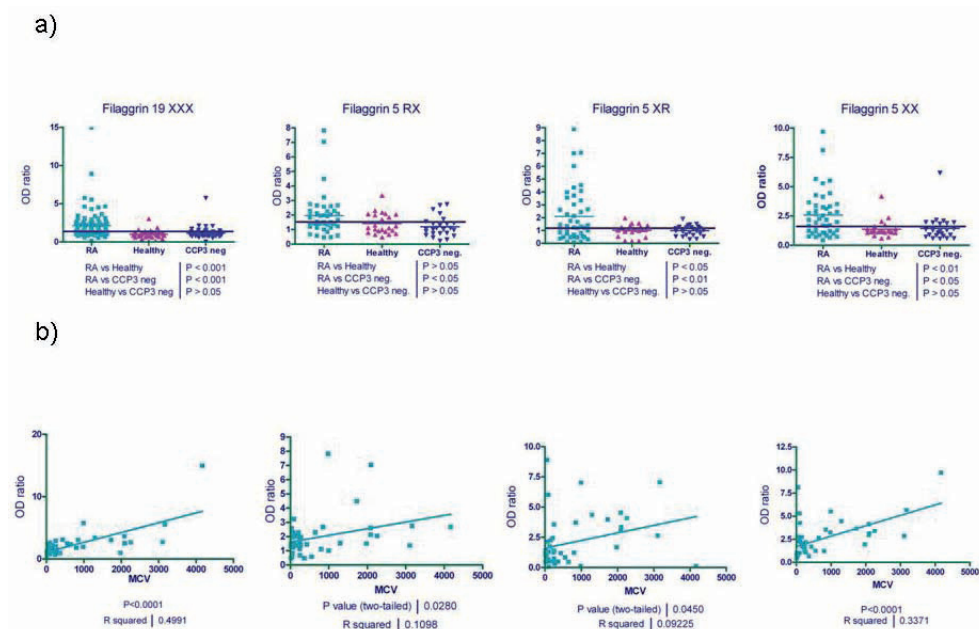
Figure 1: Multipin ELISA a, recognition of 19-mer and 5-mer filaggrin peptides by sera of RA, SLE patients and healthy donors. b, Pearson correlation between peptides' data and MCV titers.

Results

Identification of the minimal epitope of triple citrullinated filaggrin peptide.

To determine the optimal number and position of citrullin for ACPA detection the peptides were synthesized on MultiPin NCP kit. The advantage of the kit is that the same kit can be applied several times (more than 50) after regeneration. The 19-mer filaggrin peptide, containing 3 citrullins was recognized by significantly higher number of RA (CCP3 positive) sera, as compared to CCP3 negative SLE sera or sera of normal blood donors. Next, three 5mer filaggrin peptides containing one or two citrullins were compared. All three 5-mers were recognized by a number of RA sera, but depending on the position of citrullin the difference between RA and non-RA groups varied, indicating the importance of the position of citrullin in the recognition (Fig. 1a). We have found a positive correlation between MCV titers and the OD index values of the 19-mer, the 5-mer TXGXS and TXGRS peptide (X=citrullin) (Fig.1). The latter 5-mer peptide was chosen for further experiments.

Optimalization of the linker for biotinylation

The 5-mer peptide TXGRS was resynthesized by SPPS and biotinylated at either the N or C terminal end using short or long chain biotin (biotin-6-amino-hexanoic acid). Exclusively the C terminally biotinylated peptides were recognized by RA sera. Furthermore, we also used a longer linker between the peptide and the biotin, such as Ttds [5], but that did not increase significantly the recognition of the peptides (Fig.2).
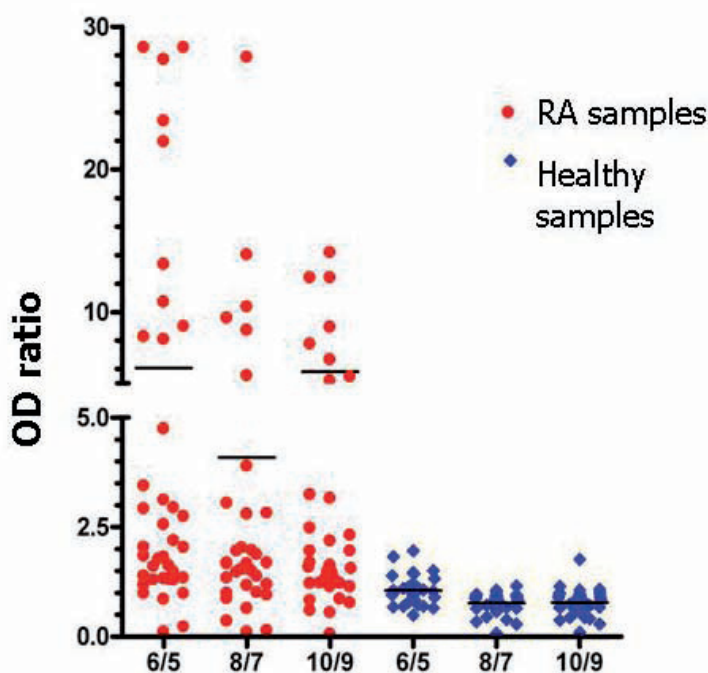
Figure 2: Linker optimalization of 5-mer biotinylated TXGRS filaggrin peptides. 6/5 contains long-chain biotin, 8/7 contains Ttds-biotin and 10/9 have Ttds-long-chain biotin on the N-terminus. Even numbers stand for citrullin, odd numbers for arginin containing peptides.

Comparison of citrullin containing filaggrin, vimentin and collagen (CII)peptides.

Reactivities of sera with C-terminally biotinylated peptides of filaggrin, and N-terminally biotinylated peptides of type II collagen and vimentin were compared. The CII peptide was a linear version of the previously described arthritis-related triple helical peptide of collagen, CI[III] [6], the vimentin peptide was described earlier by Hill et al. [7]. 113 sera from RA patients 18 sera from SLE patients and 97 sera from age-matched control individuals were tested. As compared to the controls, all citrullin-containing peptides gave significantly higher reactivity with sera from the RA group. At 95 % specificity the sensitivity values were 34.5 %, 49 %, 48.3 %, 55.2 %, 27.2 % and 42.2%, for the TXGRS-K(biotin-6-amino-hexanoyl), TXGRS-K(Ttds-biotin), SHQESTXGXSXGRSGRSG S-K(Ttds-biotin-6-amino-hexanoyl), SHQESTXGXSXGRSGRSGS-K -(biotin-6-amino-hexanoyl) (data not shown for the 19-mer peptides), (biotin-6-amino-hexanoyl)-collagen359-369 and (biotin-6-amino-hexanoyl)-vimentin65-77 peptides, respectively (Fig. 3-4). All peptides were recognized by sera of RA patients with high specificity, while the sensitivity values varied. The data also indicate that certain groups of patients recognize only one or two peptides, while some patients recognized them all. Current works are in progress to differentiate between these groups.
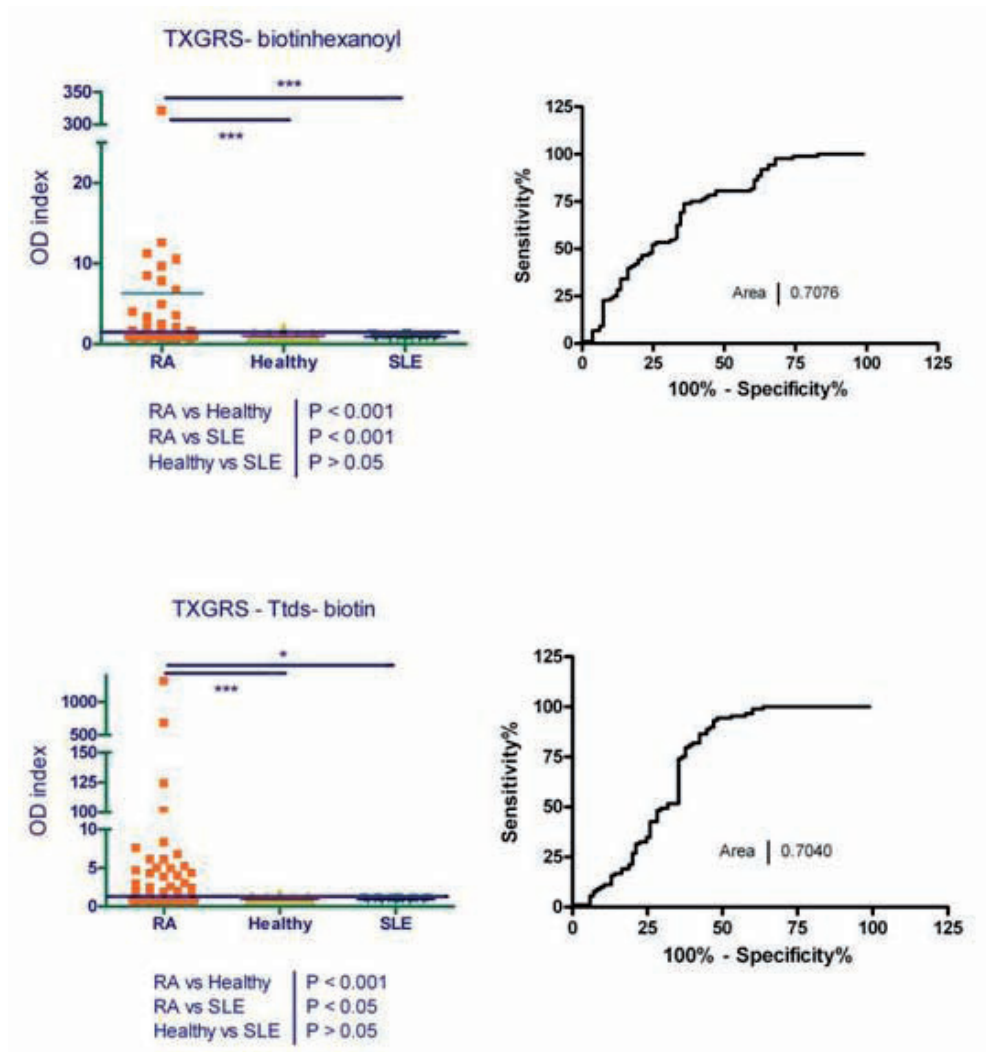
Figure 3: Recognition of TXGRS filaggrin peptides by sera of the RA, SLE and healthy groups (left panels). ROC curves for these peptides were determined (right panels).

Anti-TXGRS filaggrin peptide-specific antibody production in vitro.

    In order to see whether innate signals may force B-cells from RA patients to produce peptide-specific antibodies, purified B-cells were cultured with CpG oligo-nucleotide, a TLR9 agonist in the presence of BAFF. RA B-cells synthesized some TXGRS peptide-specific IgG *in vitro* even in control samples, and the amounts of these antibodies significantly increased due to the CpG+BAFF treatment. B cells from healthy controls failed produce citrullinated peptide specific antibodies (Fig. 5).
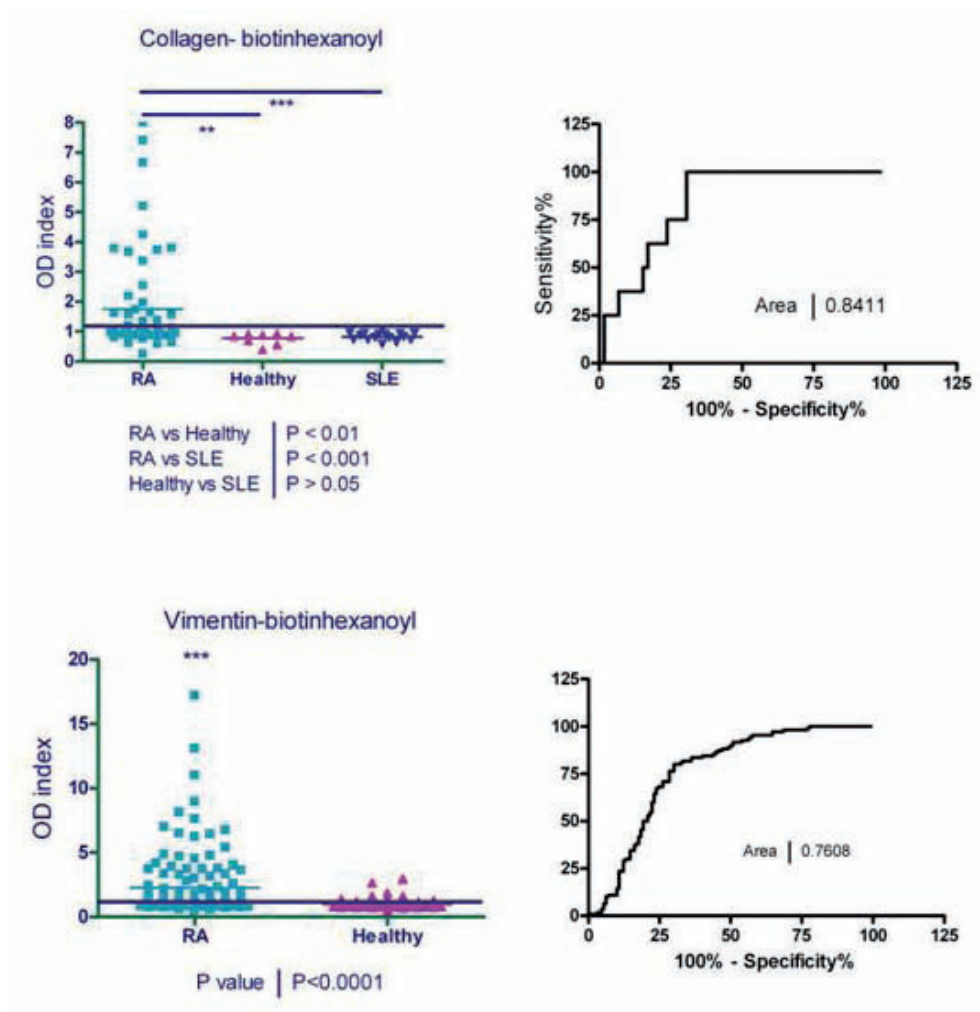
Figure 4: Recognition of N-terminally biotinylated collagen and vimentin peptides.

Discussion

Until now filaggrin, Type II collagen (CII), α-enolase, fibrinogen and vimentin are the best known auto-antigens that undergo citrullination and trigger ACPA production in subgroups of RA patients [3, 8-10]. Pro-filaggrin has not been found in the joints of RA patients, while CII, α-enolase, fibrin(ogen) and vimentin, are present in the inflamed synovium in large amount [11, 12]. However, anti-filaggrin reactivity were shown to co-localize with anti-citrulline reactivity in the synovium [13]. The first test that become available to detect ACPA was based on a synthetic citrullin containing peptide derived from filaggrin (CCP1) [14]. More recently, other ELISA tests using second- and third-generation citrullin containing peptides (CCP2, CCP3) [15, 16] or
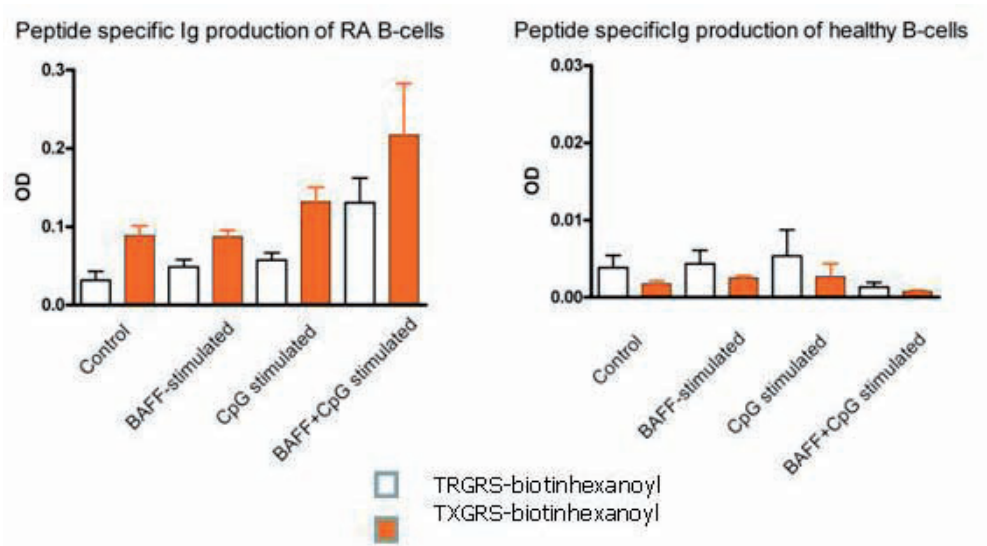
Figure 5: Citrullin containing filaggrin peptide specific IgG secretion of B-cells isolated from blood of RA patients (n=5).

mutated citrullinated vimentin (MCV) [17], with useful diagnostic and prognostic properties have been developed. However, reactivity of RA sera with single, citrullin containing epitopes was not compared. The aim of the present study was to evaluate the diagnostic yield of several citrullin containing peptides by ELISA, and to compare their sensitivity and specificity in a cohort of patients with RA. First, we identified the minimal epitope of citrullinated filaggrin, as a 5-mer peptide, TXGRS. Since ACPA recognizing citrullinated filaggrin is suggested to cross-react with several other citrullinated proteins [13], it is not surprising that we found a significant positive correlation between anti-MCV tests and the recognition of both the 19-mer and the 5-mer citrullin containing epitopes.

The TXGRS peptide was also recognized by antibodies produced *in vitro* after the stimulation of RA B-cells with CpG, the TLR9 agonist. These data suggest that peptide-specific memory B-cells may exist in the blood of RA patients that can be triggered to develop into autoantibody producing plasma cells. This might occur *in vivo* after bacterial infection.

The second epitope we have tested corresponds to a sequence in collagen type II (CII), a part of the previously described, conformation-dependent arthritis-related epitope of CII [9]. Here we show that the monomeric form of this citrullin containing collagen peptide is also specifically recognized by some RA sera, although the sensitivity of this test is lower as compared to all other peptides. The vimentin65-77 peptide was described as a T-cell epitope with a predicted binding to the HLA DRB1*0401, shared epitope in RA [7]. This peptide-MHC interaction, and subsequent Th activation was suggested to be responsible for driving autoantibody production against vimentin. Here we have shown that the same peptide is indeed specificaly-

ly recognized by sera of RA patients, although with somewhat lower sensitivity as compared to commercial tests.

Taking all together, we suggest that our data are important for emerging diagnostic tests that would allow to identify subgroups of RA patients and to develop individual therapies.

References

1. Yamada, R., Suzuki, A., Chang, X., and Yamamoto, K. Peptidylarginine deiminase type 4: identification of a rheumatoid arthritis-susceptible gene. Trends Mol Med *9*, 503-508, 2003.

2. Yamada, R., Suzuki, A., Chang, X., and Yamamoto, K. (2005). Citrullinated proteins in rheumatoid arthritis. Front Biosci *10*, 54-64.

3. Steiner, G. Auto-antibodies and autoreactive T-cells in rheumatoid arthritis: pathogenetic players and diagnostic tools. Clin Rev Allergy Immunol *32*, 23-36, 2007.

4. Klareskog, L., Malmstrom, V., Lundberg, K., Padyukov, L., and Alfredsson, L. Smoking, citrullination and genetic variability in the immunopathogenesis of rheumatoid arthritis. Semin Immunol *23*, 92-98, 2011.

5. Bartos, A., Uray, K., and Hudecz, F. New biotin derivatives for labeling and solubilizing IgG peptides. Biopolymers *92*, 110-115, 2009.

6. Burkhardt, H., Koller, T., Engstrom, A., Nandakumar, K.S., Turnay, J., Kraetsch, H.G., Kalden, J.R., and Holmdahl, R. Epitope-specific recognition of type II collagen by rheumatoid arthritis antibodies is shared with recognition by antibodies that are arthritogenic in collagen-induced arthritis in the mouse. Arthritis Rheum *46*, 2339-2348, 2002.

7. Hill, J.A., Southwood, S., Sette, A., Jevnikar, A.M., Bell, D.A., and Cairns, E. Cutting edge: the conversion of arginine to citrulline allows for a high-affinity peptide interaction with the rheumatoid arthritis-associated HLA-DRB1*0401 MHC class II molecule. J Immunol *171*, 538-541, 2003.

8. Bang, H., Egerer, K., Gauliard, A., Luthke, K., Rudolph, P.E., Fredenhagen, G., Berg, W., Feist, E., and Burmester, G.R. Mutation and citrullination modifies vimentin to a novel autoantigen for rheumatoid arthritis. Arthritis Rheum *56*, 2503-2511, 2007.

9. Burkhardt, H., Sehnert, B., Bockermann, R., Engstrom, A., Kalden, J.R., and Holmdahl, R. Humoral immune response to citrullinated collagen type II determinants in early rheumatoid arthritis. Eur J Immunol *35*, 1643-1652, 2005.

10. Sebbag, M., Moinard, N., Auger, I., Clavel, C., Arnaud, J., Nogueira, L., Roudier, J., and Serre, G. Epitopes of human fibrin recognized by the rheumatoid arthritis-specific autoantibodies to citrullinated proteins. Eur J Immunol *36*, 2250-2263, 2006.

11. Matsuo, K., Xiang, Y., Nakamura, H., Masuko, K., Yudoh, K., Noyori, K., Nishioka, K., Saito, T., and Kato, T. Identification of novel citrullinated autoantigens of synovium in rheumatoid arthritis using a proteomic approach. Arthritis Res Ther *8*, R175, 2006.

12. Tilleman, K., Van Steendam, K., Cantaert, T., De Keyser, F., Elewaut, D., and Deforce, D. Synovial detection and autoantibody reactivity of processed citrullinated isoforms of vimentin in inflammatory arthritides. Rheumatology (Oxford) *47*, 597-604, 2008.

13. Baeten, D., Peene, I., Union, A., Meheus, L., Sebbag, M., Serre, G., Veys, E.M., and De Keyser, F. Specific presence of intracellular citrullinated proteins in rheumatoid arthritis synovium: relevance to antifilaggrin autoantibodies. Arthritis Rheum *44*, 2255-2262, 2001.

14. Avouac, J., Gossec, L., and Dougados, M. Diagnostic and predictive value of anti-cyclic citrullinated protein antibodies in rheumatoid arthritis: a systematic literature review. Ann Rheum Dis *65*, 845-851, 2006.

15. Grootenboer-Mignot, S., Nicaise-Roland, P., Delaunay, C., Meyer, O., Chollet-Martin, S., and Labarre, C. Second generation anti-cyclic citrullinated peptide (anti-CCP2) antibodies can replace other anti-filaggrin antibodies and improve rheumatoid arthritis diagnosis. Scand J Rheumatol *33*, 218-220, 2004.

16. Wu, R., Shovman, O., Zhang, Y., Gilburd, B., Zandman-Goddard, G., and Shoenfeld, Y. Increased prevalence of anti-third generation cyclic citrullinated peptide antibodies in patients with rheumatoid arthritis and CREST syndrome. Clin Rev Allergy Immunol *32*, 47-56, 2007 .

17. Besada, E., Nikolaisen, C., and Nossent, H. Diagnostic value of antibodies against mutated citrullinated vimentin for rheumatoid arthritis. Clin Exp Rheumatol *29*, 85-88, 2011.

Food additives or Cosmetic ingredients in Plygonum cuspidatum

Sawabe A., Nakamura T., Fujii Y., Takeda R., and Iida A.

Department of Applied Biological Chemistry, Faculty of Agriculture, Kinki University, 3327-204, Nakamachi, Nara 631-8505, Japan.
E-mail: sawabe@nara.kindai.ac.jp

Summary

Seven compounds were isolated from the leaves of *polygonum cuspidatum*, and their structures were established on basis of MS and NMR spectroscopy. They were 3-*O*-caffeoyl quinic acid (**1**), quercetin 5-*O*-Fucosyl(1→2)-rhamnoside (**2**), (-)-epicatechin (**3**), procyanidin B-2 (**4**), procyanidin C (**5**), procyanidin E (**6**), 3'-trimethoxy procyanidin E (**7**). As a result, remarkable hyaluronidase inhibitory activity was indicated to proanthocyanidin compounds. Subsequently we evaluated isolated compounds for a collagenase inhibitory activity examination and the histamine liberation inhibition test by using human juvenile basophil cell line KU812. In conclusion, it might be used in general as food additives or cosmetics because remarkable antiallergic activity which had moisturizing action was found from the leaves of *Polygonum cuspidatuma*.

Introduction

Today that one person out of about three persons of the nation has some allergic disease is clarified in 2003 by Ministry of Health, Labour and Welfare health welfare trend investigation. In addition, there is allergic symptomatic number of patients in an increase tendency in future. Especially, there is the most type I allergic number of patients such as pollinosis and atopic dermatitis. As for treatments of an allergic disease, complete recovery is difficult, and it tend to need a long period. From such a background, diet therapy to improve a symptom by taking food with a few side effects every day is expected.

In this study, we report a hyaluronidase inhibitory activity examination [1], a collagenase inhibitory activity examination [2], and the histamine liberation inhibition test by using human basophil cell line KU812 [3] as an index of antiallergic effect. Remarkable activity was found in the leaves of *Polygonum cuspidatum* extract which was Polygonaceae plant of East Asia when we screened it from several kinds of plant extracts by using a hyaluronidase inhibitory activity examination.
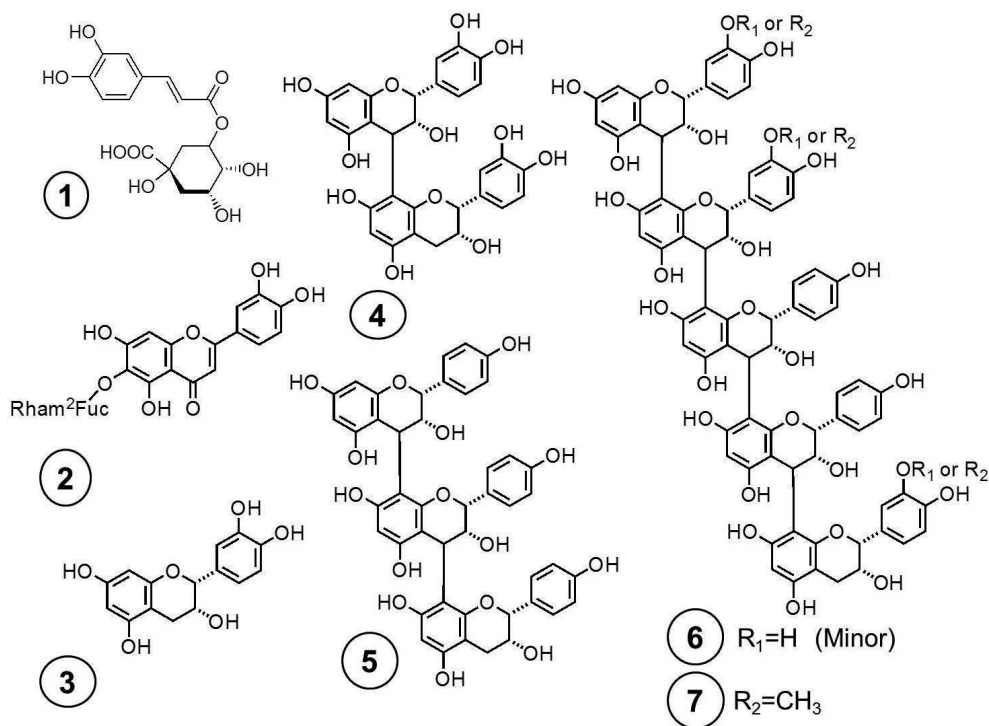
Fig. 1

Materials and Methods

Isolation of Functional Compounds

The leaves (2.2 kg) of *polygonum cuspidatum* were immersed in 70% ethanol a week, and ethanol extracts were obtained by filtration and vacuum concentration. The ethanol extracts were extracted with hexane, then with 1-butanol. The following 7 compounds were isolated and purified by repeated silica gel chromatography and gel filtration; **1** (48 mg), **2** (28 mg), **3** (30 mg), **4** (143 mg), **5** and **6** (73 mg), and **7** (48 mg) from the 1-butanol extracts (Fig. 1).

Quantity of corneum moisture

The quantity of corneum moisture was measured with SKICON- 200EX (I.B.S Co., Ltd) that measures high frequency conductance of the skin.

Results and Discussion

Remarkable hyaluronidase inhibitory activity was indicated to proanthocyanidin compounds (Fig. 2). Subsequently we evaluated isolated compounds for a collagenase
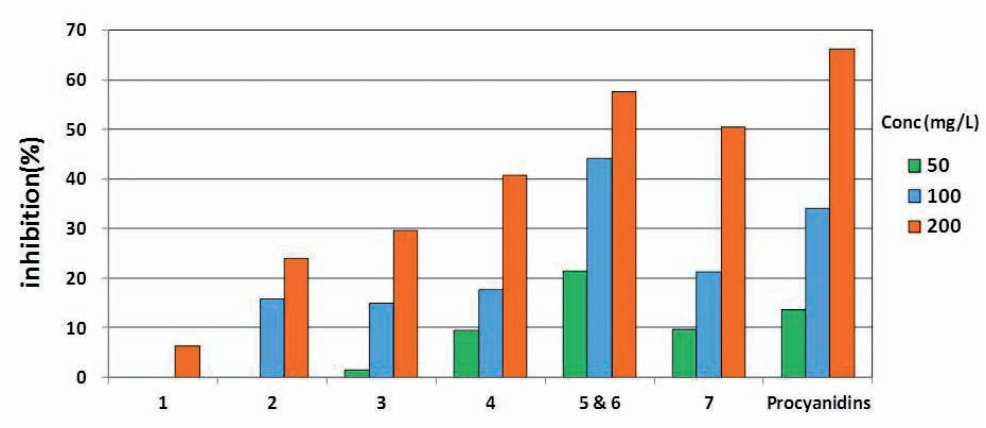
Fig. 2

Compound	Hyaluronidase inhibitory activity IC_{50} (μM)	Collagenase inhibitory activity IC_{50} (μM)	Histamine liberation inhibition (%)
1	565	115	97
2	325	180	-
3	690	543	-
4	346	168	32
5 & 6	205	40	30
7	138	11	-
Mix.	104	10	35

Table 1

inhibitory activity examination and the histamine liberation inhibition test by using human juvenile basophil cell line KU812.

For a collagenase inhibitory activity examination, remarkable inhibitory activity was indicated to proanthocyanidin compounds as well as hyaluronidase inhibitory activity (Table 1). In addition, for histamine liberation inhibition test, weak activity
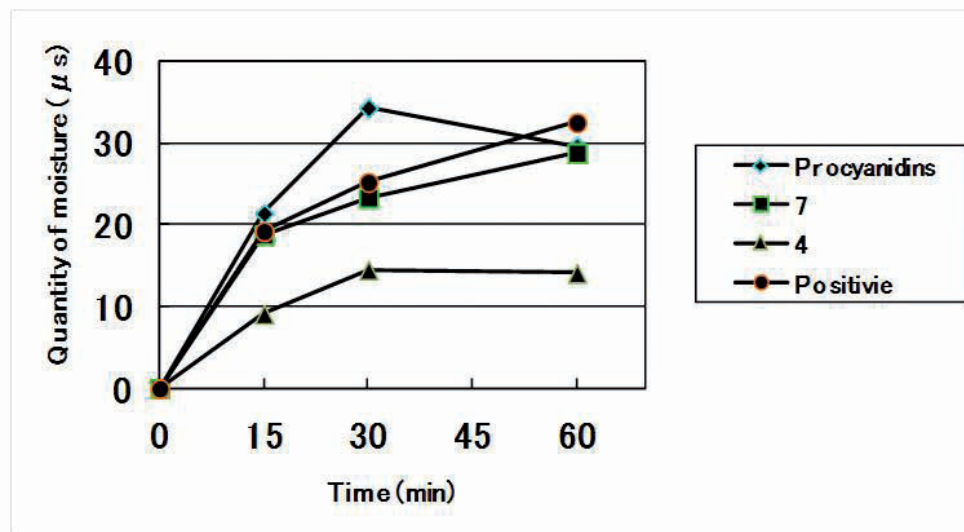
Fig. 3

was indicated to proanthocyanidin compounds. Remarkable inhibitory activity was indicated to compound **1**. Proanthocyanidin compounds showed high moisture retention (Fig. 3).

In conclusion, it might be used in general as food additives or cosmetics because remarkable antiallergic activity was found from the leaves of *Polygonum cuspidatuma*.

References

[1] T. Takahashi, M. Ikegami-Kawai, R. Okuda, K. Suzuki, Analytical Biochemistry, 322, 257-263 (2003).
[2] F. Teramachi, T. Koyano, T. Kowithayakorn, M. Hayashi, K. Komiyama, M. Ishibashi, J Nat Prod. 68, 794-796 (2005).
[3] P. Yamada, H. Isoda, JK. Han, TP. Talorete, Y. Abe, Biosci Biotechnol Biochem., 71, 1294-1305 (2007).

Synthetic Biology and the Minimal Cell Project

Stano P.,[1]* Kuruma Y.,[2] Souza T.,[3] Carrara, P.,[1] Luisi P. L.[1]

1 Biology Department, University of Roma Tre, Rome, Italy; 2 Department of Medical Genome Sciences, The Tokyo University, Tokyo, Japan; 3 Pharmacy Institute, Friedrich Schiller University, Jena, Germany. Correspondence to: stano@uniroma3.it

Summary. Here we will show the recent advancements on the use of lipid vesicles (liposomes) as cell models. Guided by the autopoietic theory, we aim at designing and constructing cell-like compartments by inserting nucleic acids, ribosomes and enzymes inside liposomes. In synthetic biology, these systems are called "minimal" cells.

1. Autopoiesis and minimal life

When we look at modern living cells, like bacteria or mammalian cells, we are puzzled about how their astonishing complexity could have emerged from inanimate matter during the last ~4.5 billion years of chemical and biological evolution. Living cells, however, could not have been so complex from the beginning. We might therefore ask what are the minimal requirements, in terms of functions and structures, in order to have cellular life.

Autopoiesis,[1] a system theory developed by Humberto Maturana and Francisco Varela in the 70s, helps to answer this question. An autopoietic (self-producing) unit is an object in the physical space that can produce its own components thanks to a reaction network inside a compartment. All living systems are autopoietic. We can therefore use the autopoietic theory as a framework for designing minimal living cells.

The first ingredient for constructing an autopoietic system in the lab is a compartment. It has been shown that simple lipid-based compartments, like aqueous micelles, reverse micelles, and – more importantly – lipid vesicles (liposomes), can undergo an autopoietic dynamics by uptaking amphiphiles from the environment, transform them into the boundary-forming compound, then grow in size, and eventually divide after reaching an unstable state (for a review, see [2]). These successful experimental approaches were soon developed in more complex way in order to mimic better the autopoietic scheme, and especially to introduce a reactive molecular network inside these compartments, with the function of synthesizing all components needed for growth.

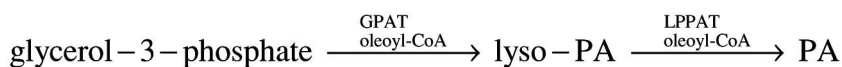Autopoietic minimal cells can be constructed by inserting the minimal number of

enzymes, DNA, RNAs, ribosomes, and other biochemicals into lipid vesicles. In this case, the corresponding constructs are called "semi-synthetic" because done of natural and synthetic molecules. The research on semi-synthetic minimal cells is rapidly growing [3] and below we will comment some cases recently reported by us.

2. Lipid synthesis inside semi-synthetic minimal cells

The most important biochemical network that has been reconstructed inside liposomes is the transcription/translation one, which produce an active protein (enzyme) starting from the corresponding DNA sequence [4]. This is possibly by coupling liposome technology and cell-free systems. Several proteins have been synthesized with this method, and the synthesized proteins showed the proper structures and enzymatic activities.

An attractive target, to be reached by means of this technology, is the synthesis of the enzymes that catalyze the production of lipids. In this way, it is possible to synthesize components of the system by an internal reaction network, as requested by the autopoietic theory.

The target enzymes, glycerol-3-phosphate acyltransferase (GPAT) and lysophosphatidic acid acyltransferase (LPAAT), are known as first two enzymes for biosynthesis of phospholipids. Their presence within a liposome would allow the production – from glycerol-3-phosphate and acyl-CoAs – of phosphatidic acid (PA), which in turn would insert into the liposome membrane and let the liposome grows in size.

$$\text{glycerol} - 3 - \text{phosphate} \xrightarrow[\text{oleoyl-CoA}]{\text{GPAT}} \text{lyso} - \text{PA} \xrightarrow[\text{oleoyl-CoA}]{\text{LPPAT}} \text{PA}$$

The genes encoding for these two proteins (plasmid DNAs) were encapsulated together with the PURE system [5] inside liposomes of a specific lipid composition [6]. The choice of the membrane composition resulted to be the key factor for obtaining functioning enzymes. Quite interestingly, the lipid bilayer acted as primitive chaperon for GPAT, which could increase four-fold its activity when compared to lipid-free conditions. The two enzymes were synthesized together in the same liposomes, but failed to produce phosphatidic acid. This was because crude LPPAT did not fold correctly in the reducing conditions required by the cell-free protein synthesis. Oxidized glutathione restored LPPAT activity, allowing the two-steps (discontinuous) synthesis of PA. Unfortunately, however, the amount of PA was quite low and we did not observe vesicle growth. This study, however, demonstrates for the first time that the intraliposomal production of membrane enzymes, which have integral membrane regions, is indeed possible. Then, semi-synthetic minimal cells can be functionalized by such kind of important cellular components. After optimization, this strategy might bring to the construction of lipid-synthesizing liposomes – one of the key intermediates for observing man-made autopoietic systems.

3. Protein synthesis inside small liposomes and the physics of solute entrapment.

In the above-mentioned study, as well as in work from other group, transcription/

translation kits are generally entrapped within large liposomes (diameter > 1 μm). The reason is that such large compartments have high entrapment yields, i.e., there is a high probability of finding the more than 80 different macromolecular components inside a single liposome. What about small liposomes (diameter ~ 0.1 μm)? Due to their small volume, it is expected a very low entrapment, with a very small expected number of entrapped molecules, e.g. < 1 molecule/vesicle. Notice that in this conditions a Poisson distribution should describe the entrapment events, and consequently the encapsulation probability would decrease quickly in the cases where the entrapment of many molecules is considered.

In a detailed study, we have demonstrated that proteins can be synthesized also in small vesicles, and that this observation implies a deviation from the expected Poisson entrapment statistics [7]. In order to verify this hypothesis, we further investigated the true statistical distribution of solutes like the protein ferritin [8] and ribosomes [9] inside conventional (sub-micron) liposomes. The number of entrapped ferritin (or ribosomes) within each liposomes was determined by direct visual inspection of cryo-transmission electronmicrographs, where individual ferritin and ribosomes are visible as single molecules, and counted accordingly. Quite unexpectedly, we have shown that the encapsulation statistics for the entrapment of these solutes inside liposomes does not follow the expected Poisson distribution, but it is rather shaped as in a power-law. This implies that the existence of solute-superfilled liposomes is not only possible, but it is order of magnitudes more probable than expected. Very high intraliposomal solute concentrations (similar to biological crowding conditions) are spontaneously achieved when lipids and solutes self-organize in a closed compartment, even starting from diluted solutions. It has been argued that such phenomenon might have had a role in origin of primitive cells.

4. Conclusions

In this contribution we have shortly illustrated the most significant studies carried out in our laboratory in the 3 years. More in general, our approach shows that the research on semi-synthetic minimal cells is rapidly growing in complexity and that – in addition to the specific and relevant bioengineering aspects, it allows the discovery of basic physico-chemical processes underlying molecular self-organization.

References.

1. VARELA FJ, MATURANA HR, URIBE RB. Autopoiesis: the organization of living systems, its characterization and a model. BioSystems 5, 187-196, 1974.
2. STANO P, LUISI PL. Achievements and open questions in the self-reproduction of vesicles and synthetic minimal cells. ChemComm 46, 3639-3653, 2010.
3. LUISI PL, FERRI F, STANO P. Approaches to semi-synthetic minimal cells: a review. Naturwissenschaften 93, 1-13, 2006.
4. STANO P, CARRARA P, KURUMA Y, SOUZA T, LUISI PL. Compartmentalized reactions as a case of soft-matter biotechnology: synthesis of proteins and nucleic acids inside lipid vesicles. J. Mat. Chem. DOI: 10.1039/c1jm12298c.
5. SHIMIZU Y, INOUE A, TOMARI Y, SUZUKI T, YOKOGAWA T, NISHIKAWA K,

UEDA T. Cell-free translation reconstituted with purified components. Nat. Biotech. 19, 751-755, 2001.

6. KURUMA Y, STANO P, UEDA T, LUISI PL. A synthetic biology approach to the construction of membrane proteins in semi-synthetic minimal cells. Biochim. Biophys. Acta 1788, 567-574, 2009.

7. SOUZA T, STANO P, LUISI PL. The minimal size of liposome-based model cells brings about a remarkably enhanced entrapment and protein synthesis. ChemBioChem 10, 1056-1063, 2009

8. LUISI PL, ALLEGRETTI M, SOUZA T, STEINEGER F, FAHR A, STANO P. Spontaneous protein crowding in liposomes: A new vista for the origin of cellular metabolism. ChemBiochem 11, 1989-1992, 2010.

9. SOUZA T, STEINIGER F, STANO P, FAHR A, LUISI PL. Spontaneous crowding of ribosomes and proteins inside vesicles: A possible mechanism for the origin of cell metabolism. ChemBioChem. DOI: 10.1002/cbic.201100306.

Differential effects of ligand binding on protein dynamics

Wieninger SA[a], Serpersu EH[b], Ullmann GM[a]

[a] *Structural Biology/Bioinformatics, University of Bayreuth, Universitätsstr. 30, BGI, 95447 Bayreuth, Germany*
[b] *Department of Biochemistry and Cellular and Molecular Biology, The University of Tennessee, Knoxville, TN 37996, USA*

Summary

The enzyme aminoglycoside phosphotransferase (3')-IIIa (APH) confers resistance against a broad range of aminoglycoside antibiotics. We use the Gaussian Network Model, a coarse-graining method, to investigate how the binding of nucleotide and antibiotic influences the dynamics and thereby the ligand binding properties of APH.

Introduction

APH catalyzes ATP-dependent phosphorylation of more than ten different aminoglycoside antibiotics, whereby the antibiotic's affinity for the ribosome is decreased. The crystal structure of APH is solved in its apo form, in complex with nucleotide,[1] and in complex with nucleotide and kanamycin A or neomycin B.[2] Interestingly, in NMR experiments, the dynamics differs significantly in the various APH complexes,[3] although the crystallographic studies indicate that no larger conformational changes occur upon ligand binding. A complete exchange of backbone amides is observed within 15h of exposure to D_2O in the apo form. While antibiotic binding leads to significant stabilization, nucleotide binding to the APH-aminoglycoside complex decreases the protection and renders several amides of β-sheet residues exchangeable.

Materials and Methods

A Gaussian Network Model[4] was applied. The nodes of the elastic network are grouped into dynamic domains based on the correlations of fluctuations. Details are described elsewhere.[5]
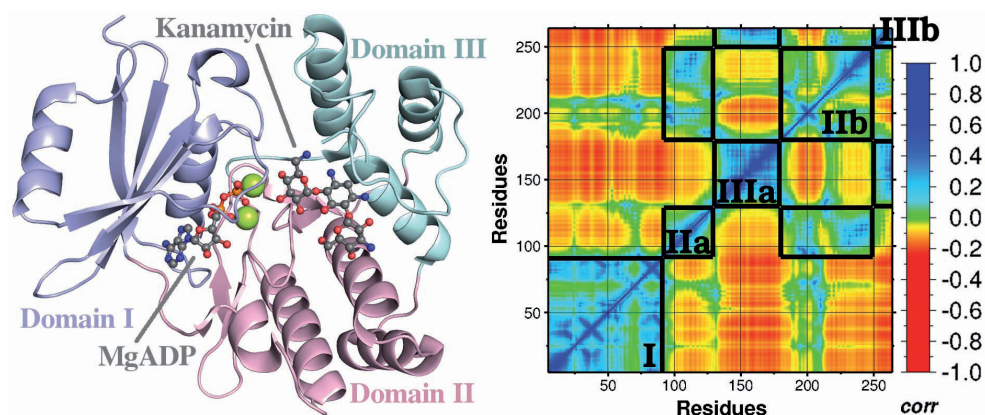
Figure 1: Definition of three dynamic domains of APH based on correlations of residue fluctuations. The residues of one domain are positively correlated to each other, while they are anticorrelated to residues of the other domains. MgATP binds between domains I and II, the antibiotic binds between domains II and III.
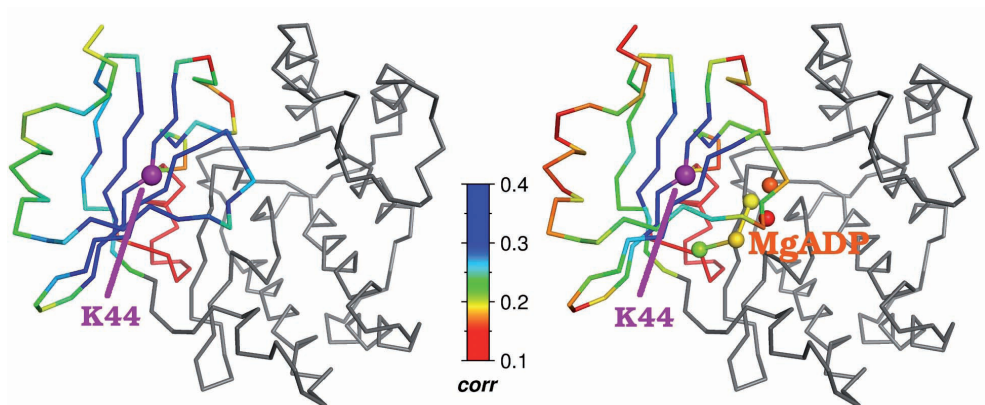

Figure 2: Correlations of nodes of domain I to the node representing K44. The correlations are higher in the absence of nucleotide (left side).

Results

Based on the correlations of fluctuations of apo- APH, three dynamic protein domains are identified (Figure 1). Ligand binding between the dynamic domains reduces the correlation within the domains (Figure 2) and reduces the flexibilities of residue nodes which are located near the ligand.

Conclusions

Stabilization of APH due to antibiotic binding can be explained by reduced residue

flexibilities upon ligand binding. But the surprising destabilization of β-sheet residues upon nucleotide binding shows that not only the number of closest neighbors, but the overall protein architecture is important for the dynamical properties. Nucleotide binding disturbs the rigid-body movement of domain I, manifested by reduced correlations, and weakens hydrogen bonds between the strands of the β-sheet. The differential effects of antibiotic and nucleotide binding on dynamics arise from structural differences between the binding domains I and III. While the antibiotic binding loop of domain III is very flexible and can be stabilized by additional connections to the ligand, the β-sheet of domain I underlies many constraints even in the absence of ligand. Nucleotide binding leads to frustration. The arrangement of the protein into three anticorrelated dynamic domains with different rigidities allows for the tuning of APH dynamics upon ligand binding, which is a key factor in explaining the substrate promiscuity of the enzyme.

Acknowledgements

References

1   BURK DL, HON WC, LEUNG AK, BERGHUIS AM, Structural analyses of nucleotide binding to an aminoglycoside phosphotransferase, Biochemistry, 40, 8756-8764, 2001.

2   FONG DH, BERGHUIS AM, Substrate promiscuity of an aminoglycoside antibiotic resistance enzyme via target mimicry, Embo J., 21, 2323-2331, 2002.

3   NORRIS A, SERPERSU EH, NMR detected hydrogen-deuterium exchange reveals differential dynamics of antibiotic- and nucleotide-bound aminoglycoside phosphotransferase(3')-IIIa, J. Am. Chem. Soc., 131, 8587-8594, 2009.

4   BAHAR I, ATILGAN AR, ERMANN B, Direct evaluation of thermal fluctuations in proteins using a single-parameter harmonic potential, Fold. Des., 2, 173-181, 1997.

5   WIENINGER SA, SERPERSU EH, ULLMANN GM, ATP binding enables broad antibiotic selectivity of aminoglycoside phosphotransferase (3')-IIIa - an elastic network analysis, J. Mol. Biol., 409, 450-465, 2011.

The turn of the light-harvesting chlorophyll a/b complexes of photosystem II (LHCIIb) between the BC loop and helix C has important structural significance

Liu Cheng and Yang Chunhong*

Key Laboratory of Photobiology, Institute of Botany, Chinese Academy of Sciences, Beijing, China
*Corresponding author:
Chunhong Yang
Key laboratory of photobiology, Institute of botany
Chinese Academy of Sciences
Nanxincun road 20, 100093 Beijing, China
Tel: +86-10-62836252
fax: +86-10-62836219
E-mail: yangch@ibcas.ac.cn

Summary: Terrestrial plants grow in an environment full of variations in temperature and light intensity. In order to cope with the changing temperature and light intensity, plants have developed mechanisms for the adaptation to high temperature and excessive light conditions, among which one of the most important features is the structural flexibility of the pigment-protein supercomplexes. The major light-harvesting chlorophyll (Chl) *a/b* protein of photosystem II (PSII) (LHCIIb), because of its important role in energy balance in photosynthetic apparatus, is the most important pigment-protein complex for the adaptation to the changing external environments. In order to study the structural basis regulating the supermolecular organization of LHCIIb, especially the lumenal region, mutational studies to the amino acids, Ser123 and Ile 124, located in the turn between the BC loop and the helix C of LHCIIb, have been executed. It is concluded that the turn between the BC loop and the helix C plays important roles in determining the structural stability and inter-molecular interaction properties of LHCIIb.

Introduction: The major light-harvesting chlorophyll (Chl) *a/b* complexes of the plant photosystem II (LHCIIb) is a multi-functional pigment-protein complex. Besides harvesting solar energy and delivering the energy for the charge separation, LHCIIb can quickly switch to a quenched-state that starts a non-photochemical quenching (NPQ) process so that the harmful overexcited energy is dissipated to heat under excessive light conditions (1). Reversible change of the supermolecular organizations of LHCIIb is one of the molecular mechanisms switching between quenched- and

unquenched-state in response to the altered energy balance in thylakoid membranes (2). Although the significance of the LHCIIb aggregate formation in NPQ has long been in the focus of the research interest (3), the structural basis for regulating the reversible supermolecular organizational change of LHCIIb remains a myth. Understanding the molecular mechanisms regulating the supermolecular organization of LHCIIb is a basic scientific goal that may eventually have significant impacts on material science in future because LHCIIb is a potential material for harnessing solar energy.

The basic functional structure of LHCIIb is a trimer which is composed of homo- or hetero- monomers (4). It has been proposed that the trimeric LHCIIb in thylakoid membrane undergoes flexible supermolecular organizational changes, e.g. the trimer-monomer, or trimer-aggregation transitions, during regulatory processes such as state transition (5) and NPQ (2). As revealed by the near atomic structural resolutions (6,7), each monomeric LHCIIb contains three transmembrane (TM) α-helices (Helix A, B, C), one amphiphilic α-helix (Helix D) and an amphipathic short 3_{10}-helix (Helix E) at the lumenal side and coordinates, as cofactors, 8 Chl *a*, 6 Chl *b*, 2 Lutein (Lut), 1 xanthothyll pigment, and 1 neoxanthin (Neo) (6,7). It has been shown, *via* detailed spectroscopic analysis and biochemical analysis, that the properties of the *in vitro* recombinant pigment-protein complexes of LHCIIb are similar to the native complexes (8-10). This characteristic has laid the foundation for studies of the structural and functional roles of individual amino acid or a particular motif of the protein. It is proposed that the lumenal region between TM B and C of LHCIIb also serves as a functional switch regulating structure and function of LHCIIb (11,12). The mutational analysis to the same lumenal loop reveals its important roles in adjusting the pigment conformation and the energy transfer efficiency under different environmental conditions (12,13). The aim of the work is to study the role of the turn between the BC loop and the helix C of LHCIIb in regulating the structural stability and supermolecular organization of LHCIIb. For this purpose, the two amino acids, Ser 123 and Ile 124, have been exchanged to Gly and Leu, and the spectroscopic and biochemical charac-terization of the mutants have been studied. The results revealed that the mutagenesis in the region results in different consequences on the conformations of the bound pigments, which in turn, leads to altered properties in supermolecular organization.

Methods and Material: (1) *Preparation of recombinant LHCIIb:* The construct overexpressing pea Lhcb1 was obtained as described in (12). The mutagenesis of Lhcb1 was carried out with MutanBEST site-directed mutagenesis Kit (Takara Inc, Japan) *In vitro* reconstitution of trimeric LHCIIb were performed as described (12). The recombinant pigment-protein complexes were purified using sucrose density gradient ultracentrifugation with the same method in (12). (2) *Pigment stoichiometries:* The band corresponding to the trimers in the sucrose density gradient after the ultracen-trifugation were further analyzed for pigment stoichiometries by HPLC as described in (12). Pigments were quantified by comparing integrated peak areas to calibrated ones of known pigment amounts. (3) *Steady-state spectroscopy:* Absorption spectra were obtained using an Shimadzu UV-VIS 2550 spectrophotometer at room tempe-rature (scan rate 100 nm/second, bandwidth 1 nm and step 0.2 nm). Fluorescence emission spectra were obtained at 77K by using a Hitachi F-4500 spectrofluorometer (scan rate 100 nm/minute, bandwidth 5 nm and step 0.5 nm). Circular dichroism (CD) spectra were recorded on a Jasco 815 spectropolarimeter (scan rate 100 nm/minute, bandwidth 1 nm and step 0.5 nm). The measurements were repeated for three

LHCIIb	Chl *a*	Chl *b*	Lut	Neo
WT	7.61±0.42	7.20±0.31	2	0.98±0.03
S123G	7.59±0.12	6.65±0.11	2	0.79±0.02
I124L	7.66±0.21	7.02±0.14	2	0.99±0.01

All values are given as the average of 3-5 individual measurements ± standard deviation.

TABLE 1: Pigment composition of recombinant LHC II complexes. The pigment contents of the complexes from the sucrose density gradient were determined with HPLC. The values are normalized, assuming each LHCIIb monomer binds two Luts.

times and averaged. (4) *Thermal Stability and photostability analysis:* The structural stabilities of reconstituted LHCIIb were measured, as described in (12). The thermal stability was measured by observing the decrease in the extent of energy transfer from complex bound Chl *b* to Chl *a* upon gradual dissociation of the complexes at 37°C. The photostability was measured by observing the decrease in the absorbance at Q_y region by constant illumination with cold white light (4000 µmol m^{-2} s^{-1}).

Results and Discussion: Exchanging the two amino acids S123 and I124 in the edge of the helix C to Gly and Leu, respectively, did not abort the property of the protein binding photosynthetic pigments and yielding stable monomeric and trimeric pigment-protein complexes (PAGE, data not shown). The mobility of the mutant complexes was similar as that of the wild type (WT) LHCIIb. The pigment stoichiometry of the WT and the mutant LHCIIb were calculated based on the pigment/ (2 Luts) ratio, assuming each LHCIIb monomer binds two Luts. It is clearly to see from Table 1 that S123G bound less Chl *b* (0.55) and Neo (0.19), compared to the pigment stoichiometry of WT, which was not the case by I124L. The later showed similar pigment stoichiometry as the WT LHCIIb.

Circular dichroism (CD) in the visible range reflects the dipole-dipole interactions of the chromophores in LHCIIb, which is a powerful tool to study the conformational organization of the LHCIIb. **Figure 1** shows the CD spectra of the WT LHCIIb and the mutants I124L and S123G. The CD spectrum of the WT LHCIIb presents typical finger-print of native LHCIIb, which composed of two negative CD bands (680 nm and 650 nm) in the Qy region and two negative bands (493 nm and 473 nm) in the Soret region (12). I124L showed similar CD spectrum as the WT LHCIIb, both in the position and amplitude of the peaks (Fig 1), while S123G presented a different pattern in the CD spectrum because the relative amplitude of the two negative peaks in the Soret region changed. Calculating the ratio of the amplitude of the CD signals at 473 nm and 493 nm (Neo band: CD_{473nm}/CD_{493nm}) as described in (14), we can see that the Neo band of S123G was almost twice as high (1.23±0.13) as compared to that of the WT LHCIIb (0.66±0.15). It seems that the disturbance of the pigment occupancy resulted from the mutagenesis has changed the conformational arrangement of the complete chromophore of LHCIIb. The Neo band is a useful parameter indicating the binding and the conformation of Neo in LHCIIb (12, 14). Hobe et al (14) has proposed that the Neo band correlated negatively to the amount of Neo bound in the complexes while Liu et al (12) found that the conformation of Neo is also a factor influencing the value of the Neo band. The increased value of the Neo
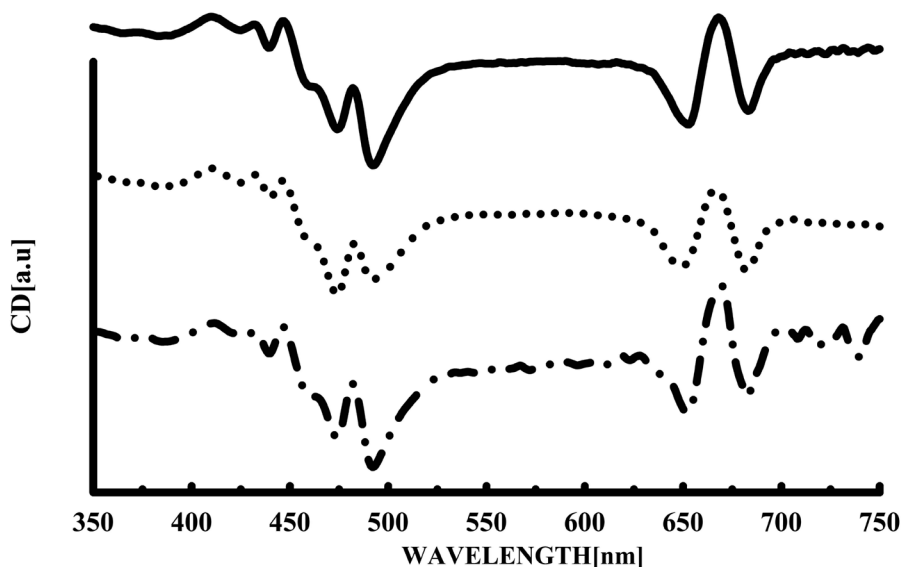
Fig. 1. *Circular dichroism spectra at 10 °C of the different LHCII samples. The spectra are normalized at the same absorption in the Qy Chl a transition.*
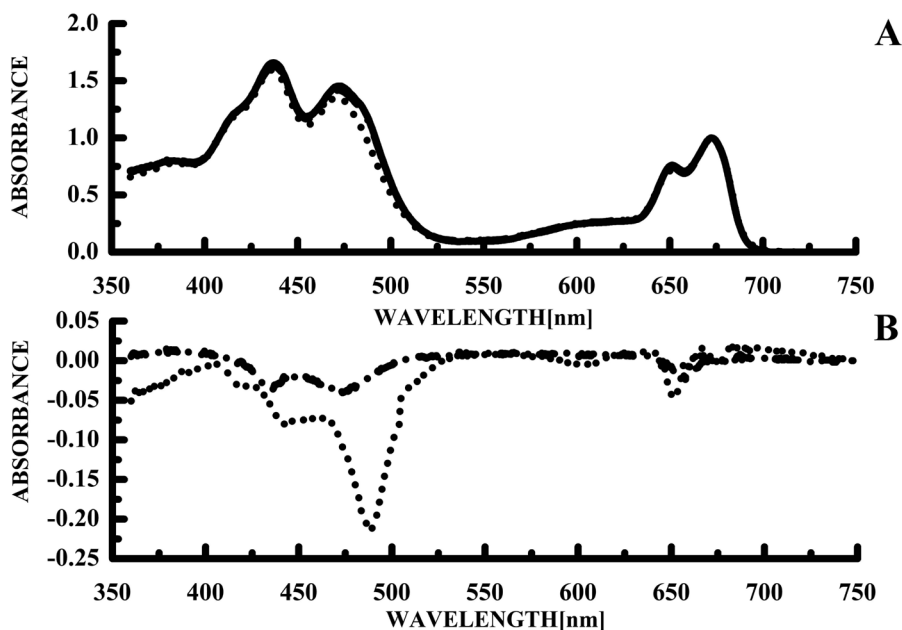

Fig. 2. *Absorption spectra of WT and mutant LHCIIb measured at RT. The spectra were normalized at the Qy Chl a absorption. (A) absorption spectra; (B) difference absorption spectra. Solid line, WT; dot line, S123G; dash line, I124L.*

band of S123G should be a combination effect of low Neo affinity and the changed pigment conformation (Table 1 and Fig. 1). In order to evaluate whether the changes in the turn region influence the functions of LHCIIb, the transition energy and the structural stabilities of the complexes were investigated.

Absorption spectrum provides us with information of the transition energy of chromophores of LHCIIb. **Fig. 2 s**hows the absorption spectra of the WT and the mutant LHCIIbs. It is clearly to see, that the absorption spectrum of I124L did not deviate from that of the WT LHCIIb, while S123G mutagenesis influenced the absorption spectrum strongly, especially in the Soret region. The difference spectrum (Fig 2B) indicates that the S123G showed a pronounced decrease in the absorption at 488 nm, which is coincident both with the pigment stoichiometry (Table 1) and the CD signal measurements (Fig 1). It seems that the decrease in the bound pigment in S123G resulted in changes not only in the pigment conformation, but also in the transition energy of LHCIIb.

The variation in the supermolecular organization of LHCIIb under different external conditions is one of the important mechanisms for photosynthetic apparatus to adapt to the changing external conditions (15,16). Since the turn region is located in the interface between two trimers, the properties of the supermolecular organizations of both mutants have been studied. The aggregation of LHCIIb is accompanied by the appearance of a new fluorescence emission at 700 nm (F_{700}) in addition to the emission of Chl a around 680 nm (F_{680}), which increases along with the increase of the size of the aggregate (3,17). Based on this principle, the degree of the LHCIIb aggregation formed at low detergent concentration (0.049 mM) were analysed with the ratio F_{700}/F_{680}. **Figure 3** shows the 77K fluorescence emission spectra of different LHCIIb species upon excitation at 436 nm. It is interesting to note that the mutagenesis at S123 increased the aggregation degree of the complexes, and in contrast, the mutagenesis at I124 resulted in an opposite effect. It clearly shows that the trimer-trimer interaction of LHCIIb is very sensitive to the properties of the interface between the two molecules. As revealed by the structural resolution (18), the hydroxyl group of S123 forms H-bond with water molecules. Exchanging Ser 123 to G has eliminated the hydrophilic environment (12), which resulted in the susceptibility of S123G to form aggregates. Analysing the structure of I124L, the mutation at the end of the TM helix C, decreased slightly the accessible surface area of the residue, which might change the susceptibility to form aggregates.

To test whether the mutagenesis causes changes in the structural stability of LHCIIb under elevated temperature and strong light intensities, the kinetics of high temperature or strong light induced functional disabilities or photobleaching of different LHCIIb species were measured. Table 2 presents the information of the thermal stabilities and the photobleaching of the different LHCIIb species: 1) The thermal stability was monitored by observing the decay kinetics of Chl b-sensitized Chl a fluorescence emission at 37°C. Tt presented the half-lives of kinetics of LHCIIb. Surprisingly, the thermal stability of S123G did not change, while mutagenesis of I124 to L increased the thermal stability strongly. 2) Under strong light conditions, the overexcited energy in Chls, if it can not be dissipated quickly, may induce photodamage to the Chls. The photostability of different LHCIIbs were monitored by observing the decrease kinetics in the Qy absorption of the bound Chls and the half-lives (Tp) of the decay kinetics were calculated (Table 2). Similar to the thermal stability observation, the
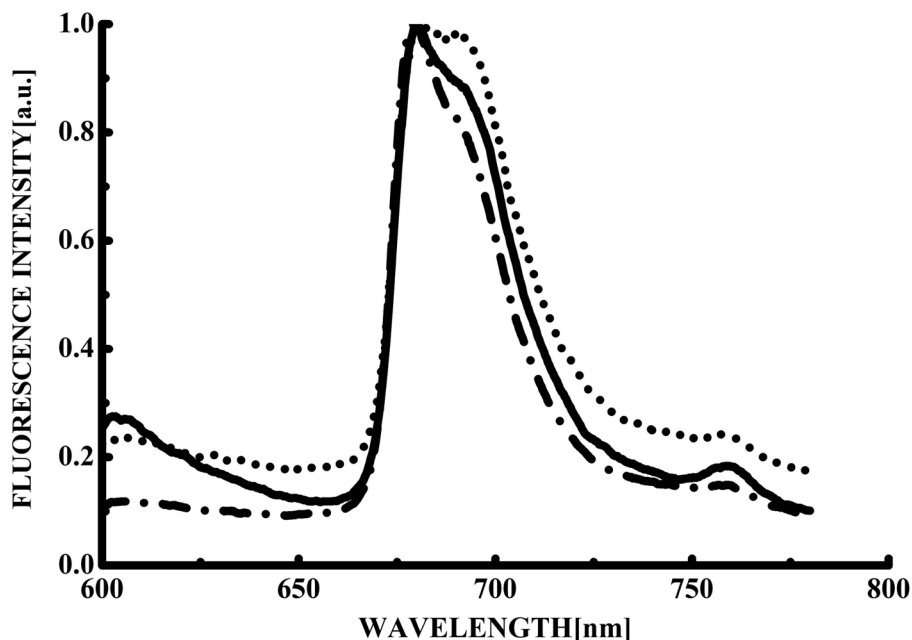
Fig. 3. 77K fluorescence emission spectra of WT and mutant LHCIIb The samples were dissolved in a media containing 0.049 mM DM. Solid line, WT; dot line, S123G; dash line, I124L.

LHCIIb	Thermostability		Photostability	
	T_t(sec)	A_t	T_p (min)	A_p
WT	132.13±5.84	0.67±0.03	15.06±1.8	0.58±0.16
S123G	133.71±10.39	0.78±0.08	14.06±1.7	0.84±0.22
I124L	157.10±6.18	0.49±0.03	12.81±1.6	0.41±0.04

TABLE 2: Structural stability of different recombinant LHCIIb complexes. Parameters of the one-phase exponential decay functions describing the stability of reconstituted complexes toward thermal denaturation (amplitude At, and half-live of the decay Tt) and the decrease in the chlorophyll absorption due to photobleaching (amplitude Ap, and half-live of the decay Tp).

photo-stability of I124L increased significantly. This result provides the first example with pigment-protein complex to support the hypothesis proposed by the previously studies that exchanging one hydrophobic amino acid (Ile124) with similar hydrophobic one (Leu) at the end of a TM helix is an effective measure to stabilize the membrane protein (19,20).

Conclusion: Mutational analysis to the turn between the BC loop and the TM

helix C demonstrated that the motif is very important for the structural stability and supermolecular organization of LHCIIb. S123G increased the susceptibility to form aggregates of LHCIIb. I124L increased the structural stability at both high temperature and strong light intensities.

References:

1. Horton, P., Ruban, A. V., and Walters, R. G. (1996) *Annu.Rev.Plant Physiol Plant Mol. Biol* **47**, 655-684
2. Horton, P., Wentworth, M., and Ruban, A. (2005) *FEBS Lett.* **579**, 4201-4206
3. Kirchhoff, H., Hinz, H. R., and Rosgen, J. (2003) *Biochim. Biophys. Acta* **1606**, 105-116
4. Dreyfuss, B. W., and Thornber, J. P. (1994) *Plant Physiol.* **106**, 829-839
5. Allen, J. F., and Forsberg, J. (2001) *Trends in Plant Sci.* **6**, 317-326
6. Liu, Z. F., Yan, H. C., Wang, K. B., Kuang, T. Y., Zhang, J. P., Gui, L. L., An, X. M., and Chang, W. R. (2004) *Nature* **428**, 287-292
7. Standfuss, R., van Scheltinga, A. C. T., Lamborghini, M., and Kuhlbrandt, W. (2005) *EMBO J.* **24**, 919-928
8. Caffarri, S., Croce, R., Cattivelli, L., and Bassi, R. (2004) *Biochemistry* **43**, 9467-9476
9. Standfuss, J., and Kühlbrandt, W. (2004) *J. Biol. Chem.* **279**, 36884-36891
10. Zhang, Y., Liu, C., Liu, S., Shen, Y., Kuang, T., and Yang, C. (2008) *Biochim. Biophys. Acta* **1777**, 479-487
11. Mick, V., Eggert, K., Heinemann, B., Geister, S., and Paulsen, H. (2004) *Biochemistry* **43**, 5467-5473
12. Liu, C., Zhang, Y., Cao, D., He, Y., Kuang, T., and Yang, C. (2008) *J. Biol. Chem.* **283**, 487-495
13. Yang, C., Lambrev, P., Chen, Z., Jávorfi, T., Kiss, A. Z., Paulsen, H., and Garab, G. (2008) *Biochim. Biophys. Acta* **1777**, 1463-1470
14. Hobe, S., Trostmann, I., Raunser, S., and Paulsen, H. (2006) *J. Biol. Chem.* **281**, 25156-25166
15. Cseh, Z., Vianelli, A., Rajagopal, S., Krumova, S., Kovacs, L., Papp, E., Barzda, V., Jennings, R., and Garab, G. (2005) *Photosynth. Res.* **86**, 263-273
16. Holm, J. K., Varkonyi, Z., Kovacs, L., Posselt, D., and Garab, G. (2005) *Photosynth. Res.* **86**, 275-282
17. Miloslavina, Y., Wehner, A., Lambrev, P. H., Wientjes, E., Reus, M., Garab, G., Croce, R., and Holzwarth, A. R. (2008) *FEBS Lett.* **582**, 3625-3631
18. Li, X. P., Gilmore, A. M., Caffarri, S., Bassi, R., Golan, T., Kramer, D., and Niyogi, K. K. (2004) *J. Biol. Chem.* **279**, 22866-22874
19. Zhou, Y. F., and Bowie, J. U. (2000) *J. Biol. Chem.* **275**, 6975-6979
20. Ambroggio, X. I., and Kuhlman, B. (2006) *J. Am. Chem. Soc.* **128**, 1154-1161

Author Index